TECHNIQUES FOR THE PROCESSING AND ANALYSIS OF MAGNETIC RESONANCE IMAGING PHASE DATA

AMANDA CHING LIH NG

Submitted in total fulfilment of the requirements of the degree of

Doctor of Philosophy

2013

Department of Electrical and Electronic Engineering
Faculty of Engineering
The University of Melbourne

Printed on archival quality paper

ABSTRACT

From its beginnings in the 1970s, the medical imaging field of magnetic resonance (MR) imaging has focussed primarily on the magnitude of the acquired complex data. With ever increasing magnet field strengths, interest in the phase, or argument, of complex T_2^*-weighted gradient echo MR data has grown. Compared to magnitude images, phase images provide novel contrast and increased sensitivity to tissue properties such as magnetic susceptibility.

Several post-acquisition processing methods exploit this sensitivity to susceptibility, notably Susceptibility-Weighted Imaging (SWI) and Quantitative Susceptibility Mapping (QSM). These methods provide greater contrast valuable in the visualisation of biological structures, such as venous vessels, tumours, haemorrhages and subcortical structures. QSM, in particular, may provide the ability to infer changes in chemical composition, such as iron deposition, which is important in the progression of several neurodegenerative disorders such as Parkinson's Disease and Alzheimer's Disease.

Phase imaging-based methods such as SWI and QSM operate on processed phase data. The argument of a complex number is inherently circular, and the MR phase is often affected by spatially slow varying inhomogeneities. In order to extract the localised phase contrast required for SWI and QSM, a combination of phase unwrapping and high pass filtering is necessary. This task is non-trivial, with several methods having been proposed in the literature.

This thesis investigates the processing and analysis of MR phase imaging, proposing four novel techniques that address boundary artefacts introduced by existing phase processing methods, correct for inaccurate structural segmentation in standard SWI at high field strengths, provide optimised contrast images through the combination of magnitude and phase data, and increase accuracy in magnetic susceptibility estimation in QSM.

DECLARATION

This is to certify that

i. the thesis comprises only my original work towards the PhD except where indicated in the Preface,

ii. due acknowledgement has been made in the text to all other material used,

iii. the thesis is fewer than 100 000 words in length, exclusive of tables, maps, bibliographies and appendices.

Melbourne, July 2013

Amanda Ching Lih Ng

PUBLICATIONS

The work presented in this thesis has produced the following journal and conference publications:

[1] A. C. L. Ng, N. Faggian, Z. Chen, J. Zhang, G. F. Egan, and L. A. Johnston, "The Optimised Contrast Image Method for Tissue Contrast Enhancement.," in *Proceedings of the ISMRM 17th Scientific Meeting and Exhibition*, Honolulu, Hawaii, USA, 2009.

[2] A. C. L. Ng, Z. Chen, J. Zhang, G. F. Egan, and L. A. Johnston, "Computationally efficient removal of inhomogeneities at the cortical surface in MR phase images.," in *Proceedings of the ISMRM/ESMRMB Joint Annual Meeting*, Stockholm, Sweden, 2010.

[3] A. C. L. Ng, G. F. Egan, Z.-H. Cho, L. A. Johnston, "Venous vessel boundary delineation at high field using sigmoid-SWI", in *Proceedings of the 33rd Annual International Conference of the IEEE Engineering in Medicine and Biology Society*, Boston MA, USA, 2011.

[4] A. C. L. Ng, L. A. Johnston, Z. Chen, Z.-H. Cho, J. Zhang, and G. F. Egan, "Spatially dependent filtering for removing phase distortions at the cortical surface," *Magnetic Resonance in Medicine*, vol. 66, no. 3, pp. 784–793, 2011.

[5] A. C. L. Ng, S. Moore, L. A. Johnston, "MR Susceptibility Mapping: inversion of large-scale ill-conditioned linear systems," presented at Early Adopters Ph.D. Workshop of the 2011 International Conference for High Performance Computing, Networking, Storage and Analysis, Seattle WA, USA, 2011.

[6] A. C. L. Ng, D. K. Wright, P. Raniga, S. Moore, G. F. Egan, and L. A. Johnston, "Diffusion-guided quantitative susceptibility mapping," in *Proceedings of the ISMRM 21st Scientific Meeting and Exhibition*, Salt Lake City, Utah, USA, 2013.

ACKNOWLEDGMENTS

At the end of this journey, the Acknowledgements is in some ways the easiest and hardest section to write. Easiest, as those that must be acknowledged are always at the fore of your mind during the arduous task that is a PhD, and hardest in that there are so many that helped along the way, too many to list, and listing implies some sort of hierarchy in terms of importance or gratitude. So in no particular order at all ...

A dQSM linear system sized (if you get through Chapter 7, you'll understand) thank you to my colleagues and supervisors, Leigh Johnston, Nathan Faggian, Zhaolin Chen, Parnesh Raniga, Gary Egan, Jingxin Zhang, and others at the Florey Institute of Neuroscience and Mental Health, who provided invaluable advice and direction. It was a steep learning curve and your knowledge and skill at conveying said knowledge was and is greatly appreciated.

A family reunion banquet-sized thank you to all my family for your support, advice and tolerance during this phase of my life. In particular to Mum and Dad, whose advice based on personal PhD journeys and decades of PhD supervisions began with 'are you SURE you want to do a PhD?' and continued with much support and encouragement. A special mention also to my uncle who insisted that completion of my PhD would instill myself as Doctor #10 in the family and contribute towards his goal of collecting a full dozen.

Finally, a friend-related-analogy-sized thank you to all my friends: to those that I've known for many years, who gave me advice from their own PhD endeavours and understood when I retreated into PhD-induced social exile; to those that began and continued their own PhD journeys at the same time as I, providing support and knowing sighs and nods; and to the SCUBA divers and creatures under the sea, without this stress-relieving escape I would surely never have made it to the end.

...

Well, almost no ordering of acknowledgement: at the top of the hierarchy of due gratitude sits my supervisor extraordinaire, Leigh Johnston, who is without doubt the most amazing, knowledgeable, supportive and dedicated supervisor in the history of PhDs. And Mum, whose uncanny ability to not only understand but convey the most complicated mathematical concepts as though they were primary school puzzles transformed mathematical brick walls into small stepping stones during my endeavours to understand that which is magnetic resonance imaging.

CONTENTS

LIST OF FIGURES

LIST OF TABLES

1

INTRODUCTION

Magnetic resonance imaging (MRI) is a medical imaging modality that provides exquisite two-dimensional and three-dimensional images of internal physical structures and chemical composition, such as soft tissues in biological objects. Of particular benefit to the medical field is the ability to distinguish between different tissue types without the use of invasive methods.

Nuclear magnetic resonance (NMR) was discovered in 1946 by Felix Bloch and Edward Purcell, both of whom were awarded the Nobel Prize in 1952. In the 1970s, Raymond Damadian, Richard Ernst, Paul Lauterbur and Peter Mansfield developed NMR as a tool for medical imaging. It has since advanced in great strides, with current technology enabling vast improvements in the contrast and resolution of MR images, as well as the ability to image structural composition, tissue fibre directionality, brain function and chemical composition [1]. These advances are in part due to development in field strength technology with field strengths of 7 Tesla, 9.4 Tesla and 11.7 Tesla being used and developed in human research [2, 3] and modified NMR machines of up to 16.4 Tesla assisting in animal imaging [4].

Among the many benefits of higher field strength is the increased contrast and resolution in MR phase imaging [5]. Raw MR images are complex valued. Most MR imaging methods employ the magnitude of these complex values as the intensity of voxels within the image data. MR phase images utilise the argument, or phase, of the complex values to produce images with contrast and structural information that is complementary to the magnitude images. For gradient echo sequences, the phase data is directly proportional to the gyromagnetic ratio of the excited protons and the magnetic field experienced by the protons, allowing for a relationship to be drawn between phase values and the inhomogeneity of the magnetic field, magnetic susceptibility and the chemical composition of tissues. Several processing methods exploit the relationship between these contributors and phase data, such as Susceptibility Weighted Imaging [6, 7] and Quantitative Susceptibility Mapping [8, 9, 10].

The benefit of these methods is particularly apparent in the study of neurodegenerative disorders, as well as the study of cardiovascular physiology. Susceptibility Weighted Imaging is widely used in the clinical environment as a venography tool[7, 11], as well as a tool for assessing strokes [12], tumours [13] and haemorrhages [14]. The increased resolution and contrast associated with greater field strengths have also lead to interest in imaging smaller structures, such as the

Stria of Gennari [15, 16]. Quantitative Susceptibility Mapping, with its promise of quantitative measures of tissue properties and composition, can provide further insights into changes into physiological change and pathologies associated with neurological disorders, such as microbleeds associated with stroke [17], iron deposition associated with Friedrich's Ataxia and Alzheimer's Disease [18]. In order to explore and advance the contributions of MR phase and susceptibility imaging to biomedicine, the processing and analysis methods need to be developed and enhanced.

The nature of complex values is such that the argument, or raw phase, is restricted to the range $[-\pi, \pi)$. In contrast, the true phase lies in an infinite range such that the raw phase is considered to be the true phase modulo 2π. The process of converting raw phase to true phase is known as phase unwrapping and is a non-trivial task. Furthermore, the true phase is often overwhelmed by large scale field inhomogeneities. For echo planar imaging-based methods, such as diffusion imaging and functional MRI, this is advantageous as it provides a means to estimate field inhomogeneity-induced artefacts in the MR data [19, 20]. However, it obscures visualisation of fine details that provide beneficial information about the composition of local structures. Removal of the large scale inhomogeneities is also non-trivial, where substantial noise in air-filled spaces affects the estimation of the field in nearby structures.

The fine structural details in the phase provide novel contrast compared to the magnitude. While magnitude images feature distinct contrast between different tissue types, phase images provide clear edge contrast at the interface between different tissues. The combination of phase contrast with magnitude contrast can elicit further information and meaningful visualisation of structures. Susceptibility Weighted Imaging (SWI) is perhaps the most well-known of such methods. It is able to exploit slight differences in phase contrast to attenuate magnitude images and reveal structures that are not otherwise visible [6, 7].

Recently, research has focussed on the relationship between magnetic susceptibility and phase. With a theoretical model based in the physics of electromagnetism, methods have been proposed that seek to estimate voxel-wise magnetic susceptibility values from local phase image data, known as Quantitative Susceptibility Mapping (QSM). The model assumes the superposition principle applied to magnetic field perturbation contributions of each voxel, where each voxel is modelled as spherical. The system describing this model is both very large and underdetermined, and thus various methods and approaches have been proposed to overcome these difficulties [8, 9, 10, 21]. However, these methods are also hindered by the fundamental assumption that the voxels conform to a spherical model. In fact, several papers have shown that white matter in the brain is not accurately modelled by spheres, but rather conforms to a cylindrical model of field perturbation.

The background section of this thesis comprises two chapters and presents the fundamental theory of magnetic resonance imaging and phase imaging:

In Chapter 2, a brief description of magnetic resonance imaging provides an understanding of the physics and concepts of this imaging modality. The chapter covers nuclear magnetic resonance, magnetic fields, relaxation, the Bloch equation, image formation and the gradient echo sequence.

Chapter 3 focuses on the emerging use of phase contrast in MRI, including a discussion on the physical mechanisms that produce phase shifts, the biological origins of phase, phase image processing methods and techniques that exploit phase data to optimise the use of available information, such as Susceptibility Weighted Imaging and Quantitative Susceptibility Mapping.

The novel works section of this thesis details four methods that enhance and advance the use of MR phase imaging:

CHAPTER 4 - SPATIALLY DEPENDENT FILTERING Processed phase images are derived from the phase signal by removing the bias field and phase wraps from the initial data. However, the usefulness of this data has been hindered by artefacts at the brain/non-brain surface, particularly in cortical regions. Spatially Dependent Filtering efficiently removes surface artefacts by performing Gaussian filtering with spatially varying parameters of unwrapped or complex filtered phase images. The proposed method is shown to produce improved images, revealing underlying structure and detail that are otherwise obscured by surface artefacts in images produced by traditional phase processing methods.

CHAPTER 5 - SIGMOID-SWI Susceptibility Weighted Imaging employs phase data to attenuate magnitude images, giving rise to novel contrast, particularly in the presence of venous structures. At higher field strengths, the effects of localised magnetic susceptibility differences are amplified, leading to increased phase contrast and larger susceptibility artefacts [11, 22]. In SWI, this can affect the visibility of large vein boundaries, resulting in incorrect vessel segmentation. The Sigmoid-SWI method is an enhanced SWI method that employs known phase characteristics to correct the contrast at venous boundaries. The method is applied to 7T in vivo healthy human data and is shown to improve the delineation of venous vessels.

CHAPTER 6 - OPTIMISED CONTRAST IMAGING This chapter presents a method for combining the contrast information from two related images into a single image. In this case, the two images are the magnitude and phase images derived from a single complex MR image. The Optimised Contrast Imaging (OCI) method adopts a novel approach to the combination of the two images:

it fits a Gaussian mixture model (GMM) to the two-dimensional histogram that represents the distribution of voxels in a magnitude-phase cartesian plane; the GMM is then manipulated to effect changes in image contrast. In contrast to the heuristic nature of SWI, the OCI image formation task is formulated as an optimisation problem in which images with maximal tissue contrast are constructed from the complex-valued data. The method is validated on 3T and 7T in vivo healthy human data and is shown to produce improved contrast over three variants of Susceptibility Weighted Imaging.

CHAPTER 7 - DIFFUSION-GUIDED QUANTITATIVE SUSCEPTIBILITY MAPPING Quantitative Susceptibility Mapping aims to derive reliable estimates of the magnetic susceptibility of voxels from magnetic resonance phase data. Magnetic susceptibility affects the local magnetic flux density which is directly proportional to the phase of complex MR gradient-echo imaging data. Current methods assume that the total change in flux density due to an object of arbitrary shape in a vacuum can be estimated by considering the object to be composed of many very small spheres and summing the change in flux density produced by each sphere. However, research has demonstrated that white matter is more accurately characterised using cylindrical models. Presented here is a diffusion-guided quantitative susceptibility mapping method for deriving susceptibility maps that combines both spherical and cylindrical models. This proof-of-principle method uses diffusion-weighted MRI data to identify voxels best modelled as cylinders and to determine the orientation of those cylinders. The Diffusion-guided Quantitative Susceptibility Mapping (dQSM) results demonstrated better accuracy and robustness compared to methods based solely on a spherical model, establishing that heterogenous modelling of susceptibility effects is both possible and enhances reliability of quantitative susceptibility maps.

BIBLIOGRAPHY

---

[1] E. Mark Haacke, Robert W. Brown, Michael R. Thompson, and Ramesh Venkatesan. *Magnetic Resonance Imaging: Physical Principles and Sequence Design*. John Wiley & Sons, Inc, New York, 1999.

[2] Jeff H. Duyn. The future of ultra-high field MRI and fMRI for study of the human brain. *NeuroImage*, 62(2):1241–1248, August 2012.

[3] Hitoshi Wada, Masaki Sekino, Hiroyuki Ohsaki, Tatsuhiro Hisatsune, Hiroo Ikehira, and Tsukasa Kiyoshi. Prospect of high-field MRI. *IEEE Transactions on Applied Superconductivity*, 20(3):115 –122, June 2010.

[4] Roger M. Bourne, Nyoman Kurniawan, Gary Cowin, Paul Sved, and Geoffrey Watson. Microscopic diffusion anisotropy in formalin fixed prostate tissue: Preliminary findings. *Magnetic Resonance in Medicine*, 68(6):1943–8, December 2012.

[5] Jeff H. Duyn, Peter van Gelderen, Tie-Qiang Li, Jacco A. de Zwart, Alan P. Koretsky, and Masaki Fukunaga. High-field MRI of brain cortical substructure based on signal phase. *Proceedings of the National Academy of Sciences*, 104(28):11796–11801, July 2007.

[6] E. Mark Haacke, Yingbiao Xu, Yu-Chung N. Cheng, and Jürgen R. Reichenbach. Susceptibility weighted imaging (SWI). *Magnetic Resonance in Medicine*, 52(3):612–618, 2004.

[7] Jürgen R. Reichenbach, Ramesh Venkatesan, Douglas J. Schillinger, Daniel K. Kido, and E. Mark Haacke. Small vessels in the human brain: MR venography with deoxyhemoglobin as an intrinsic contrast agent. *Radiology*, 204(1):272–277, July 1997.

[8] Tian Liu, Jing Liu, Ludovic de Rochefort, Pascal Spincemaille, Ildar Khalidov, James Robert Ledoux, and Yi Wang. Morphology enabled dipole inversion (MEDI) from a single-angle acquisition: Comparison with COSMOS in human brain imaging. *Magnetic Resonance in Medicine*, 66(3):777–783, 2011.

[9] Tian Liu, Pascal Spincemaille, Ludovic de Rochefort, Bryan Kressler, and Yi Wang. Calculation of susceptibility through multiple orientation sampling (COSMOS): a method for conditioning the inverse problem from measured magnetic field map to susceptibility source image in MRI. *Magnetic Resonance in Medicine*, 61(1):196–204, January 2009.

[10] Karin Shmueli, Jacco A. de Zwart, Peter van Gelderen, Tie-Qiang Li, Stephen J. Dodd, and Jeff H. Duyn. Magnetic susceptibility mapping of brain tissue in vivo using MRI phase data. *Magnetic Resonance in Medicine*, 62(6):1510–1522, December 2009.

[11] Peter Koopmans, Rashindra Manniesing, Wiro Niessen, Max Viergever, and Markus Barth. MR venography of the human brain using susceptibility weighted imaging at very high field strength. *Magnetic Resonance Materials in Physics, Biology and Medicine*, 21(1):149–158, 2008.

[12] Marc Hermier and Norbert Nighoghossian. Contribution of susceptibility-weighted imaging to acute stroke assessment. *Stroke*, 35(8):1989–1994, 2004.

[13] Vivek Sehgal, Zachary Delproposto, E. Mark Haacke, Karen A. Tong, Nathaniel Wycliffe, Daniel K. Kido, Yingbiao Xu, Jaladhar Neelavalli, Djamel Haddar, and Jürgen R Reichenbach. Clinical applications of neuroimaging with susceptibility-weighted imaging. *Journal of Magnetic Resonance Imaging*, 22(4):439–450, 2005.

[14] Hao-Li Liu, Yau-Yau Wai, Wen-Shiang Chen, Jin-Chung Chen, Po-Hong Hsu, Xin-Yu Wu, Wen-Cheng Huang, Tzu-Chen Yen, and Jiun-Jie Wang. Hemorrhage detection during focused-ultrasound induced blood-brain-barrier opening by using susceptibility-weighted magnetic resonance imaging. *Ultrasound Med Biol*, 34(4):598–606, 2008.

[15] Emmanuel L. Barbier, Sean Marrett, Adrian Danek, Alexander Vortmeyer, Peter van Gelderen, Jeff Duyn, Peter Bandettini, Jordan Grafman, and Alan P. Koretsky. Imaging cortical anatomy by high-resolution MR at 3.0T: detection of the stripe of gennari in visual area 17. *Magnetic Resonance in Medicine*, 48(4):735–738, 2002.

[16] Satoru Ide, Shingo Kakeda, Yukunori Korogi, Tetsuya Yoneda, Johji Nishimura, Toru Sato, Yasuhiro Hiai, Norihiro Ohnari, Masanori Takahashi, Kenji Hachisuka, Hitoshi Fujiwara, and Atsuji Matsuyama. Delineation of optic radiation and stria of gennari on high-resolution phase difference enhanced imaging. *Academic Radiology*, 19(10):1283–1289, October 2012.

[17] Tian Liu, Krishna Surapaneni, Min Lou, Liuquan Cheng, Pascal Spincemaille, and Yi Wang. Cerebral microbleeds: burden assessment by using quantitative susceptibility mapping. *Radiology*, 262(1):269–278, January 2012.

[18] Madhavi Thomas and Joseph Jankovic. Neurodegenerative disease and iron storage in the brain. *Current Opinion in Neurology*, 17(4):437–442, August 2004.

[19] Yung-Chin Hsu, Ching-Han Hsu, and W.-Y.I. Tseng. Correction for susceptibility-induced distortion in echo-planar imaging using field maps

and model-based point spread function. *IEEE Transactions on Medical Imaging*, 28(11):1850 –1857, November 2009.

[20] Paul J. Reber, Eric C. Wong, Richard B. Buxton, and Lawrence R. Frank. Correction of off resonance-related distortion in echo-planar imaging using EPI-based field maps. *Magnetic Resonance in Medicine*, 39(2):328–330, 1998.

[21] Ferdinand Schweser, Andreas Deistung, Karsten Sommer, and Jürgen Rainer Reichenbach. Toward online reconstruction of quantitative susceptibility maps: Superfast dipole inversion. *Magnetic Resonance in Medicine*, 69(6):1582–94, June 2013.

[22] Juliane Budde, G. Shajan, Jens Hoffmann, Kâmil Uğurbil, and Rolf Pohmann. Human imaging at 9.4 t using T2*-, phase-, and susceptibility-weighted contrast. *Magnetic Resonance in Medicine*, pages 544–550, 2010.

Part I

BACKGROUND

2

MAGNETIC RESONANCE IMAGING FUNDAMENTALS

The phase component of the MR signal is the basis of techniques such as Susceptibility Weighted Imaging and Quantitative Susceptibility Mapping which seek to derive important information and provide novel contrast from MR data. These methods are not purely image processing; they are based on the fundamental physical processes that give rise to the MR signal. Discussed in this chapter is the origin of the MR signal and how it is harnessed and processed into MR image data. Also discussed are the processing techniques specific to phase imaging and methods which utilise phase data to provide valuable information for neuroimaging research.

2.1 NUCLEAR MAGNETIC RESONANCE

Magnetic resonance imaging exploits the phenomenon of nuclear magnetic resonance, where the nuclei of specific atoms resonate in response to an external magnetic field. Atomic nuclei are composed of protons (positively charged particles) and neutrons (neutrally charged particles). The atomic number of a nuclei refers to the number of protons, while the atomic mass number refers to the total number of protons and neutrons. NMR arises due to a property of atoms known as spin, an angular momentum, $\boldsymbol{J}$. Its related quantity, the spin quantum number, I, is determined by the atomic number and atomic mass number:

1. when the atomic mass number is even and the atomic number is also even, $I = 0$;
2. when the atomic mass number is even and the atomic number is odd, $I \in \{1, 2, 3, \dots\}$;
3. when the atomic mass number is odd, $I \in \left\{\frac{1}{2}, \frac{3}{2}, \frac{5}{2}, \dots\right\}$.

When the spin quantum number is non-zero, the nucleus is said to be NMR-active.

The most important nucleus in MRI is that of the ^{1}H isotope. It is the most abundant isotope in the human body due to the high water content in soft tissue. The ^{1}H nucleus has a spin quantum number of $1/2$. It has one proton and zero neutrons, and thus MRI terminology often refers to “proton spins” and “proton density”.

The non-zero spin of a nucleus creates a very small magnetic field known as a magnetic dipole moment, $\boldsymbol{\mu}$, where the relationship to the angular momentum is given by

$$\boldsymbol{\mu} = \gamma \boldsymbol{J}. \tag{2.1}$$

γ is the gyromagnetic ratio of the nucleus, a constant whose units are radians per second per tesla (rad.s^{-1}.T^{-1}). It is more commonly quoted in hertz per tesla (Hz.T^{-1}) where the symbol $\bar{\gamma}$ is used and

$$\gamma = 2\pi\bar{\gamma}. \tag{2.2}$$

The magnitude of $\boldsymbol{\mu}$ is given by

$$\mu = \bar{\gamma} h \sqrt{I\left(I+1\right)} \tag{2.3}$$

where h is Planck's constant, 6.6×10^{-34} J $\cdot$ s. In the absence of an external field, the direction of $\boldsymbol{\mu}$ is randomly distributed. When an external magnetic field, $\boldsymbol{B}_0 = B_0\boldsymbol{k}$, is applied, $\boldsymbol{\mu}$ adopts one of $(2I+1)$ angles, θ, with the applied field where the relationship is given by

$$\cos\theta = \frac{m_I}{\sqrt{I\left(I+1\right)}}. \tag{2.4}$$

Here, $m_I \in \{-I, -I+1, \ldots, I-1, I\}$ is called the magnetic quantum number. For $\frac{1}{2}$-spin nuclei such as ^{1}H, $\theta = \pm 54^\circ 44'$. The existence of both parallel (+) and anti-parallel (-) alignment is a quantum model characteristic and is notably different to the behaviour of a small magnetic field in classical physics, where the small field will align parallel with the applied field. $\boldsymbol{\mu}_z$ is the component of $\boldsymbol{\mu}$ in the direction $\boldsymbol{k}$ and is defined as

$$\mu_z = \bar{\gamma} m_I h. \tag{2.5}$$

The transverse component, $\boldsymbol{\mu}_{xy}$, is randomly distributed and therefore does not have a calculable definite value. Furthermore, the external B field induces a torque on $\boldsymbol{\mu}$, resulting in a rotation of $\boldsymbol{\mu}$ about $\boldsymbol{k}$, known as precession. The frequency of precession is known as the Larmor frequency, ω_0, and is given by

$$\omega_0 = \gamma B_0. \tag{2.6}$$

In MRI, we observe a collection of nucleus spins of a particular type of atom (e.g. ^{1}H), rather than focussing on a single atom. The collection is known as a spin system and the sum of the magnetic dipole moments in the spin system gives a net or bulk magnetisation, $\boldsymbol{M}$. The effect on net magnetisation due to the B field, ignoring relaxation effects (to be introduced in Section 2.4), is given by

$$\frac{d\boldsymbol{M}\left(t\right)}{dt} = \gamma \boldsymbol{M}\left(t\right) \times \boldsymbol{B}\left(t\right). \tag{2.7}$$

When $\boldsymbol{B}\left(t\right)$ is static and homogenous, the transverse components $\boldsymbol{\mu}_{xy}$ are randomly distributed such that the net transverse magnetisation is zero. The net magnetisation parallel to the applied field, $\boldsymbol{M}_{0,z}$, is dependent on the ratio of spins in the various orientations relative to the applied field direction. This ratio is known as the Boltzmann distribution. For the $\frac{1}{2}$-spin system, there are two orientations: where $\boldsymbol{\mu}_z$ is parallel to $\boldsymbol{k}$, and where $\boldsymbol{\mu}_z$ is anti-parallel to $\boldsymbol{k}$. The two orientations are associated with different energy states, where the parallel orientation is the lower energy state. The ratio is described by the Boltzmann relationship

$$\frac{N_{\uparrow}}{N_{\downarrow}} = \exp\left(\frac{\Delta E}{KT}\right), \tag{2.8}$$

where $N_{\uparrow}$and $N_{\downarrow}$ are the number of spins oriented parallel and anti-parallel, respectively, $\Delta E = E_{\downarrow} - E_{\uparrow}$ is the difference in energy between the two states, $K = 1.38 \times 10^{-23}\ \mathrm{JK}^{-1}$ is the Boltzmann constant, and T is the temperature of the system. The number of nuclei in the lower energy state is slightly higher than the number in the higher energy state. This results in a very small non-zero net magnetisation $\boldsymbol{M}_0 = M_{0,z}\boldsymbol{k}$. It is this net magnetisation, commonly known as the longitudinal magnetisation, that is manipulated in MRI to give rise to the measured signals.

2.2 THE MAGNETIC FIELDS

In MRI there are several external magnetic fields: the very large static magnetic field, $\boldsymbol{B}_0$, three smaller gradient fields, $\boldsymbol{G}_x$, $\boldsymbol{G}_y$ and $\boldsymbol{G}_z$, and a smaller oscillating field, $\boldsymbol{B}_1$, termed the radio frequency (RF) excitation field.

The $\boldsymbol{B}_0$ field is a very large static homogeneous field, created by either a resistive, permanent or superconducting magnet. At the time of writing, the field strength of human scanners are commonly 1.5T and 3T, with research dedicated scanners of 7T and 9.4T in existence. Due to the high currents required to produce these very large field strengths, the magnets are constructed with superconducting wire.

A coordinate system called the laboratory frame of reference is defined with reference to the MRI scanner or magnet, where the z direction is the direction of the B_0 field. The x and y directions are orthogonal to z. The definition of the x and y directions are arbitrary, but in the case of typical human MRI scanners, where the bore is horizontal and cylindrical, the y axis is aligned floor to ceiling and the x direction is horizontal and perpendicular to the y axis. Facing in the positive z direction, the x axis increases from right to left.

Three sets of gradient coils are used to create linear gradients in the strength of the static magnetic field in each of the x, y and z directions:

$$\boldsymbol{B}(\boldsymbol{r}) = \boldsymbol{B}_0 + \boldsymbol{G} \cdot \boldsymbol{r} \tag{2.9}$$

where $\boldsymbol{G} = \boldsymbol{G}_x + \boldsymbol{G}_y + \boldsymbol{G}_z$. The z-component of $\boldsymbol{G}$ is known as the gradient field, $B_{G,z}$, and

$$\begin{aligned} G_x &= \frac{\partial B_{G,z}}{\partial x}, \\ G_y &= \frac{\partial B_{G,z}}{\partial y}, \\ G_z &= \frac{\partial B_{G,z}}{\partial z} \end{aligned}$$

are known as the x-gradient, y-gradient and z-gradient, respectively. These magnetic fields are time varying and are used to spatially vary the Larmor frequency of spins by altering the strength of the external field at different locations.

The RF field is used to bring the transverse components of the magnetic dipole moments, $\boldsymbol{\mu}_{xy}$, into phase with each other and to manipulate the direction of the net magnetisation. It oscillates in such a way that its direction rotates in the x-y plane:

$$\begin{aligned} \boldsymbol{B}_1(t) &= B_1^e(t)\left[\cos\left(\omega_{\mathrm{rf}} t + \phi\right)\hat{\boldsymbol{x}} - \sin\left(\omega_{\mathrm{rf}} t + \phi\right)\hat{\boldsymbol{y}}\right] && (2.10) \\ &= B_{1,x}(t) + iB_{1,y}(t) && (2.11) \\ &= B_1^e(t)\, e^{-i\left(\omega_{\mathrm{rf}} t + \phi\right)} && (2.12) \end{aligned}$$

where $B_1^e(t)$ is an envelope function, often a rectangular or sinc pulse, ω_{rf} is the frequency at which the RF field oscillates, and ϕ is the phase of B_1 at time $t = 0$. Since the rotation is in the x-y plane and the change in net magnetisation, $\boldsymbol{M}$, given by (2.7), is proportional to the cross product of $\boldsymbol{M}$ and the applied field (including the RF field), the effect of the RF field is to induce $\boldsymbol{M}$ to move, or flip, away from the$z$-axis and rotate about the z-axis as a spiral on the unit sphere.

2.3 THE ROTATING FRAME OF REFERENCE

A rotating frame of reference is introduced to facilitate understanding of the system. It is defined such that it rotates about the z axis in the direction of precession with a frequency ω_{fr}. If $\omega_{fr} = \omega_{rf}$, then the RF field appears stationary. If the net magnetisation is precessing at $\omega_0 = \omega_{rf}$, then it also appears stationary within the rotating frame. However, if inhomogeneities exist in the B field, then the protons will precess at

$$\omega = \gamma\left(B_0 + \Delta B\right) \tag{2.13}$$

where ΔB is the difference between the B_0 field and the field experienced by the protons. The protons will then rotate off-resonance and appear to rotate in the rotating frame of reference at $\omega' = \omega - \omega_{fr}$.

2.4 THE BLOCH EQUATION AND RELAXATION

Once the RF field has induced a non-zero M_{xy}, after it is turned off, the net magnetisation returns to its equilibrium state, $\boldsymbol{M} = M_{z,0}\boldsymbol{k}$, a process known as relaxation. The change in magnetisation, $\boldsymbol{M}$, with respect to time is described by the Bloch equation:

$$\frac{d\boldsymbol{M}}{dt} = \gamma \boldsymbol{M} \times \boldsymbol{B} - \frac{M_x\hat{\boldsymbol{x}} + My\hat{\boldsymbol{y}}}{T_2} - \frac{(M_z - M_{z,0})\,\hat{\boldsymbol{z}}}{T_1}, \tag{2.14}$$

where $\boldsymbol{B}$ is the applied field and T_1 and T_2 are the relaxation parameters that describe the longitudinal and transverse relaxation, respectively. Longitudinal relaxation occurs as the longitudinal magnetisation, M_z, increases in the positive z-direction, such that

$$M_z\,(t) = M_{z,0}\left(1 - \exp\left(\frac{-t}{T_1}\right)\right) + M_z\,(0_+)\exp\left(\frac{-t}{T_1}\right) \tag{2.15}$$

where $M_z\,(0_+)$ is the longitudinal magnetisation immediately following time $t = 0$. Longitudinal relaxation is also known as spin-lattice relaxation, as the excess energy is dissipated into the surroundings (lattice) of the spins. Transverse relaxation occurs as the transverse magnetisation decreases to zero and is a result of dephasing caused by two mechanisms. Initially, transverse magnetisation occurs because spins are rotating in phase about the z-axis, resulting in a non-zero net magnetisation in the x-y plane. During relaxation, precession of spins are affected by the very slight fluctuations of the local magnetic field caused by neighbouring spins. This results in spins precessing faster or slower than their neighbours and thus dephasing occurs. This dephasing mechanism is known as spin-spin relaxation, and is defined by the time constant T_2. The governing equation is

$$M_{xy}\,(t) = M_{xy}\,(0_+)\,e^{-t/T_2} \tag{2.16}$$

where $M_{xy}\,(0_+)$ is the transverse relaxation immediately following time $t = 0$. The second dephasing mechanism is defined by the time constant T_2' and is a result of larger local magnetic field inhomogeneities caused by environmental factors such as tissue susceptibility. It is often combined with T_2 as

$$\frac{1}{T_2^*} = \frac{1}{T_2} + \frac{1}{T_2'} \tag{2.17}$$

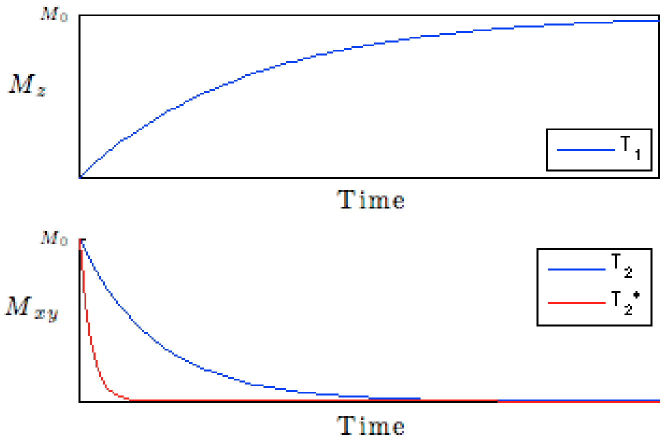

Figure 1: Timing profiles for relaxation parameters T_1, T_2 and T_2^*, given by (2.15) and (2.16).

where the T_2^* is the time constant describing a much faster dephasing mechanism than T_2. In general, T_1 is much longer than T_2, which itself is usually much longer than T_2^* (Fig. 1).

Different tissues have different T_1, T_2 and T_2^* time constants. Magnetic resonance imaging is carefully synchronised to optimise the difference in signal strength (and thus image contrast) between tissues based on these time constants, thus leading to what is termed T_1-weighted, T_2-weighted and T_2^*-weighted imaging. Proton density imaging is yet another contrast method where the image intensities represent differences in $M_z(0)$, and thus is an indication of the density of ^{1}H isotopes.

2.5 SPIN ECHO SEQUENCE

The sequence and timing of the gradient fields and RF pulses determine which part of the subject is imaged, and what contrast is obtained. Slice select, phase encoding and frequency encoding steps form the basis of MRI sequences. They involve the super-position of linear gradient fields to $\boldsymbol{B}_0$. Whilst a gradient is applied, protons precess at different frequencies proportional to the distance along the gradient direction. This results in dephasing of the proton spins, where the accumulation of phase at distance, l, is given by

$$\phi(l,t) = \gamma G l t \tag{2.18}$$

where G is the gradient and t is the time.

During the slice select step, a linear gradient is applied to the B_0 field along one direction, $\boldsymbol{G}_{SS}$, for a time period of τ_{SS}. To simplify explanation, we will assume the gradient is along the z-direction. Since the Larmor frequency, ω, of the protons

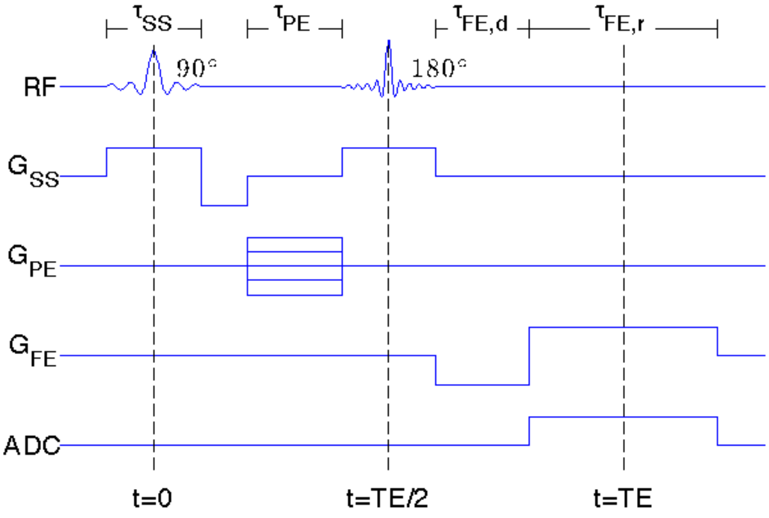

Figure 2: Spin echo sequence. A sinc excitation pulse (RF) is applied in conjunction with a slice select gradient ($\mathrm{G_{SS}}$) for τ_{SS} seconds. This is followed by a negative $\mathrm{G_{SS}}$ to rephase the excited protons. A phase encoding gradient ($\mathrm{G_{PE}}$) is applied for τ_{PE} seconds. A second sinc pulse and slice select gradient is applied at TE/2 seconds to induce a 180° flip. Subsequent to the 180° pulse, the protons rephase, inducing the signal echo which is recorded by the analog-digital converter (ADC). Note that the gradients illustrated display an idealised zero ramp time.

is proportional to the strength of the applied field, the precessional frequency of protons will increase along the z-axis as the applied field strength increases.

$$\omega\left(z\right)=\gamma\left(\boldsymbol{B}_0+\boldsymbol{G}_{SS}z\right). \tag{2.19}$$

An RF pulse can then be tailored to excite protons at a particular z-position, thus selecting a slab, or "slice", perpendicular to the z-axis. The central frequency of the RF pulse, ω, determines the centre of the slice. Increasing the gradient strength, or decreasing the RF pulse bandwidth reduces the thickness of the slice. The excitations are assumed to occur instantaneously at $t=0$. For $\tau_{SS}/2$ seconds following excitation, the slice select gradient, $\boldsymbol{G}_{SS}$ remains on and the excited protons dephase. The time that the RF pulse is applied, τ_p, and the RF pulse power determine the flip angle, α, induced in the net magnetisation,

$$\alpha=\int_0^{\tau_p}\gamma B_1^e\left(t\right)dt. \tag{2.20}$$

For spin echo sequences, the RF pulse is tailored such that a 90° flip angle is induced. Immediately following the positive slice select gradient and RF pulse, a negative slice select gradient is imposed in order to rephase the dipole moments.

The phase encoding step involves the addition of either the x or y gradient, G_{PE} on the B_0 field over a short time period. During this time, the Larmor frequency of protons will differ along the gradient direction. When the gradient is turned off, the protons resume precessing at equal Larmor frequencies to each other, however they will now have a phase shift that is dependent on their position along the phase encoding gradient direction. Protons that were precessing faster will lead those that precessed slower. Thus the position of the proton along the phase encoding axis is encoded as the phase of its precession.

As time progresses, dephasing occurs in the x-y plane due to T_2 and $T_2^{'}$ mechanisms. This leads to a loss of transverse magnetisation. While it is not possible to counteract the dephasing due to the random nature of T_2, it is possible to counteract the $T_2^{'}$ dephasing by applying a 180° RF pulse in conjunction with a repeat of the slice select gradient. Assuming the net magnetisation immediately following the 90° pulse is parallel to the rotating frame of reference axis y', then the excited protons will have accumulated a phase angle of ωt relative to y' at time t. Applying the 180° RF pulse along y' will flip the transverse magnetisation such that the phase angle will be $-\omega t$. Following the 180° RF pulse, rephasing occurs, that is, the phase angle decreases towards zero, and transverse magnetisation accumulates. When coherence is achieved, a signal echo occurs, called the spin echo. The time between the excitation and the echo is the echo time, TE. Since the echo is induced by the 180° pulse, the time to rephase is equal to the time allowed for dephasing. That is, the 180° pulse is applied at TE/2 seconds after the excitation pulse. During the time between the excitation and the echo, relaxation occurs and the echo time can be tailored to weight the contrast in the image according to the T_1 or T_2 relaxation parameters. For multiple excitations, T_1 relaxation occurs during the time between successive excitations, called the repetition time (TR). Thus, the TR affects the magnitude of the longitudinal magnetisation that is excited in the subsequent excitation. The TR can therefore also be tailored to weight the contrast according to T_1.

The frequency encoding step involves the addition of the third B_0 gradient. If the phase encoding step utilises the y gradient, the frequency encoding step will employ the x gradient. Again, the Larmor frequency is altered by the gradient. In this step, the position of the proton along the frequency encoding axis is encoded as the frequency of its precession. To prepare for the echo, a negative gradient, $G_{FE,d}$, is applied for $\tau_{FE,d}$ seconds to dephase the protons. It is then followed by a positive gradient, $G_{FE,r}$, applied for $\tau_{FE,r}$ seconds, such that

$$G_{FE,d}\tau_{FE,d} = \frac{G_{FE,r}\tau_{FE,r}}{2}, \tag{2.21}$$

causing the protons to rephase, giving rise to the recordable signal, a time-varying electromagnetic wave. This signal induces a current in a receiver coil which is recorded with an analog-to-digital converter (ADC) that is switched on for the duration of the rephasing frequency encoding gradient, $\tau_{FE,r}$.

2.6 GRADIENT ECHO SEQUENCE

The spin echo sequence eliminates the effects of $T_2^{'}$ dephasing and therefore it is not suitable for producing T_2^*-weighted images. In this instance, gradient echo sequences are employed, where the primary mechanism by which the echo occurs is the inversion of the gradients. Prior to the echo, a negative gradient is applied along the frequency encoding direction, inducing a dephasing of the spins (Fig.3). The gradient is then reversed in polarity, inducing not only a spatial dependence in the Larmor frequencies of the spins, but also a rephasing and subsequent signal echo. In comparison to the 90° flip angle of the spin echo sequence, the flip angles in gradient echo sequences can be much smaller. The low flip angle allows a reduced relaxation delay and shorter TR, therefore reducing the acquisition time.

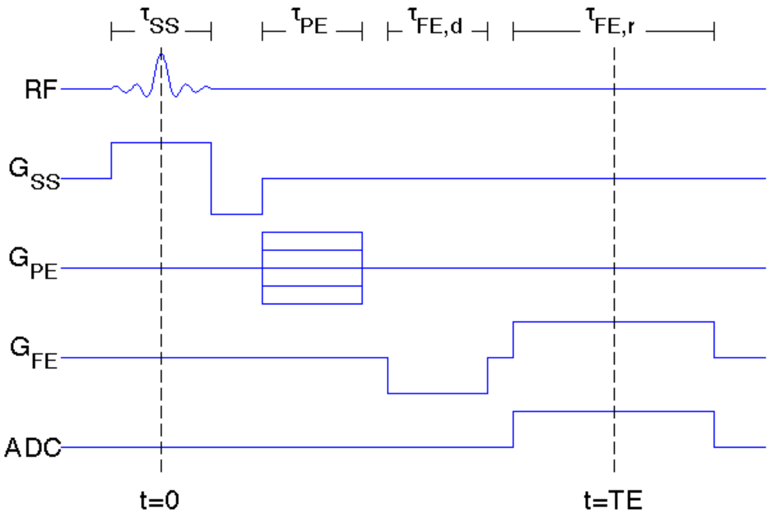

Figure 3: 2D gradient echo sequence diagram. A sinc excitation pulse (RF) is applied in conjunction with a slice select gradient (G_{SS}) for τ_{SS} seconds. This is followed by a negative G_{SS} to rephase the excited protons. A phase encoding gradient (G_{PE}) is applied for τ_{PE} seconds. The signal echo is primed by applying a negative frequency encoding gradient (G_{FE}) for $\tau_{FE,d}$ seconds in order to dephase the protons. During the positive G_{FE}, protons rephase, inducing the signal echo which is recorded by the analog-digital converter (ADC). Note that the gradients illustrated display an idealised zero ramp time.

2.7 K-SPACE AND IMAGE FORMATION

The recorded signal is an integration of the signal from all the excited spatial locations

$$S(t) \propto \int_V \boldsymbol{M}(\boldsymbol{r}, t) \exp\left[i\Delta\phi(\boldsymbol{r}, t)\right] d^3\boldsymbol{r} \tag{2.22}$$

where

$$\Delta\phi\left(\boldsymbol{r},t\right)=-\gamma\int_{0}^{t}\Delta B\left(\boldsymbol{r},\tau\right)d\tau \tag{2.23}$$

is the accumulated phase shift at spatial location $\boldsymbol{r}$ and time t. The change in magnetic field, $\Delta B\left(\boldsymbol{r},t\right)$, is determined by the applied gradient, spatial location and field inhomogeneities such as T_2' effects. Assuming that the field inhomogeneities are much smaller than changes induced by the applied gradient, we have

$$\Delta B\left(\boldsymbol{r},t\right)=\boldsymbol{G}\left(t\right)\cdot\boldsymbol{r}.$$

In T_2^*-weighted gradient echo imaging, the position $\boldsymbol{r}$ is independent of time, assuming negligible flow or diffusion of water molecules, or other protons. It can therefore be taken outside the integral in (2.23) and simplified, giving

$$\Delta\phi\left(\boldsymbol{r},t\right)=\boldsymbol{k}\left(t\right)\cdot\boldsymbol{r} \tag{2.24}$$

where

$$\boldsymbol{k}\left(t\right)=-\gamma\int_{0}^{t}\boldsymbol{G}\left(\tau\right)d\tau.$$

Substituting (2.24) into (2.22), we have

$$S\left(t\right)\propto\int_{V}\boldsymbol{M}\left(\boldsymbol{r},t\right)\exp\left[i\boldsymbol{k}\left(t\right)\boldsymbol{r}\right]d^{3}\boldsymbol{r}$$

which resembles the Fourier transform

$$F\left(\boldsymbol{k}\left(t\right)\right)\propto\int_{V}f\left(\boldsymbol{r}\right)\exp\left[i\boldsymbol{k}\left(t\right)\boldsymbol{r}\right]d^{3}\boldsymbol{r}.$$

Therefore, at time t, the signal $S\left(t\right)$ is the intensity of the Fourier transform of the magnetisation $\boldsymbol{M}\left(\boldsymbol{r},t\right)$ at the point $\boldsymbol{k}\left(t\right)$ in Fourier space, or "k-space". Manipulating the gradients $\boldsymbol{G}$ and the time t allows for signals at different points within k-space to be acquired. This is known as traversing k-space, where the phase encoding step is used to select the position along the k_y axis by applying the gradient G_y for a period of time, and the frequency encoding step is used to traverse a line along the k_x direction. The phase encoding and frequency encoding steps are repeated in order to fill k-space. Performing a 2D inverse Fourier transform on the acquired k-space data produces the complex-valued MR image.

The described technique for 2D slice acquisition can be extended to 3D volume acquisition. Increasing the bandwidth of the RF pulse during the slice select step allows for a wider slab, or volume, to be excited. Phase encoding is performed in both the y and z directions, producing a 3D k-space traversal. The complex-valued 3D image is then computed by performing a 3D inverse Fourier transform on the k-space data. One advantage of 3D acquisitions is the increased resolution in the 3rd, or slicing, dimension.

Traditionally, the magnitude of the complex values in the MR image have been utilised as the intensity of MR images. These are called magnitude images where the voxel intensities are proportional to the net magnetisation, $\boldsymbol{M}(\boldsymbol{r}, t)$ in Eq (2.22), where t is the echo time, TE. In T_2^*-weighted gradient echo images, the phase of the complex numbers can be used to derive phase images, where the phase is proportional to the precessional frequency of protons. In Chapter 3, we explore phase images in more detail: in particular, the origins of phase, processing methods and techniques that utilise phase data to enhance the information content of images.

3

MR PHASE IMAGING

Much attention has been given in recent years to MR phase images, particularly because of an increased contrast-to-noise ratio (CNR) at higher field strengths. While the true nature and source of the phase and related artefacts are not fully understood, it is generally accepted that the greater sensitivity to magnetic susceptibility is a significant contributor to the increased CNR [1, 2]. It is also this sensitivity that has sparked interest in using phase imaging to study neurodegenerative diseases such as Alzheimer's, Parkinson's, Huntington's and multiple sclerosis [3, 4, 5, 6, 7]. Even though the contrast between grey matter (GM) and white matter (WM) is variable across the brain, even disappearing in some instances [8, 9], studies have demonstrated that the contrast is seven to nine fold greater than in magnitude images for T2*-weighted gradient echo (GRE) sequences [3, 8]. Other studies have shown little difference in contrast compared to that of the magnitude image for the same sequence [10]. The heterogeneity of WM and GM in phase images is also striking and has been attributed to microvasculature, myelin, iron content [8] and microstructural orientation [11, 12]. Appearance of veins is particularly well enhanced, although Hammond et al reported a narrower appearance of the veins in phase images compared to magnitude images [3], a phenomenon also mentioned in a study of multiple sclerosis patients [4]. Neither study offered an explanation for these observations. Nevertheless, phase imaging has shown great potential for structural imaging in its enhanced contrast and structural delineation.

In this chapter we present the basic electromagnetism theory that describes the phase of the complex MR signal and explore the biological origins of the phase. We also detail processing steps required to extract structural detail from the phase data and established post-processing techniques that employ phase to modify contrast and information in MR images.

3.1 ELECTROMAGNETISM

The phase angle of T_2^*-weighted GRE data is understood to be a combination of the effects of chemical exchange processes between water and macromolecules and the effects of magnetic susceptibility on the magnetic B field experienced by the H^1 nuclei [1, 2, 13]. In order to comprehend the mechanisms behind the susceptibility of tissues and their effect on the phase angle, some understanding of the physics of electromagnetics is required.

Newcomers to the field of magnetism are often confounded by the concepts of magnetic field intensity (or strength), H, and magnetic flux density, B, most notably because the term “magnetic field” is regularly used interchangeably for both. Magnetic field intensity, H, can be considered to be the “magnetic field” produced by an external source regardless of the material (or lack thereof) within that field, such as the field created by the superconducting magnet of an MRI machine without consideration for the presence of a subject within the machine. The SI unit of H is ampere per metre (A/m). Magnetic flux density, B, is measured in the SI unit Tesla (T) and refers to the induced “magnetic field” that is proportional to the summation of the H field and the magnetisation, M, of the material (or lack thereof) within the H field. In the presence of an H field, material can respond by creating its own additional magnetic field intensity, a concept known as magnetisation. The relationship between the H field and the magnetisation, M, for linear materials is given by

$$M = \chi H \tag{3.1}$$

where the susceptibility, χ, is a unitless property of the material and denotes the degree to which a material is magnetised in the presence of an external magnetic field intensity, H. In the context of MRI, “magnetic field” almost always refers to the magnetic flux density, B, as is indicated by the use of B_0 and B_1 to refer to the static magnetic field and the smaller oscillating magnetic, or RF, field. In human imaging, susceptibility values are very small, of the order of -10^{-5} [14].

The relationship between magnetic flux density, B, magnetic field intensity, H, and magnetisation, M, is given by

$$B = \mu (H + M) \tag{3.2}$$

where the permeability (H/m), μ, is also a property of the material and refers to the resistance (or assistance) of material (or free space) to the flow of a magnetic field through it.

An important permeability constant is the permeability of free space, μ_0, which denotes the relationship between B and H in a vacuum:

$$B = \mu_0 H. \tag{3.3}$$

The permeability of free space is the constant $4\pi \times 10^{-7}$ H/m (henrys per metre).

Relative permeability, μ_r, is the unitless ratio between the permeability of a material, μ, and the permeability of free space, μ_0:

$$\mu_r = \frac{\mu}{\mu_0}. \tag{3.4}$$

Magnetic susceptibility, χ, is related to relative permeability, μ_r, as follows:

$$\chi = \mu_r - 1. \tag{3.5}$$

Materials are often classified in terms of their relative permeability, of which the following terms apply: paramagnetic, diamagnetic and ferromagnetic.

Paramagnetic materials contain atoms with unpaired electrons. These atoms have a permanent magnetic moment. In the absence of an external magnetic field these atoms will be randomly distributed and will therefore tend to cancel each other out to produce a negligible bulk magnetisation. In the presence of an external magnetic field, the magnetic moments will align with the applied field producing a bulk magnetisation in the direction of the applied field. This has the effect of strengthening the magnetic field both within and outside of the material, compared to the field in the absence of the material. The relative permeability, μ_r, of paramagnetic materials is therefore larger than 1.

All atoms, regardless of the number of electrons, have an induced diamagnetic effect in the presence of a time-varying external magnetic field. The motion of the electrons is affected by the field in the same way that a current is produced in a wire by a time-varying magnetic field (Faraday's Law). In contrast to paramagnetism, diamagnetism induces a bulk magnetisation in an anti-parallel direction to the applied magnetic field. The strength of diamagnetism is weak compared to paramagnetism. However when atoms have paired electrons, paramagnetism is negligible and diamagnetism is dominant. Diamagnetic materials have a relative permeability, μ_r, smaller than 1.

Ferromagnetic materials, such as iron, nickel, cobalt, gadolinium and dysprosium, comprise of domains within which the atoms are aligned with each other and produce a strong magnetic field regardless of the presence of an external field. In the presence of an external field, these domains align with the field to produce a very strong magnetic field. The alignment is known as 'magnetic saturation'. Provided the temperature is below a critical point, the Curie temperature, the magnetisation is permanent and remains after removal of the external field. Ferromagnetic materials thus have a relative permeability, μ_r, much greater than 1.

3.2 THE ORIGINS OF MR PHASE

An MR image of the brain (for example) created purely by using the phase angle of the measured complex signal without post-processing has very little resemblance to the structure of the brain. In fact it is primarily representative of B_0 field inhomogeneities, often with lines of sharp intensity changes due to phase values wrapping about the $-\pi/\pi$ border (Fig. 4a). Once phase is unwrapped (Fig. 4b) and the background inhomogeneities (low frequency changes) are removed (Fig. 4c), the detailed phase image (Fig. 4d), or high frequency variations, are evident. These are the localised phase variations, the source of which is still in contention, as previously mentioned.

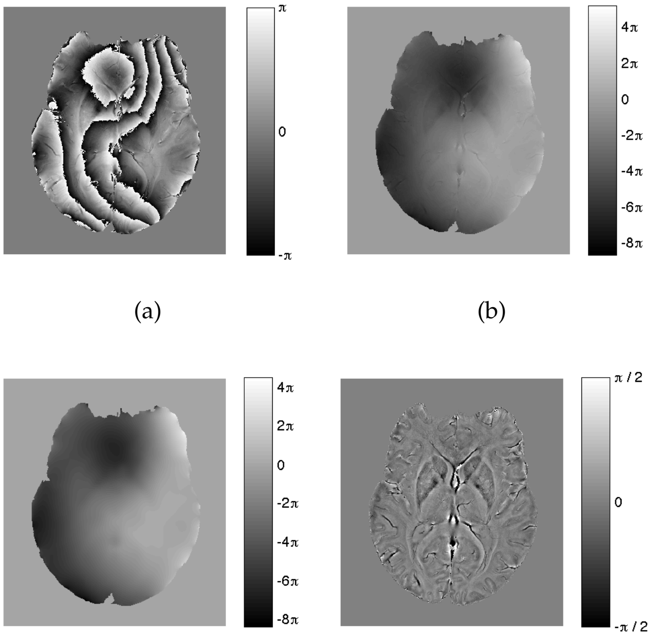

(a) (b)

(c) (d)

Figure 4: Phase processing: the (a) raw phase image, demonstrating $-\pi/\pi$ phase wraps, is (b) unwrapped, then (c) spatially high-pass filtered. The filtered image is subtracted from the unwrapped image to produce the (d) final phase image

The phase angle in MRI complex data arises because protons do not precess at the exact same frequency. In phase sensitive MRI acquisitions, the contribution of the absolute B_0 and gradient field strength to the frequency is implicitly removed during the signal detection and image reconstruction steps. The frequencies of proton precession are affected by microscopic differences in B_0, such as those produced by tissue susceptibility and frequency shifts caused by microscopic chemical exchange processes between free water and macromolecules [13]. Tissue susceptibility alters the B_0 field by inducing magnetisation in the tissue at the microscopic, or sub-voxel, level. Such differences give rise to the observed difference in intensity value in MRI phase images [8].

Human brain tissue, such as grey matter and white matter, is largely composed of water. Water is diamagnetic and has a susceptibility value of -9.05×10^{-6} at body temperature (37°C) [15]. While human tissue is also diamagnetic, with susceptibility values within ±20% of that of water, that is, between -11.0×10^{-6} and -7.0×10^{-6}, it is incorrect to assume that the high water percentage is solely responsible for its diamagnetic value. Paramagnetic molecules or ions, such as oxygen or ferritin, can theoretically cancel the diamagnetic effect of hundreds or thousands of water molecules [15]. However, paramagnetic materials are very rarely present in concentrations large enough to significantly alter the magnetism of tissue, and when so, are usually a sign or symptom of a pathology. Measurement of the susceptibility of biological tissues is considerably challenging, due to their relatively small values and the heterogeneous nature of tissues. In MRI, brain tissue is often assumed to be similar to water [16] and therefore the value -9.05×10^{-6} is used in calculations. This assumption was supported by susceptibility measurements of ex vivo rat cortex [17], and a very recent study by Peprah et al. [18], who measured ex-vivo fixed rat brain tissue susceptibility in the range -9.51×10^{-6} to -8.99×10^{-6}, although changes in tissues following death, the effects of fixation, and other possible differences between live and dead tissues on susceptibility have not been explored.

The relatively large contrast between brain tissue and venous vessels in phase images can be attributed to the susceptibility effects of the deoxygenated blood, or more precisely, the presence of deoxyhaemoglobin. Deoxyhaemoglobin molecules are slightly paramagnetic, with a susceptibility of approximately 0.15×10^{-6} [15]. They reside within red blood cells which, given the concentration of water compared to deoxyhaemoglobin molecules, have a susceptibility of -6.52×10^{-6}. The susceptibility of deoxygenated whole blood with a hematocrit of 0.45 varies due to varying levels of red blood cells in the volume, but nevertheless has a susceptibility of approximately -7.9×10^{-6} for a normal adult human. Since this value is less diamagnetic than brain tissue, the B_0 field will be stronger in the location of veins, thus leading to a more negative phase value compared to that of brain tissue [19]. While the susceptibility of venous vessels has only a small difference from the assumed susceptibility of brain tissue, it is enough to form distinct contrast in phase images.

Despite the common assumption that the intensities in phase images are a result of the tissue's susceptibility, it is apparent from several studies that the magnetic susceptibility of biological material on its own cannot account for the measured phase contrast [8, 13, 20, 21]. Not only does the shape of the biological object affect the magnetisation, but so does its orientation [15, 22]. It is well known that for long cylindrical objects, such as veins, a magic angle with respects to the B_0 field's direction exists at which the susceptibility has no effect on the intensity in the phase image, and the object ceases to have enhanced phase contrast [23]. Studies support the theory that a correlation exists between iron content in grey matter and phase shift, yet the hypothesised relationship does not accurately predict phase contrast where iron is not present, such as in white matter [20, 21]. It has been suggested that these discrepancies arise as a result of the lower water content and high lipid content in white matter [20]; however Duyn et al [8] have also demonstrated that these alone cannot account for the phase shifts measured in white matter. Grey matter is known to have higher vasculature density than white matter, yet an examination of the effects of deoxyhaemoglobin in grey matter reveals that deoxyhaemoglobin content alone cannot be responsible for the observed phase shifts [8]. Furthermore, in the literature encountered that seeks to study the relationship between tissue susceptibility and phase, the possible spatial shift of signal in the image domain due to susceptibility differences has not been explored. The change in frequency, Δf, associated with a change in susceptibility, $\Delta\chi$, is given by $\Delta f = \frac{1}{3}.f_0.\Delta\chi$ [20, 24], where f_0 is the operating frequency. At 7T, $f_0 = 298$ MHz and the typical bandwidth is approximately 30 Hz [8]. For an equivalent change in frequency, $\Delta f = 30$ Hz, due to susceptibility, the expected $\Delta\chi$ is 3×10^{-7}, which is approximately the susceptibility range of brain tissues [18]. It is therefore possible that spatial shifts in the image may occur in some tissues, accounting for the noticeable heterogeneity at boundaries between grey matter, white matter and blood vessels. Without more extensive ground-truth knowledge of the susceptibility and chemical composition of tissues being imaged, we may not be able to conclusively state the extent of the role tissue susceptibility has in defining phase contrast.

An alternative source of phase contrast was suggested by Zhong et al [13], who proposed that phase contrast is a result, in part, of microscopic chemical exchange processes between free water and macromolecules. Macromolecule concentration has a close relationship with T_1 and T_2 spin relaxation times via exchange between bulk tissue water and hydrophilic groups on the surface of macromolecules. Despite these exchange processes being fast, of the order of 10^{-10} seconds, they can still result in small phase shifts in the water resonance. The amount of shift is dependent on the concentration and type of macromolecules, therefore it is logical to conclude that the differing macromolecule environments of grey matter (GM) versus white matter (WM) would have an effect on the intensity in MRI phase images. Zhong et al demonstrated that not only is there a linear relationship between macromolecule concentration and phase shift, but that it is sufficient to explain the observed GM/WM phase contrast in some regions of the brain [13].

Both theories of the origin of phase contrast fail to provide an explanation for phase shifts in all areas of the brain, particularly in the cerebrospinal fluid (CSF) and the Stria of Gennari. CSF contains very little deoxyhaemoglobin, iron or myelin, and in comparison to GM and WM, it has very low concentrations of macromolecules [13]. Its susceptibility is assumed to be very close to that of water, yet phase images show that its phase shift is far closer to that of WM. The Stria of Gennari, known through histology studies to be high in myelin content in comparison to surrounding GM, has a phase-derived frequency much higher than GM which, itself, is higher than the adjacent WM [8]. The basic notion that magnetic susceptibility and macromolecule presence affects phase shifts in MRI is sound; however, the complexity of the brain, from the chemical composition in not only different tissues, but different locations, to the intricate structural shapes, hampers efforts to fully understand the source of phase contrast.

3.3 PHASE UNWRAPPING AND FILTERING

The creation of phase images from complex MRI data that clearly depict the structural details of the brain necessitates the removal of background field inhomogeneities. While these inhomogeneities are low in spatial frequency they are much larger in amplitude relative to that of the structural details. The range of these phase values often extend beyond 2π, creating distinct contrast lines in the image where the phase values wrap about the $-\pi/\pi$ threshold. Thus, creation of phase images requires not only the removal of the low frequency fluctuations, but also correction of the phase wrapping. The most common methods of phase wrap elimination are homodyne filtering [23, 25] and phase unwrapping algorithms in image space [26].

Homodyne filtering involves the division of the original complex image by a low pass filtered version of the same complex image, resulting in a high-pass filtered image. The drawback to this method is the trade-off between high-pass filtering and removal of phase wraps. If the filtering is too aggressive, low frequency details specific to anatomical structure and not inhomogeneities may be removed. Conversely, if the filtering is too conservative, removal of phase wraps may remain incomplete.

Phase unwrapping algorithms [27, 28, 29] tackle the phase wrap problem in image space and, unlike homodyne filtering, have the advantage of preserving all spatial frequencies. The algorithms are based on the interpretation of the phase unwrapping challenge as the search for the value n for every voxel, where the true phase, ϕ_T, is equal to the wrapped phase, ϕ_W, plus n multiples of 2π:

$$\phi_T = \phi_W + 2\pi n. \tag{3.6}$$

If the true phase of all voxels is within 2π of the true phase of all its neighbours, then the phase unwrapping problem is trivial. However this is not always the case. Algorithms have to identify when phase unwrapping is required and when the true change in phase is greater than 2π. Incorrect decisions will result in obvious artefacts, such as streaking in the image. Laplacian-based phase unwrapping algorithms, in particular, are increasing in popularity [29]. These algorithms demonstrate robustness to noise and compute faster than most methods. However, the reliability is reduced in the presence of noise and large gradients, such as at the border of the brain. The drawback to phase unwrapping algorithms arises as a result of the steep transition between a region of no signal (i.e. background or air-filled cavities) and a region with signal. At these interfaces, the change in

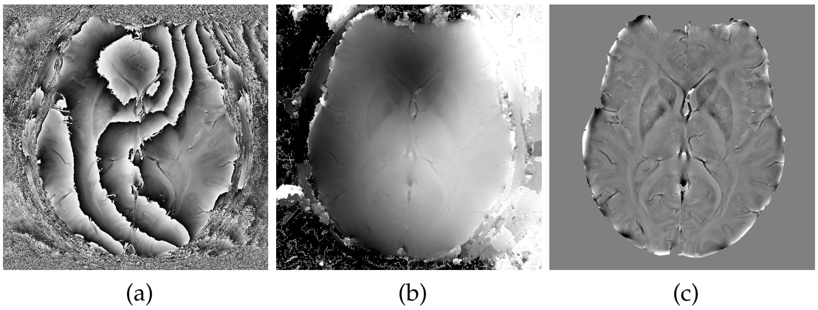
(a) (b) (c)

Figure 5: The (a) wrapped, (b) unwrapped and (c) filtered phase image demonstrating artefacts at the edge of the brain.

phase can be several multiples of π. The subsequent low pass filtering (to remove the slow fluctuating background field inhomogeneities) results in poor quality at these borders (Fig. 5c). Thus while algorithm-based unwrapping of phase images is able to more effectively maintain spatial frequencies than homodyne filtering in the centre of the brain, the loss of quality at the border restricts the usability of these images for study of the cortical layers.

Rauscher et al [26] addressed the disadvantages of homodyne filtering and phase unwrapping algorithms by developing an algorithm which is a hybrid of both methods. The algorithm seeks to circumvent the trade-off in homodyne filtering by applying a phase unwrapping algorithm to the low-pass filtered version of the complex image. This eliminates the need in the homodyne filtering method to increase the threshold in the low pass filter to a level where all phase wraps are removed. The phase images processed by Rauscher et al's method show significant improvement in the quality of the image near the brain-background border. Nevertheless, this method is limited to situations where the high frequency fluctuations do not, themselves, result in phase wraps. Although these situations are quite rare in MRI phase imaging, they could, theoretically, be resolved by performing an additional phase unwrapping step on the high-pass filtered image.

Homodyne filtering [23, 25], phase unwrapping [27] and the hybrid [26] algorithms all rely on information from neighbouring voxels to unwrap each voxel. Recently, Feng et al [30] proposed a phase unwrapping algorithm, CAMPUS, which unwraps voxels individually based on a multi-echo acquisition. By acquiring multiple echoes, with a very short echo spacing, the evolution of the phase for each voxel can be observed. The first echo serves as a reference point from which the change in phase in subsequent echoes is calculated. Assuming the phase at each voxel does not evolve faster than $\pm\pi$ between adjacent echoes, CAMPUS is able to correctly resolve the phase in regions of high gradients where previously mentioned methods struggle. The MR sequence employed is a 3D bipolar gradient echo sequence with flow compensation in all three directions for the first echo, flow compensation in the readout direction for the other odd echoes, and no

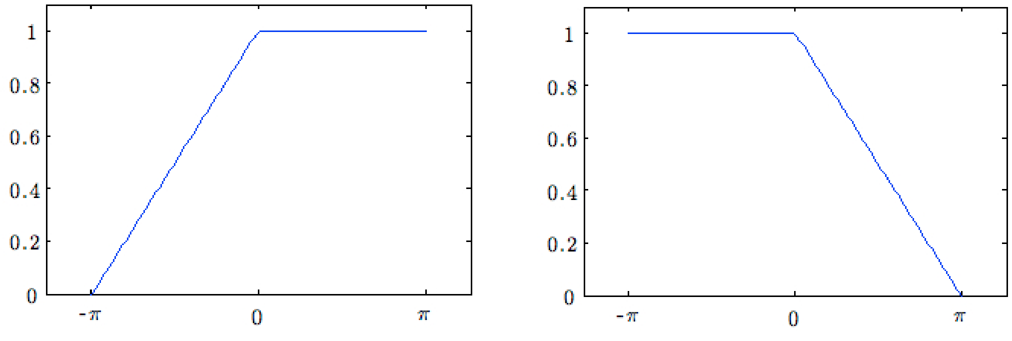

(a)

(b)

Figure 6: Susceptibility-weighted imaging (a) negative and (b) positive phase masks.

flow compensation for the even echoes. This combination of flow compensation allows for the phase effects of flow to be eliminated, however it necessitates the implementation of what is currently a non-standard sequence. As such, although CAMPUS promises greater accuracy and reliability of phase images, it cannot be applied to data acquired with conventional standard sequences available on MR scanners, particularly in the clinical environment.

3.4 PHASE AND MAGNITUDE COMBINATION

The most well-known and commonly utilised MRI technique that combines information from both phase and magnitude is Susceptibility Weighted Imaging (SWI) [23, 31]. SWI uses the relative phase values to attenuate voxels in the magnitude image. A negative mask is created using the phase image by setting positive phase values to unity (or 1) and linearly rescaling the range $[-\pi, 0]$ to the range $[0, 1]$.

$$f_m^- = \begin{cases} \frac{\pi+\phi}{\pi}, & \phi < 0 \\ 1, & \phi \geq 0 \end{cases} \tag{3.7}$$

where f_m^- is the negative phase mask and ϕ is the phase of the voxel. Similarly, a positive mask is defined as

$$f_m^+ = \begin{cases} 1, & \phi < 0 \\ \frac{\pi-\phi}{\pi}, & \phi \geq 0 \end{cases} \tag{3.8}$$

where negative phase values are set to unity and the range $[0, +\pi]$ is linearly scaled to $[0, 1]$.

The magnitude image is multiplied by the mask n times to attenuate the voxels of negative phase, where n has been found to produce optimum contrast when it is between 3 and 5 [31].

$$s = \rho \left(f_m\right)^n . \tag{3.9}$$

Here, s is the SWI image intensity, ρ is the magnitude of the voxel and f_m is f_m^- or f_m^+.

The method was originally devised as a technique for suppressing peripheral veins in angiograms where contrast agents had enhanced both arteries and veins in the magnitude image [23]. Though the arteries and veins are indistinguishable in the magnitude image, the effects of deoxyhaemoglobin in venous blood results in veins parallel to the field having a more negative phase value than arteries. Thus the phase image could be used to attenuate the voxels in the magnitude image that represents venous vessels. This work led to the usage of SWI as a method for MR venography [32, 33]. It has also been applied in applications such as tumour and lesion identification, stroke assessment, haemorrhage detection and quantification of iron content [34, 35, 36, 37].

Abduljalil et al [9] evaluated a different method to combine the information from phase images with magnitude images. Having noted reduced GM/WM contrast in magnitude images and increased GM/WM contrast in phase images acquired with gradient echo sequences, they sought to determine whether the phase contrast could be used to increase the contrast in the magnitude image. They proposed to achieve this by multiplying the magnitude image by the phase image 2-3 times, without performing the SWI mask transformations. Their results, however, showed little added benefit compared to the phase image.

Fripp et al [38] took a different approach to combining information from phase and magnitude images. Rather than create a new contrast image, they used the information in both images to perform segmentation of the bones in the knee joint based on texture details. The algorithm involves training a Support Vector Machine (SVM) using features extracted from manually segmented images, then using an Active Snake Model (ASM) to segment the image based on classifications produced by the SVM. The algorithm performs well, with the combined phase and magnitude information providing better classification and ultimately improved segmentation.

While this thesis is focussed on the use of phase in structural MRI, it is worth noting that functional MRI (fMRI) studies have also investigated the benefits of utilising the full complex data rather than just magnitude [39, 40]. In traditional fMRI, activation maps are created based on intensity changes in the magnitude as a result of the fluctuation in deoxyhaemoglobin concentration that is linked to neural activity. If the signal-to-noise ratio (SNR) in the magnitude image is low, there is an increased chance of incorrectly labelling voxels as active [40]. By including the deoxyhaemoglobin effect in phase in the assessment of activation, the chance of incorrectly labelling a voxel in the activation map is reduced. Rowe et al [40] demonstrated that at high SNR, the accuracy of fMRI activation maps based on complex data is comparable to those based solely on magnitude data . However at low SNR, complex-based activation maps performed better than magnitude-only maps. It may therefore be possible to increase the resolution in fMRI studies while maintaining the reliability of the data by combining the phase information with magnitude.

3.5 QUANTITATIVE SUSCEPTIBILITY MAPPING

The combination of Eqs (2.6) and (2.23) provides the relationship between the phase image intensity and the change in magnetic flux density in a given voxel

$$\phi\left(\boldsymbol{r}\right) = -\gamma\left(\boldsymbol{r}\right).\Delta B\left(\boldsymbol{r}\right).\mathrm{TE}. \tag{3.10}$$

Since ΔB is dependent on magnetic susceptibility, χ, it is theoretically possible to derive voxel-wise magnetic susceptibility estimates from the phase information, a recent area of research known as Quantitative Susceptibility Mapping (QSM).

Attempts to quantify susceptibility using magnetic resonance imaging can be traced back to the 1980's when the susceptibility differences associated with large abnormal pathologies, such as haematomas and tumours, were shown to produce contrast on phase images [41, 42, 43]. Further efforts were made in the 1990's to derive bulk susceptibility values from the phase data, primarily focussing on large objects with known morphology, such as the liver, and assuming uniform susceptibility within. Various methods, such as finite element and Fourier-based convolution, were used to model the observed magnetic B field perturbations induced by arbitrarily-shaped objects [44, 45, 46, 47, 48]. In particular, the Fourier-based convolution method assumed a spherical model for the susceptibility elements. This spherical model of susceptibility effects extended into the area of field estimation [49, 24, 50], where the model was used to predict field perturbations due to arbitrary susceptibility distributions, rather than uniform susceptibility distributions over arbitrary shapes. At the same time, Li and Leigh [51] demonstrated using a numerical phantom that an arbitrary susceptibility distribution could be calculated from known B field perturbation data by solving a large linear system using a singular value decomposition method. Unfortunately, the scaling of the method was limited by exponential increases in computation and memory requirements. Advances in high field MR technology led to increased phase contrast [8], from which field perturbation maps with intricate structural detail could be calculated. This allowed for the susceptibility derivation paradigm as a linear system with voxels modelled as spheres to prevail.

Current QSM methods model the relationship between the change in B field and susceptibility as

$$\Delta B\left(\boldsymbol{r}\right) = \left(\Delta\chi \otimes F_S\right)\left(\boldsymbol{r}\right) \tag{3.11}$$

where $\Delta B\left(\boldsymbol{r}\right)$ is the change in B field at voxel $\boldsymbol{r}$ (the field map), $\Delta\chi$ is the change in susceptibility, $\otimes$ is the convolution operation and F_S is the spherical model kernel based on the change in B induced by a sphere. Implied in this model is, as previously mentioned, the assumption that the spherical model is valid for all voxels. Furthermore, these current methods ignore the effects of chemical exchange on phase. Due to characteristics of the spherical kernel, the system described by (3.11) is under-determined and presents a challenge to which several approaches to QSM have been proposed: thresholded k-space kernel methods [52, 53, 54], calculation of susceptibility through multiple orientation sampling (COSMOS) [55] and regularisation-based methods [56, 57, 58, 59]. While these methods have achieved varying degrees of success in the estimation of susceptibility, the fundamental assumptions that all voxels can be modelled as spheres and that the effects of chemical exchange are negligible are limited, with research suggesting that the effects of these assumptions are not insubstantial [13, 60, 61, 12, 62, 63, 64, 11, 65, 66]. In Chapter 7, we explore the appropriateness of the spherical model and present a new method of QSM that incorporates spherical and cylindrical modelling in the estimation of magnetic susceptibility.

BIBLIOGRAPHY

[1] Jie Luo, Xiang He, D. Andre′ d'Avignon, Joseph J. H. Ackerman, and Dmitriy A. Yablonskiy. Protein-induced water 1H MR frequency shifts: contributions from magnetic susceptibility and exchange effects. *Journal of Magnetic Resonance*, 202(1):102–108, January 2010.

[2] José P. Marques, Rajika Maddage, Vladimir Mlynarik, and Rolf Gruetter. On the origin of the MR image phase contrast: An in vivo MR microscopy study of the rat brain at 14.1 t. *NeuroImage*, 46(2):345–352, June 2009.

[3] Kathryn E. Hammond, Janine M. Lupo, Duan Xu, Meredith Metcalf, Douglas A. C. Kelley, Daniel Pelletier, Susan M. Chang, Pratik Mukherjee, Daniel B. Vigneron, and Sarah J. Nelson. Development of a robust method for generating 7.0 t multichannel phase images of the brain with application to normal volunteers and patients with neurological diseases. *Neuroimage*, 39(4):1682–1692, 2008.

[4] Kathryn E. Hammond, Meredith Metcalf, Lucas Carvajal, Darin T. Okuda, Radhika Srinivasan, Dan Vigneron, Sarah J. Nelson, and Daniel Pelletier. Quantitative in vivo magnetic resonance imaging of multiple sclerosis at 7 tesla with sensitivity to iron. *Annals of Neurology*, 64(6):707–713, 2008.

[5] Bradley P. Thomas, E. Brian Welch, Blake D. Niederhauser, William O. Whetsell, Adam W. Anderson, John C. Gore, Malcolm J. Avison, and Jeffrey L. Creasy. High-resolution 7T MRI of the human hippocampus in vivo. *Journal of Magnetic Resonance Imaging: JMRI*, 28(5):1266–72, November 2008.

[6] Jens M. Theysohn, O. Kraff, S. Maderwald, M.U. Schlamann, A. de Greiff, M. Forsting, S.C. Ladd, M.E. Ladd, and E.R. Gizewski. The human hippocampus at 7T - in vivo MRI. *Hippocampus*, 19(1):1–7, 2009.

[7] Bing Yao, Tie-Qiang Li, Peter van Gelderen, Karin Shmueli, Jacco A. de Zwart, and Jeff H. Duyn. Susceptibility contrast in high field MRI of human brain as a function of tissue iron content. *NeuroImage*, 44(4):1259–1266, February 2009.

[8] Jeff H. Duyn, Peter van Gelderen, Tie-Qiang Li, Jacco A. de Zwart, Alan P. Koretsky, and Masaki Fukunaga. High-field MRI of brain cortical substructure based on signal phase. *Proceedings of the National Academy of Sciences*, 104(28):11796–11801, July 2007.

[9] Amir M. Abduljalil, Petra Schmalbrock, Vera Novak, and Donald W. Chakeres. Enhanced gray and white matter contrast of phase susceptibility-weighted images in ultra-high-field magnetic resonance imaging. *Journal of Magnetic Resonance Imaging*, 18(3):284–290, 2003.

[10] Zang-Hee Cho, Young-Bo Kim, Jae-Yong Han, Hoon-Ki Min, Kyoung-Nam Kim, Sang-Han Choi, Eugene Veklerov, and Larry A. Shepp. New brain atlas - mapping the human brain in vivo with 7.0 t MRI and comparison with post-mortem histology: Will these images change modern medicine? *International Journal of Imaging Systems and Technology*, 18(1):2–8, 2008.

[11] Xiang He and Dmitriy A. Yablonskiy. Biophysical mechanisms of phase contrast in gradient echo MRI. *Proceedings of the National Academy of Sciences*, 106(32):13558–13563, 2009.

[12] Jongho Lee, Karin Shmueli, Byeong-Teck Kang, Bing Yao, Masaki Fukunaga, Peter van Gelderen, Sara Palumbo, Francesca Bosetti, Afonso C. Silva, and Jeff H. Duyn. The contribution of myelin to magnetic susceptibility-weighted contrasts in high-field MRI of the brain. *NeuroImage*, 59(4):3967–3975, February 2012.

[13] Kai Zhong, Jochen Leupold, Dominik von Elverfeldt, and Oliver Speck. The molecular basis for gray and white matter contrast in phase imaging. *Neuroimage*, 40(4):1561–1566, 2008.

[14] J.C. de Munck, R. Bhagwandien, S.H. Muller, F.C. Verster, and M.B. Van Herk. The computation of MR image distortions caused by tissue susceptibility using the boundary element method. *Medical Imaging, IEEE Transactions on*, 15(5):620–627, 1996.

[15] John F. Schenck. The role of magnetic susceptibility in magnetic resonance imaging: MRI magnetic compatibility of the first and second kinds. *Medical Physics*, 23(6):815–850, June 1996.

[16] Dardo G. Tomasi and Ruiliang Wang. Induced magnetic field gradients and forces in the human head in MRI. *Journal of Magnetic Resonance Imaging*, 26(5):1340–1345, 2007.

[17] Karin Shmueli, David L. Thomas, and Roger J. Ordidge. Design, construction and evaluation of an anthropomorphic head phantom with realistic susceptibility artifacts. *Journal of Magnetic Resonance Imaging*, 26(1):202–207, 2007.

[18] Marcus K. Peprah, Garrett W. Astary, Thomas H. Mareci, and Mark W. Meisel. Absolute magnetic susceptibility of rat brain tissue. *Magnetic Resonance in Medicine*, page In Press, 2013.

[19] E. Mark Haacke, Robert W. Brown, Michael R. Thompson, and Ramesh Venkatesan. *Magnetic Resonance Imaging: Physical Principles and Sequence Design*. John Wiley & Sons, Inc, New York, 1999.

[20] E. Mark Haacke, Norman Y.C. Cheng, Michael J. House, Qiang Liu, Jaladhar Neelavalli, Robert J. Ogg, Asadullah Khan, Muhammad Ayaz, Wolff Kirsch, and Andre Obenaus. Imaging iron stores in the brain using magnetic resonance imaging. *Magnetic Resonance Imaging*, 23(1):1–25, January 2005.

[21] Robert J. Ogg, James W. Langston, E. Mark Haacke, R. Grant Steen, and June S. Taylor. The correlation between phase shifts in gradient-echo MR images and regional brain iron concentration. *Magnetic Resonance Imaging*, 17(8):1141–1148, October 1999.

[22] Devesh Raj, Derek P. Paley, Adam W. Anderson, Richard P. Kennan, and John C. Gore. A model for susceptibility artefacts from respiration in functional echo-planar magnetic resonance imaging. *Physics in Medicine and Biology*, 45(12):3809–3820, 2000.

[23] Y. Wang, Y. Yu, D. Li, K.T. Bae, J.J. Brown, W. Lin, and E.M. Haacke. Artery and vein separation using susceptibility-dependent phase in contrast-enhanced MRA. *Journal of Magnetic Resonance Imaging*, 12(5):661–670, 2000.

[24] R. Salomir, B. D. de Senneville, and C. T. Moonen. A fast calculation method for magnetic field inhomogeneity due to an arbitrary distribution of bulk susceptibility. *Concepts in Magnetic Resonance Part B: Magnetic Resonance Engineering*, 19B(1):26–34, 2003.

[25] D.C. Noll, D.G. Nishimura, and A. Macovski. Homodyne detection in magnetic resonance imaging. *Medical Imaging, IEEE Transactions on*, 10(2):154–163, 1991.

[26] Alexander Rauscher, Markus Barth, Karl-Heinz Herrmann, Stephan Witoszynskyj, Andreas Deistung, and Jürgen R Reichenbach. Improved elimination of phase effects from background field inhomogeneities for susceptibility weighted imaging at high magnetic field strengths. *Magnetic Resonance Imaging*, 26(8):1145–1151, October 2008.

[27] Mark Jenkinson. Fast, automated, n-dimensional phase-unwrapping algorithm. *Magnetic Resonance in Medicine*, 49(1):193–197, January 2003.

[28] Stephan Witoszynskyj, Alexander Rauscher, Jürgen R. Reichenbach, and Markus Barth. Phase unwrapping of MR images using [Phi]UN - a fast and robust region growing algorithm. *Medical Image Analysis*, 13(2):257–268, April 2009.

[29] Marvin A. Schofield and Yimei Zhu. Fast phase unwrapping algorithm for interferometric applications. *Optics Letters*, 28(14):1194–1196, July 2003.

[30] Wei Feng, Jaladhar Neelavalli, and E. Mark Haacke. Catalytic multiecho phase unwrapping scheme (CAMPUS) in multiecho gradient echo imaging: Removing phase wraps on a voxel-by-voxel basis. *Magnetic Resonance in Medicine*, (1):117–126, July 2012.

[31] E. Mark Haacke, Yingbiao Xu, Yu-Chung N. Cheng, and Jürgen R. Reichenbach. Susceptibility weighted imaging (SWI). *Magnetic Resonance in Medicine*, 52(3):612–618, 2004.

[32] Peter Koopmans, Rashindra Manniesing, Wiro Niessen, Max Viergever, and Markus Barth. MR venography of the human brain using susceptibility weighted imaging at very high field strength. *Magnetic Resonance Materials in Physics, Biology and Medicine*, 21(1):149–158, 2008.

[33] Jürgen R Reichenbach and E. Mark Haacke. High-resolution BOLD venographic imaging: a window into brain function. *NMR in Biomedicine*, 14(7-8):453–467, 2001.

[34] Vivek Sehgal, Zachary Delproposto, E. Mark Haacke, Karen A. Tong, Nathaniel Wycliffe, Daniel K. Kido, Yingbiao Xu, Jaladhar Neelavalli, Djamel Haddar, and Jürgen R Reichenbach. Clinical applications of neuroimaging with susceptibility-weighted imaging. *Journal of Magnetic Resonance Imaging*, 22(4):439–450, 2005.

[35] E. Mark Haacke, Muhammad Ayaz, Asadullah Khan, Elena S. Manova, Bharani Krishnamurthy, Lakshman Gollapalli, Carlo Ciulla, I. Kim, Floyd Petersen, and Wolff Kirsch. Establishing a baseline phase behavior in magnetic resonance imaging to determine normal vs. abnormal iron content in the brain. *Journal of Magnetic Resonance Imaging*, 26(2):256–264, 2007.

[36] Andreas Deistung, Hans-Joachim Mentzel, Alexander Rauscher, Stephan Witoszynskyj, Werner A Kaiser, and Jürgen R Reichenbach. Demonstration of paramagnetic and diamagnetic cerebral lesions by using susceptibility weighted phase imaging (SWI). *Z Med Phys*, 16(4):261–7, 2006.

[37] Marc Hermier and Norbert Nighoghossian. Contribution of susceptibility-weighted imaging to acute stroke assessment. *Stroke*, 35(8):1989–1994, 2004.

[38] Jurgen Fripp, Pierrick Bourgeat, Stuart Crozier, and Sebastien Ourselin. Segmentation of the bones in MRIs of the knee using phase, magnitude, and shape information. *Academic Radiology*, 14(10):1201–1208, October 2007.

[39] Jongho Lee, Morteza Shahram, Armin Schwartzman, and John M. Pauly. Complex data analysis in high-resolution SSFP fMRI. *Magnetic Resonance in Medicine*, 57(5):905–917, 2007.

[40] Daniel B. Rowe and Brent R. Logan. A complex way to compute fMRI activation. *NeuroImage*, 23(3):1078–1092, November 2004.

[41] D Faul, J Arbart, and P Margosian. Quick measurement of magnetic field variations within the body. *Radiology*, 153:303–4, 1984.

[42] I. J. Cox, G. M. Bydder, D. G. Gadian, I. R. Young, E. Proctor, S. R. Williams, and Ian Hart. The effect of magnetic susceptibility variations in NMR imaging and nmr spectroscopy in vivo. *Journal of Magnetic Resonance (1969)*, 70(1):163–168, October 1986.

[43] I. R Young, S. Khenia, D. G. T Thomas, C. H Davis, D. G Gadian, I. J Cox, B. D Ross, and G. M Bydder. Clinical magnetic susceptibility mapping of the brain. *Journal of Computer Assisted Tomography*, 11(1):2–6, January 1987.

[44] Robert M. Weisskoff and Suzanne Kiihne. MRI susceptometry: Image-based measurement of absolute susceptibility of MR contrast agents and human blood. *Magnetic Resonance in Medicine*, 24(2):375–383, April 1992.

[45] R. Bhagwandien, M.A. Moerland, C.J.G. Bakker, R. Beersma, and J.J.W. Lagendijk. Numerical analysis of the magnetic field for arbitrary magnetic susceptibility distributions in 3D. *Magnetic Resonance Imaging*, 12(1):101–107, 1994.

[46] Randall W. Holt, Pedro J. Diaz, Jeffrey L. Duerk, and Errol M. Bellon. MR susceptometry: an external-phantom method for measuring bulk susceptibility from field-echo phase reconstruction maps. *Journal of Magnetic Resonance Imaging*, 4(6):809–818, November 1994.

[47] O. Beuf, A. Briguet, M. Lissac, and R. Davis. Magnetic resonance imaging for the determination of magnetic susceptibility of materials. *Journal of Magnetic Resonance, Series B*, 112(2):111–118, August 1996.

[48] Zhiyue J. Wang, Shuchun Li, and John C. Haselgrove. Magnetic resonance imaging measurement of volume magnetic susceptibility using a boundary condition. *Journal of Magnetic Resonance*, 140(2):477–481, October 1999.

[49] Christopher M. Collins, Bei Yang, Qing X. Yang, and Michael B. Smith. Numerical calculations of the static magnetic field in three-dimensional multi-tissue models of the human head. *Magnetic Resonance Imaging*, 20(5):413–424, June 2002.

[50] JP Marques and R Bowtell. Application of a fourier-based method for rapid calculation of field inhomogeneity due to spatial variation of magnetic susceptibility. *Concepts in Magnetic Resonance Part B: Magnetic Resonance Engineering*, 25B(1):78, 65, April 2005.

[51] Lin Li and John S. Leigh. Quantifying arbitrary magnetic susceptibility distributions with MR. *Magnetic Resonance in Medicine*, 51(5):1077–1082, May 2004.

[52] Karin Shmueli, Jacco A. de Zwart, Peter van Gelderen, Tie-Qiang Li, Stephen J. Dodd, and Jeff H. Duyn. Magnetic susceptibility mapping of brain tissue in vivo using MRI phase data. *Magnetic Resonance in Medicine*, 62(6):1510–1522, December 2009.

[53] Wei Li, Bing Wu, and Chunlei Liu. Quantitative susceptibility mapping of human brain reflects spatial variation in tissue composition. *NeuroImage*, 55(4):1645–1656, April 2011.

[54] Sam Wharton, Andreas Schäfer, and Richard Bowtell. Susceptibility mapping in the human brain using threshold-based k-space division. *Magnetic Resonance in Medicine*, 63(5):1292–1304, 2010.

[55] Tian Liu, Pascal Spincemaille, Ludovic de Rochefort, Bryan Kressler, and Yi Wang. Calculation of susceptibility through multiple orientation sampling (COSMOS): a method for conditioning the inverse problem from measured magnetic field map to susceptibility source image in MRI. *Magnetic Resonance in Medicine*, 61(1):196–204, January 2009.

[56] B Kressler, L de Rochefort, T Liu, P Spincemaille, Q Jiang, and Y Wang. Nonlinear regularization for per voxel estimation of magnetic susceptibility distributions from MRI field maps. *IEEE Transactions on Medical Imaging*, June 2009.

[57] Ludovic de de Rochefort, Tian Liu, Bryan Kressler, Jing Liu, Pascal Spincemaille, Vincent Lebon, Jianlin Wu, and Yi Wang. Quantitative susceptibility map reconstruction from MR phase data using bayesian regularization: Validation and application to brain imaging. *Magnetic Resonance in Medicine*, 63(1):194–206, 2010.

[58] Tian Liu, Jing Liu, Ludovic de Rochefort, Pascal Spincemaille, Ildar Khalidov, James Robert Ledoux, and Yi Wang. Morphology enabled dipole inversion (MEDI) from a single-angle acquisition: Comparison with COSMOS in human brain imaging. *Magnetic Resonance in Medicine*, 66(3):777–783, 2011.

[59] Ferdinand Schweser, Karsten Sommer, Andreas Deistung, and Jürgen Rainer Reichenbach. Quantitative susceptibility mapping for investigating subtle

susceptibility variations in the human brain. *NeuroImage*, 62(3):2083–2100, September 2012.

[60] Christian Denk, Enedino Hernandez Torres, Alex MacKay, and Alexander Rauscher. The influence of white matter fibre orientation on MR signal phase and decay. *NMR in Biomedicine*, 24(3):246–252, 2011.

[61] Pascal Sati, Afonso C. Silva, Peter van Gelderen, Maria I. Gaitan, Jillian E. Wohler, Steven Jacobson, Jeff H. Duyn, and Daniel S. Reich. In vivo quantification of T2* anisotropy in white matter fibers in marmoset monkeys. *NeuroImage*, 59(2):979–985, January 2012.

[62] Wei Li, Bing Wu, Alexandru V. Avram, and Chunlei Liu. Molecular underpinnings of magnetic susceptibility anisotropy in the brain white matter. In *Proceedings of the ISMRM 20th Annual Meeting*, page 0379, May 2012.

[63] Jie Luo, Xiang He, and Dmitriy A Yablonskiy. Magnetic susceptiblity induced MR signal frequency shift in white matter - experimental comparison between lorentzian sphere and generalized lorentzian approaches. In *Proceedings of the ISMRM 20th Annual Meeting*, page 0415, Melbourne, Australia, May 2012.

[64] Sharon K. Schreiber, Bradley D. Clymer, Michael V. Knopp, and Petra Schmalbrock. 7T susceptibility sensitive imaging detects microarchitectural white matter differences across the healthy corpus callosum. In *Proceedings of the ISMRM 20th Annual Meeting*, page 2367, Melbourne, Australia, May 2012.

[65] Jongho Lee, Karin Shmueli, Masaki Fukunaga, Peter van Gelderen, Hellmut Merkle, Afonso C. Silva, and Jeff H. Duyn. Sensitivity of MRI resonance frequency to the orientation of brain tissue microstructure. *Proceedings of the National Academy of Sciences*, 107(11):5130–5135, March 2010.

[66] Karin Shmueli, Stephen J. Dodd, Tie-Qiang Li, and Jeff H. Duyn. The contribution of chemical exchange to MRI frequency shifts in brain tissue. *Magnetic Resonance in Medicine*, 65(1):35–43, 2011.

Part II

NOVEL RESEARCH

4

SPATIALLY DEPENDENT FILTERING

A METHOD FOR REMOVAL OF PHASE DISTORTIONS AT THE CORTICAL SURFACE

Ideally, processing of wrapped phase data should maximise retention of structural detail, eliminate the bias field and avoid artefacts at the surface of the brain. Surface artefacts appear as intensity inhomogeneities in the processed phase images, often obscuring underlying structural detail. They are a result of insufficient estimation, during phase processing, of the large phase changes contributed by the bias field and susceptibility differences at air-tissue and bone-tissue interfaces. The ability of phase processing methods to address these requirements has a direct effect on post processing techniques such as SWI [1, 2] and susceptibility mapping [3, 4, 5].

This chapter presents a spatially dependent filtering method that adjusts filter parameters according to a voxel's location while performing computationally efficient filtering of the phase unwrapped or complex filtered phase images. Our aim is to remove surface artefacts with higher computational efficiency than the hybrid method. The method is applied to 3T cortical and 7T cortical and subcortical data and is shown to substantially improve removal of surface artefacts, thus enhancing the usefulness and reliability of phase data for visual interpretation and phase-dependent image processing techniques.

4.1 BACKGROUND

Generating phase images relies on image processing methods beyond calculating the phase angle of the complex data. Processing of phase images is confounded by two characteristics of the phase data: (i) phase wrapping, where the true, or unwrapped, phase angles, $\boldsymbol{\phi}_U$, are wrapped into the interval $[-\pi, \pi)$, such that

$$\boldsymbol{\phi}_U = \angle \boldsymbol{C} + 2\pi \boldsymbol{K} \tag{4.1}$$

where $\angle \boldsymbol{C}$ means the argument of the complex values, $\boldsymbol{C}$, and $\boldsymbol{K}$ is a map of voxel-wise integer values representing the wrapping order; and (ii) a background field,

$\boldsymbol{\phi}_B$, comprising surface artefacts and bias field, which tend to be spatially slowly varying compared to the sought after information contained in the local field, $\boldsymbol{\phi}_L$, where

$$\boldsymbol{\phi}_U = \boldsymbol{\phi}_B + \boldsymbol{\phi}_L. \tag{4.2}$$

Removal of the phase wraps and the background field is undertaken using either complex, or homodyne, filtering [6] or phase unwrapping followed by subtraction of the estimated background field [7].

Phase unwrapping techniques are applicable to several fields ranging from MRI [8, 9, 10] to Synthetic Aperture Radar Interferometry [11, 12]. The techniques require precise detection of phase wraps and effective handling of singularities [12]. As robust phase unwrapping methods tend to have long computation times, efforts have been made to increase their computational efficiency [13, 14].

Several methods have been proposed for the estimation and removal of the background field. High pass filtering [7] is achieved by subtracting a low pass filtered (LPF) unwrapped phase data from the original unwrapped phase data:

$$\boldsymbol{\phi}_L^{\mathrm{LPF}} = \boldsymbol{\phi}_U - \mathrm{LPF}\left(\boldsymbol{\phi}_U\right). \tag{4.3}$$

This phase processing method produces artefacts near the cortical surface of the brain, since the intensities of non-brain voxels are included in the background field estimate. Polynomial fitting [15] involves the estimation of the bias field by fitting n-th order polynomials to the data. A higher order n allows better estimation of the field, particularly the higher gradients near the cortex, however they may also incorrectly estimate the bias field near large structures. Spherical mean estimation [16] exploits the physical property that fields produced by sources outside of a volume of interest (VOI) are harmonic throughout the VOI and therefore satisfy Laplace's equation

$$\nabla^2 B = 0. \tag{4.4}$$

Fields due to sources within the VOI are not harmonic, and therefore the Laplace operator can theoretically be used to separate the external, or bias, field from the internal, or local, field. Outside of the brain, phase values are zero and therefore the field is unknown. Here, application of this method will fail, leading to incorrect bias field estimation near the cortex. Dipole fitting [17, 18] seeks to estimate the bias field by assuming that it can be modelled by dipoles positioned at each voxel outside of the brain. A brain mask is defined and the optimal arrangement of dipoles outside of the brain is determined, such that the net magnetic field effect of those dipoles approximates the phase-derived magnetic field inside the brain. The accuracy of this method is particularly sensitive to the brain mask, particularly near the cortex where high field gradients exist. In subsequent publications that use this method [19, 20], significant erosion of the mask at the cortex is apparent, suggesting that the method is inadequate at estimating the bias field in the peripheral voxels.

Complex filtering takes a different approach to the task of unwrapping phase and removing the background field. The local field is computed as

$$\boldsymbol{\phi}_L^{\mathrm{COM}} = \angle \boldsymbol{C} - \angle \mathrm{LPF}\left(\boldsymbol{C}\right) \tag{4.5}$$

where the low pass filtering operation is applied to the complex data. This method avoids singularity problems, has less surface artefact and is faster to compute compared to the high pass filtering method. However, compromises must be made between information retention, requiring a larger image space filter size, and phase wrap removal, requiring a smaller image space filter size [21].

Although complex filtering produces less surface artefact than high pass filtering methods, further processing is required to remove remaining artefact. Attempts have been made at removing these inhomogeneities from unwrapped phase data by deriving better estimates of the background field and surface artefact. One method, aimed specifically at SWI applications, employs local field gradients to measure the severity of the inhomogeneities and applies these measurements to the creation of the SWI phase mask in order to suppress the effects of large inhomogeneities [22]. Another method uses geometrical models derived from the magnitude data to calculate estimations of inhomogeneities induced by susceptibility differences at air-tissue interfaces [23]. While the methods give some benefit in removing surface artefact, the primary aim of both methods is to remove the effects of inhomogeneities in medial areas of the brain and so limited attention is given to assessing their effectiveness in the peripheral areas of the brain.

Recently, a hybrid method was proposed for processing wrapped phase data and reducing the surface artefacts in phase images [24]. This method combines phase unwrapping and complex filtering to better estimate and remove the background field as follows

$$\boldsymbol{\phi}_L^{\mathrm{HYB}} = \boldsymbol{\phi}_U - \left(\angle \mathrm{LPF}\left(\boldsymbol{C}\right)\right)_U . \tag{4.6}$$

The method was shown to improve on traditional phase processing with regards to removal of the surface artefacts; however, limitations exist in areas of steep phase gradient.

4.2 METHOD

4.2.1 *Spatially dependent filtering method*

The brain mask, $\boldsymbol{M}$, is derived from the magnitude image using thresholding to initialise the mask and active contours [25] to optimise the mask, such that,

$$\boldsymbol{M}_{ij} = \begin{cases} 1, & \text{foreground voxel} \\ 0, & \text{background voxel} \end{cases} \tag{4.7}$$

where subscripts ij denote the ij-th voxel, and sufficient separation between brain voxels and skull voxels, both spatially and in intensity, avoids the need for further skull stripping methods. The active contours algorithm evolves the boundary defined by the initial mask based on segmentation of the image, with soft constraints on curvature of the boundary. It is a more reliable method than intensity gradient active contour methods in noisy images, or where blurred edges occur.

The proximity map, $\boldsymbol{P}$, indicates the proximity of the voxel to the brain surface and is derived by applying a 2D Gaussian filter to the mask,

$$\boldsymbol{P}_{ij} = \left(\boldsymbol{F}_{\sigma,2\sigma} * \boldsymbol{M}\right)_{ij} \boldsymbol{M}_{ij} \tag{4.8}$$

where the symbol $*$ represents the convolution operation and $\boldsymbol{F}_{\sigma,2\sigma}$ is a Gaussian filter of standard deviation σ voxels. The second subscript, 2σ, indicates the filter kernel extends to $\pm 2\sigma$ voxels in both dimensions. Larger kernel sizes increase computation time, but also capture more of the Gaussian duty. 2σ, equivalent to 95.5% of Gaussian duty, is chosen as a compromise between filter kernel size and percentage of Gaussian duty. The values of $\boldsymbol{P}$ reside in the interval [0,1] and the standard deviation, σ, is chosen to ensure removal of the background field while maintaining the detail in the local field.

The alpha map, $\boldsymbol{\alpha}$, represents spatially dependent standard deviations which are computed as

$$\boldsymbol{\alpha}_{ij} = \sigma \left(\boldsymbol{P}_{ij}^{n}\right)_{2} \boldsymbol{M}_{ij} \tag{4.9}$$

where exponentiation is element-wise. $\left(\boldsymbol{P}_{ij}^{n}\right)_{2}$ indicates that $\boldsymbol{P}_{ij}^{n}$ is rounded to two decimal places, giving a maximum of N=101 unique values in $\boldsymbol{\alpha}$. The exponent n is calculated so that the Gaussian filter defined by $\boldsymbol{\alpha}_{ij}$ is large enough to incorporate values from the adjacent voxels, and small enough to effectively estimate surface artefact. A constraint is therefore imposed such that $\boldsymbol{\alpha}_{ij} = 1$ when proximity $\boldsymbol{P}_{ij} =$

0.5. That is, when a voxel's neighbourhood is equally split between brain and non-brain voxels. From Eq. (4.9),

$$1 = \sigma 0.5^n. \tag{4.10}$$

The exponent n is thus given by

$$n = \frac{-\log \sigma}{\log 0.5}. \tag{4.11}$$

We define $\boldsymbol{A} = \{\alpha_1, \ldots, \alpha_N\}$ as this set of unique values in increasing order, such that $\alpha_1 = \min(\boldsymbol{A})$ and $\alpha_N = \max(\boldsymbol{A})$.

An index map, $\boldsymbol{X}$, relates $\boldsymbol{\alpha}_{ij}$ to $\boldsymbol{A}$, such that

$$\boldsymbol{X}_{ij} = k, \qquad \text{where } \boldsymbol{\alpha}_{ij} = \alpha_k. \tag{4.12}$$

A set of low pass filtered images, $\boldsymbol{\Phi} = \{\phi_1, \ldots, \phi_N\}$, is constructed from $\boldsymbol{A}$, where ϕ_k is derived using only brain voxels identified by the mask, $\boldsymbol{M}$, and standard deviation α_k in the filtering calculation:

$$\boldsymbol{\phi}_k = \frac{\boldsymbol{F}_{\alpha_k, 2\sigma} * (\boldsymbol{\phi} \cdot \boldsymbol{M})}{\boldsymbol{F}_{\alpha_k, 2\sigma} * \boldsymbol{M}}. \tag{4.13}$$

Here, $\boldsymbol{\phi}$ is the phase image obtained by either the phase unwrapping method, $\boldsymbol{\phi}_U$, or the complex filtering method, $\boldsymbol{\phi}_L^{\text{COM}}$. Division and multiplication are element-wise operations.

The spatially dependent filtered background field estimate, $\boldsymbol{\phi}_B^{\text{SDF}}$, is constructed from the $\boldsymbol{\Phi}$ image set and index map, $\boldsymbol{X}$:

$$\boldsymbol{\phi}_{B,ij}^{\text{SDF}} = \boldsymbol{\phi}_{k,ij}, \qquad \text{where } k = \boldsymbol{X}_{ij}. \tag{4.14}$$

The spatially dependent filtered phase image containing the detail in the local field, $\boldsymbol{\phi}_L^{\text{SDF}}$, is computed by

$$\boldsymbol{\phi}_L^{\text{SDF}} = \boldsymbol{\phi} - \boldsymbol{\phi}_B^{\text{SDF}}. \tag{4.15}$$

4.2.2 *Simulated data*

A simulated phase dataset was created to illustrate the spatially dependent filtering method. The ground truth data comprised zero phase disc of radius 40 voxels embedded in a 101 × 101 matrix size image (Fig. 7a). The voxel dimensions were chosen as 0.2 × 0.2 × 0.2 mm^3. Fine structural detail was simulated by the addition of three vertical lines of width 1 voxel and phase value 0.1 radians. The background phase was zero radians. A bias field was simulated using a linear ramp ranging vertically from 0 to 0.2 radians, while surface artefacts were assumed to be caused by air tissue interfaces external to the brain [18] and were thus simulated by placing four magnetic dipole moments around the exterior of the disc (Fig. 7b). The change in phase at $\boldsymbol{r}'$ due to a dipole at $\boldsymbol{r}$, $\Delta\boldsymbol{\phi}_d\left(\boldsymbol{r}',\boldsymbol{r}\right)$, was calculated as

$$\Delta\phi_d\left(\boldsymbol{r}',\boldsymbol{r}\right) = -\gamma \mathrm{TE} \Delta \boldsymbol{B}\left(\boldsymbol{r}',\boldsymbol{r}\right) \tag{4.16}$$

where $\Delta\boldsymbol{B}\left(\boldsymbol{r}',\boldsymbol{r}\right)$ is the change in magnetic flux density outside the dipole, given by [26] as

$$\Delta\boldsymbol{B}\left(\boldsymbol{r}',\boldsymbol{r}\right) = \frac{\mu_0}{4\pi}\frac{1}{\left|\boldsymbol{r}-\boldsymbol{r}'\right|^3}\left(3\frac{\boldsymbol{m}\left(\boldsymbol{r}'\right)\cdot\left(\boldsymbol{r}-\boldsymbol{r}'\right)^2}{\left|\boldsymbol{r}-\boldsymbol{r}'\right|^2}\left(\boldsymbol{r}-\boldsymbol{r}'\right)-\boldsymbol{m}\left(\boldsymbol{r}'\right)\right). \tag{4.17}$$

The parameters used are typical of data acquisitions at $\boldsymbol{B}_0$ field strength of 3T: $\gamma = 42.58$ MHz, TE $= 45$ ms, $\mu_0 = 4\pi \times 10^{-7}$. $\boldsymbol{m}\left(\boldsymbol{r}'\right)$ is the magnetic dipole moment, given by

$$\boldsymbol{m}\left(\boldsymbol{r}\right) = 4\pi a \chi\left(\boldsymbol{r}\right)\boldsymbol{H}_0 \tag{4.18}$$

where a is the volume of the voxel, $\chi = -9.05 \times 10^{-6}$ is the susceptibility of water and $\boldsymbol{H}_0 = {}^{B_0}/_{\mu_0}$ is the magnetic field intensity, with direction as indicated in Fig. 7a. The ground truth phase, bias field and surface artefacts were summed to create the simulated phase image (Fig 7c). Spatially dependent filtering was applied with a standard deviation $\sigma = 20$ voxels.

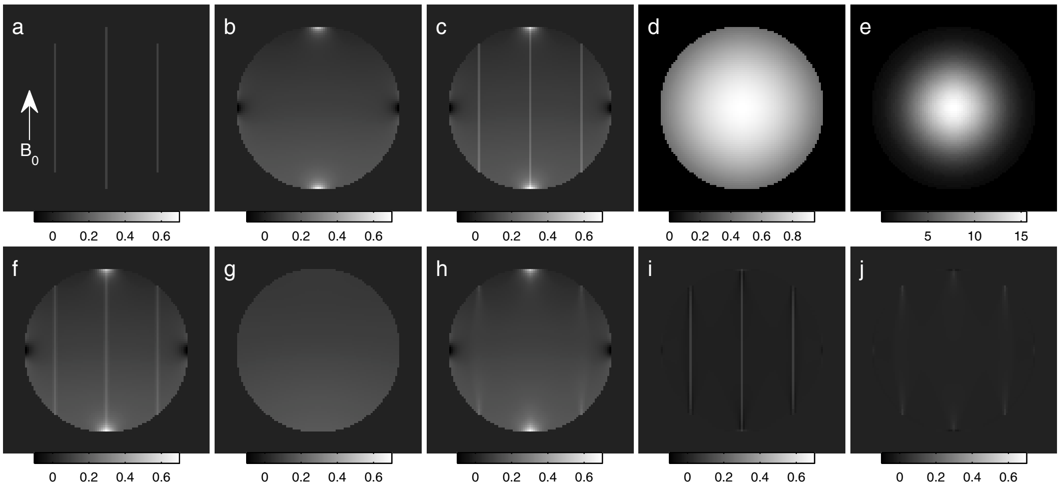

Figure 7: Simulated phase data: (a) The ground truth (rads) was combined with (b) a bias field and surface artefacts (rads) to produce (c) a simulated phase image. Spatially dependent filtering involved creation of (d) the proximity map, (e) the alpha map and the N individual low pass filtered (LPF) phase images, illustrated here using the (f) smallest and (g) largest alpha values. The LPF phase images were combined to produce (h) the spatially dependent filtered background field estimate (rads), which was subtracted from the simulated data to produce (i) the local field image (rads). The difference between the local field image and the ground truth is shown in (j) (rads).

4.2.3 *Experimental Data*

3T data was acquired from a healthy human volunteer using a Siemens TIM Trio 3T system with a Siemens 12 channel Head Matrix Coil (Siemens Medical Solutions, Erlangen, Germany) using the following imaging parameters: axial 2D Gradient Recall Echo, T_2^*-weighted imaging with $\mathrm{TE} = 45$ ms, $\mathrm{TR} = 1000$ ms, flip angle $= 45°$, slice thickness $= 2.5$ mm, $\mathrm{FOV} = 240 \times 180\ \mathrm{mm}^2$, image matrix size $= 448 \times 384$. The magnitude data was reconstructed using SENSE. The wrapped phase data was reconstructed using a phase optimised SENSE method [27].

7T data was acquired from a healthy human volunteer (male, aged 27) on a 7T Siemens system (Siemens Medical Solutions, Erlangen, Germany) with an 8-channel transmit-receive head coil (Neuroscience Research Institute, Incheon, South Korea) using the following parameters: axial 2D gradient echo (GRE), T_2^*-weighted imaging with $\mathrm{TE} = 21.6$ ms, $\mathrm{TR} = 750$ ms, flip angle $= 30°$, bandwidth $= 30$ Hz per pixel, slice thickness $= 2$ mm, $\mathrm{FOV} = 256 \times 224\ \mathrm{mm}^2$, matrix size $= 1024 \times 896$. Spatial resolution was $0.25 \times 0.25 \times 2\ \mathrm{mm}^3$. A total of 17 slices were acquired. The total scan time was 11.5 min. The magnitude and wrapped phase data were reconstructed using the optimised complex reconstruction method [27].

4.2.4 *Comparison of artefact removal*

A 3T axial slice, a 7T superior axial slice and a 7T inferior axial slice were selected for comparison of the phase processing methods (Fig. 8a). Five phase images, $\boldsymbol{\phi}_L^{\mathrm{LPF}}$, $\boldsymbol{\phi}_L^{\mathrm{COM}}$, $\boldsymbol{\phi}_L^{\mathrm{HYB}}$, $\boldsymbol{\phi}_L^{\mathrm{SDF,UP}}$ and $\boldsymbol{\phi}_L^{\mathrm{SDF,COM}}$ were produced for each slice. In construction of each phase image, filter types and sizes were chosen in accordance with the published studies and based on heuristic assessment of the bias field removal and image contrast in the output. In constructing (4.3), unwrapping was achieved using the ΦUN method [28]. The low pass filtering operation involved convolution in image space with a 2D Gaussian kernel with standard deviations, σ, of 5, 10 and 10 voxels for the 3T, 7T superior and 7T inferior axial slice data, respectively. A kernel size extending to $\pm 2\sigma$ in both dimensions was used in each case. $\boldsymbol{\phi}_L^{\mathrm{COM}}$ was constructed using the complex filtering method (4.5), where the low pass filtering of the complex data was achieved using multiplication in k-space with a 2D Gaussian kernel with standard deviation 15, 50 and 20 for the 3T, 7T superior and 7T inferior axial slice data, respectively. For the hybrid method (4.6) phase image, $\boldsymbol{\phi}_L^{\mathrm{HYB}}$, unwrapping was achieved using the ΦUN method, and low pass filtering involved multiplication in k-space with a 2D Hamming window of size 80×80, 100×100 and 125×125, for the 3T, 7T superior and 7T inferior axial slice data, respectively. Brain masks were derived from the magnitude data (Fig. 8b), as described above in Spatially dependent filtering method. $\boldsymbol{\phi}_L^{\mathrm{SDF,UP}}$ was constructed by applying the spatially dependent filtering method to the unwrapped phase data using the same filter kernel size and standard deviation parameter, σ, as for the construction of $\boldsymbol{\phi}_L^{\mathrm{LPF}}$. $\boldsymbol{\phi}_L^{\mathrm{SDF,COM}}$ was constructed by applying the spatially dependent filtering method to the previously obtained complex filtered phase images, $\boldsymbol{\phi}_L^{\mathrm{COM}}$. In applying the spatially dependent filtering method, standard deviations of 25, 5 and 15 voxels were used for the 3T, 7T superior and 7T inferior axial slice data, respectively. The processed phase images were multiplied by the brain mask to improve visualisation of the brain surface voxels.

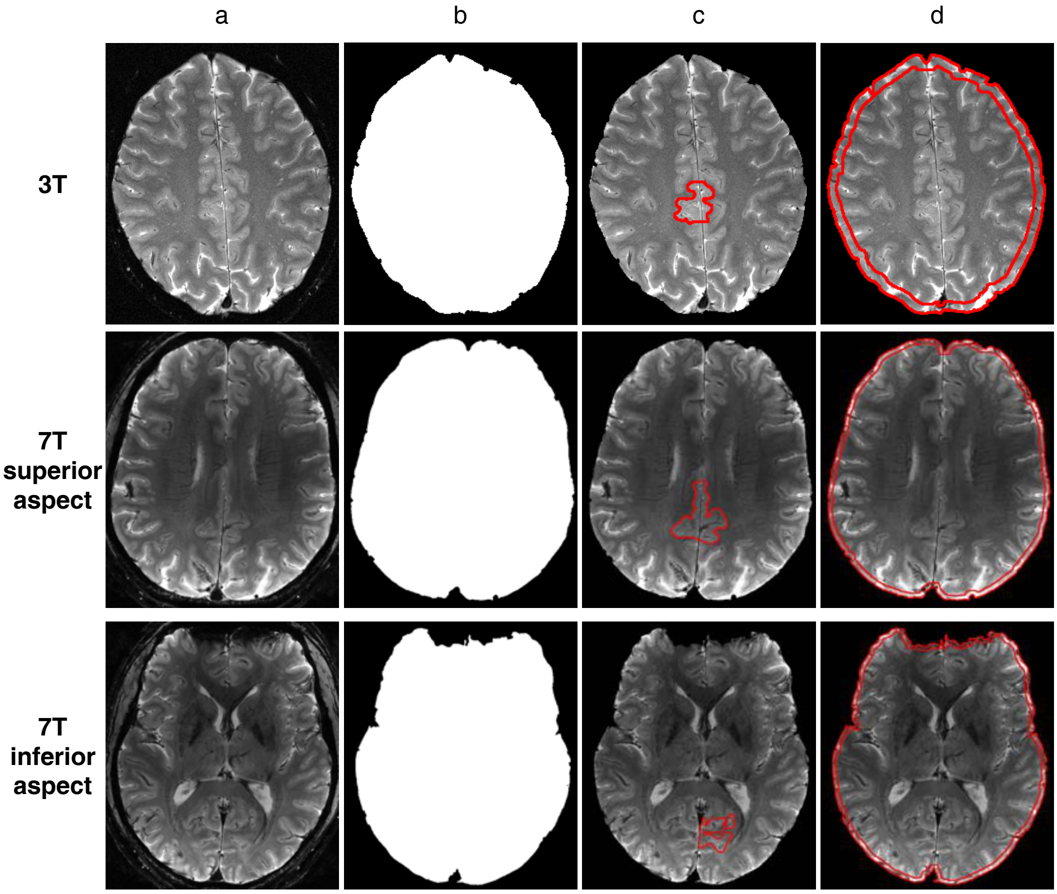

Figure 8: The (a) magnitude image was used to derive the (b) binary foreground/background mask, (c) medial cortical region of interest and (d) lateral cortical region of interest.

The phase images were quantitatively compared by selecting two regions of interest (ROI) comprising predominantly grey matter (GM): (i) a medial cortical ROI unaffected by surface artefacts (Fig. 8c); and (ii) a lateral cortical ROI representing areas affected by surface artefacts (Fig. 8d). The premise of this quantitative comparison is that voxels in the lateral cortical areas have a similar phase intensity distribution to those in the medial cortical areas. For each image, the mean and standard deviation of voxel intensities were calculated for the two ROIs. The ability of each method to remove surface artefact was quantified as the absolute shift in mean

$$\Delta\mu = |\mu_l - \mu_m| \tag{4.19}$$

and the intensity spread ratio

$$R_\sigma = \frac{\sigma_l}{\sigma_m}$$

where μ is the mean and σ is the standard deviation and subscripts l and m represent the lateral and medial ROIs, respectively. A smaller $\Delta\mu$ and an R_σ closer to 1 indicate less surface artefact in the image.

All computations were undertaken and timed using MATLAB on a PC with Intel Core Duo 3.16GHz processors and 8 GB RAM.

4.3 RESULTS

4.3.1 *Application of spatially dependent filtering method to simulated data*

The steps of the spatially dependent filtering method are exemplified by application to the simulated dataset. The proximity map, $\boldsymbol{P}$ (Fig 7d), shows decreasing proximity values from the centre to the edge of the disc. These values are translated into decreasing values in the alpha map, $\boldsymbol{\alpha}$ (Fig 7e). A low pass filtered phase image calculated using the smallest alpha value ($\boldsymbol{\phi}_1$, Fig 7f) demonstrated the ground truth vertical lines, surface artefacts and bias field. In contrast, filtering using the largest alpha value ($\boldsymbol{\phi}_N = 37$, Fig 7g), demonstrated only the bias field. The spatially dependent filtering combination of the low pass filtered phase images estimated the bias field and surface artefacts (Fig 7h) with only minor evidence of the ground truth local detail (vertical lines) appearing near the surface. The estimated local phase image ($\boldsymbol{\phi}_L^{\mathrm{SDF}}$, Fig 7i) accurately replicates the ground truth. Inconsistencies that were insignificant relative to the original artefact appear close to the surface in the difference image (Fig 7j). Line profiles along the central vertical line (Fig 40) demonstrated the greater accuracy in the SDF method compared to standard gaussian filtering.

4.3.2 *Comparison of artefact removal: 3T axial slice*

The standard Gaussian filtered unwrapped phase image (Fig. 10c) displayed pronounced artefact at the cortical surface. An artefact caused by the presence of a singularity in the wrapped phase data is apparent in the left anterior surface of the brain. There was also a noticeable remaining bias field artefact that could

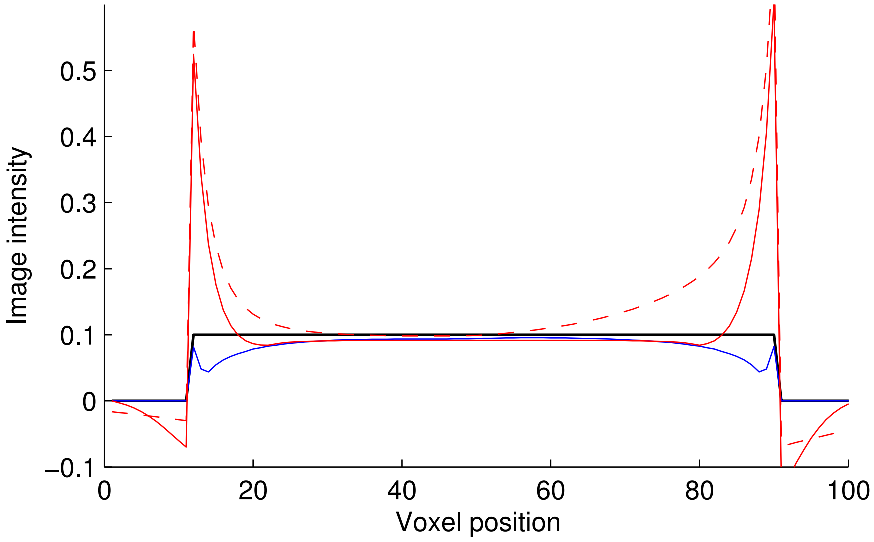

Figure 9: Line profile along central vertical line in simulated data. The black line indicates the ground truth. The blue line is the SDF result for $\sigma = 20$, as illustrated in Fig. 7i. Also shown are profiles for standard gaussian high pass filtering using $\sigma = 5$ (solid red line) and $\sigma = 20$ (dashed red line).

not be removed without compromising the contrast in the image. The complex filtered phase image (Fig. 10d) did not show evidence of the bias field artefact and the surface artefacts were reduced, including the singularity artefact. The hybrid method (Fig. 10e) was similarly successful at removing the large bias field. Spatially dependent filtering of the unwrapped phase image (Fig. 10f) produced the same results as the standard Gaussian filter method in the medial cortical ROI. The removal of surface artefacts was noticeably improved by the spatially dependent filter method. In particular, when applied to the complex filtered phase image (Fig. 10g), the method produced the lowest intensity spread ratio (Table 1), suggesting it is the most effective at removing surface artefact.

4.3.3 *Comparison of artefact removal: 7T superior axial slice*

The standard Gaussian filtering method applied to the unwrapped phase image (Fig. 11c) was successful at removing the bias field in the central region of the foreground, although artefacts remain at the cortical surface. Steep gradients in the phase data, such as at the anterior surface, could not be successfully removed using the complex filtering method without compromising the contrast within the medial region of the brain. The remaining surface artefact in the complex filtered phase image is more prominent than in the standard Gaussian filtered image, yet the intensity spread ratio score (Table 1) suggests otherwise. The hybrid method (Fig. 11e) produced an image with visibly reduced surface artefact compared with the previous methods. The spatially dependent filtering method applied to the

		Phase unwrapping + standard Gaussian filtering	Complex filtering	Hybrid method	Phase unwrapping + spatially dependent filtering	Complex filtered phase + spatially dependent filtering
3T axial slice	μ_m (σ_m)	-0.02 (0.15)	-0.02 (0.15)	-0.02 (0.14)	-0.02 (0.15)	-0.04 (0.15)
	μ_l (σ_l)	-0.07 (0.50)	-0.06 (0.40)	-0.05 (0.37)	-0.03 (0.32)	-0.00 (0.18)
	$\Delta\mu$	0.05	0.04	0.04	0.01	0.04
	R_σ	3.28	2.64	2.61	2.13	1.18
7T superior axial slice	μ_m (σ_m)	-0.01 (0.25)	0.05 (0.25)	-0.02 (0.24)	-0.01 (0.25)	-0.02 (0.22)
	μ_l (σ_l)	-0.02 (0.89)	-0.48 (0.87)	-0.19 (0.67)	-0.05 (0.35)	-0.02 (0.50)
	$\Delta\mu$	0.01	0.53	0.17	0.04	0.01
	R_σ	3.62	3.45	2.81	1.42	2.29
7T inferior axial slice	μ_m (σ_m)	-0.02 (0.24)	-0.03 (0.19)	-0.03 (0.19)	-0.02 (0.24)	-0.03 (0.19)
	μ_l (σ_l)	0.08 (1.39)	0.09 (0.81)	0.01 (1.24)	-0.00 (0.46)	-0.01 (0.49)
	$\Delta\mu$	0.10	0.12	0.04	0.02	0.02
	R_σ	5.76	4.25	6.70	1.90	2.55

Table 1: Medial and lateral cortical ROI phase intensity distributions and artefact removal measures for the local field phase images.

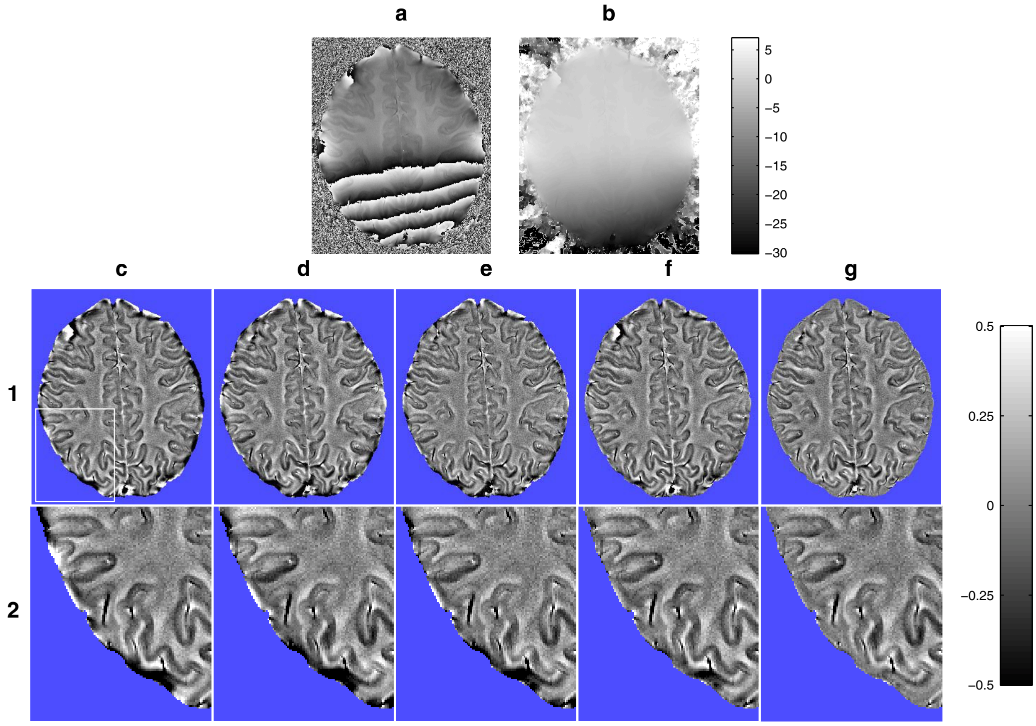

Figure 10: 3T axial slice phase data (rads) in (a) wrapped and (b) unwrapped stages. Phase images constructed using (c) standard Gaussian filtering of the unwrapped phase image, (d) complex filtering, (e) the hybrid method, and spatially dependent filtering applied to the (f) unwrapped phase data and the (g) complex filtered phase image. Row 2 shows magnifications of the region indicated in image (c1).

unwrapped phase image (Fig. 11f) and complex filtered phase image (Fig. 11g) demonstrated improvement in reduction of the surface artefact compared to the standard Gaussian filtering, complex filtering and the hybrid methods. Fine structural detail at the cortical surface, such as venous vessels, were visible in the spatially dependent filtering images which remain obscured in the other images. The reduction in shift in mean and intensity spread ratio scores for the spatially dependent filtering images compared to the other three methods support the visually identified results (Table 1).

4.3.4 *Comparison of artefact removal: 7T inferior axial slice*

The standard Gaussian filtered phase image (Fig. 12c) demonstrated substantial contrast within the medial cortical areas although there were noticeable surface artefacts. The complex filtering method (Fig. 12d) improved on the artefact removal, but lacked the contrast visible in the standard Gaussian filtered image. The hybrid method (Fig. 12e) produced similar internal contrast; however, while the removal of surface artefact visually appears comparable to the complex filtering method, the intensity spread ratio score (Table 1) is significantly worse, as a result

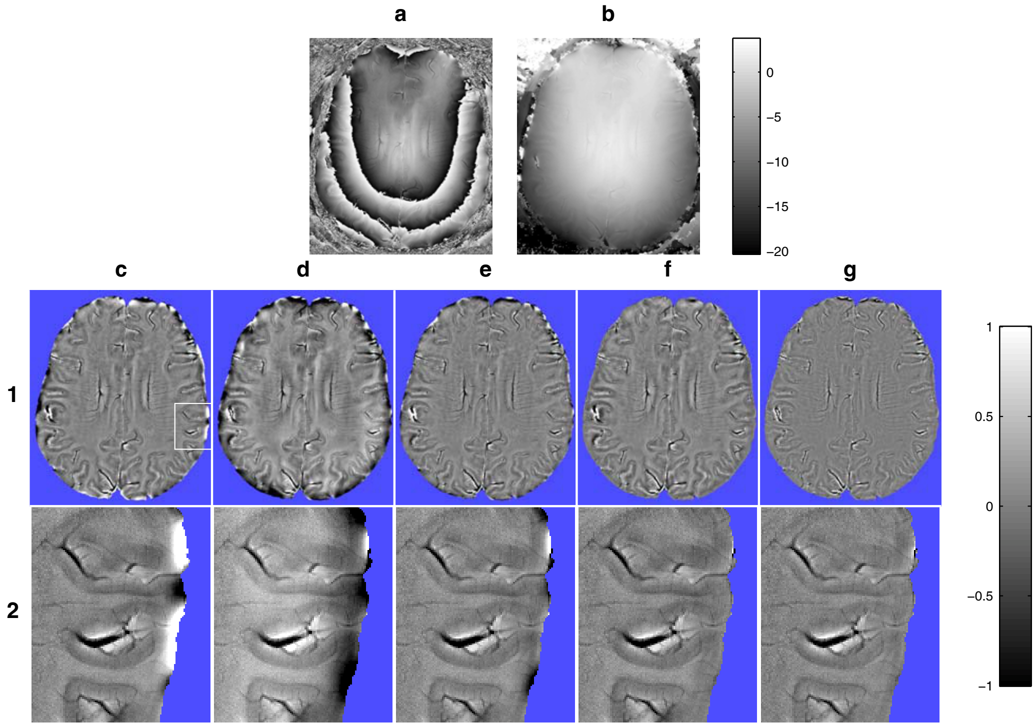

Figure 11: 7T superior axial slice phase data (rads) in (a) wrapped and (b) unwrapped stages. Phase images constructed using the (c) standard Gaussian filtering of the unwrapped phase image, (d) complex filtering, (e) the hybrid method, and spatially dependent filtering applied to the (f) unwrapped phase data, and (g) complex filtered phase image. Row 2 presents magnification of the region indicated in image (c1).

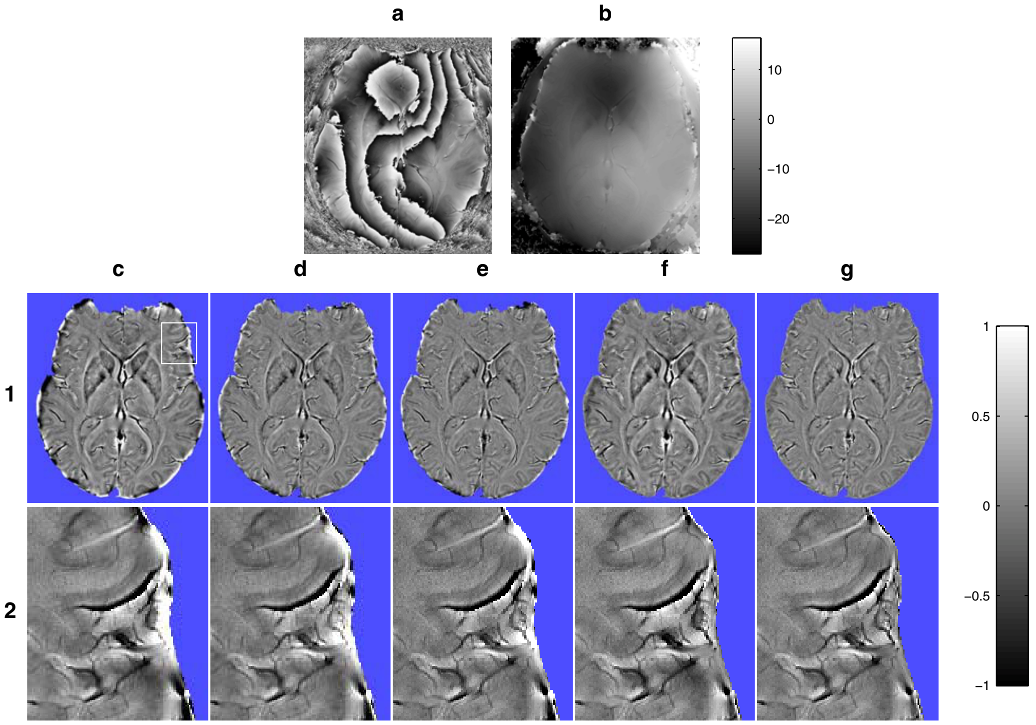

Figure 12: 7T inferior axial slice phase data (rads) in (a) wrapped and (b) unwrapped stages. Phase images constructed using (c) standard Gaussian filtering of the unwrapped phase, (d) complex filtering, (e) the hybrid method, spatially dependent filtering of the (f) unwrapped phase data, and (g) complex filtered phase image. Row 2 presents magnification of the region indicated in image (c1).

of the remaining artefacts in the anterior surface of the brain. Spatially dependent filtering of the unwrapped phase image (Fig. 12f) maintained the contrast in the central region apparent in the standard Gaussian filtered image, while the reduction of surface artefacts was improved. Intricate structural detail was revealed in areas populated in other images by high intensity artefacts. Spatially dependent filtering also improved on the complex filtered phase image (Fig. 12g).

4.3.5 *Computation time*

Computational efficiency was below one minute for all methods (Table 2). Processing times for the 7T images were considerably slower than the 3T images. Complex filtering proved to be the fastest of all methods with <1 second computation times. For the methods requiring phase unwrapping, the unwrapping stage was the most time consuming. The hybrid method and spatially dependent filtering of the unwrapped phase image had comparable times. In comparison to these two methods, the spatially dependent filtering method of the complex filtered phase image had similar computational efficiency for the 3T data and was substantially faster for the 7T.

	3T axial slice	7T superior axial slice	7T inferior axial slice
Phase unwrapping + standard Gaussian filtering	(3.30 s + 0.0138 s) = 3.31 s	(30.9 s + 0.0602 s) = 30.9 s	(34.5 s + 0.0756 s) = 34.5 s
Complex filtering	0.101 s	0.618 s	0.561 s
Hybrid method	(3.30 s + 2.88 s) = 6.17 s	(30.9 s + 16.2 s) = 47.0 s	(34.5 s + 21.6 s) = 56.1 s
Phase unwrapping + spatially dependent filtering	(3.30 s + 2.26 s) = 5.55 s	(30.9 s + 16.9 s) = 47.7 s	(34.5 s + 17.3 s) = 51.8 s
Complex filtered phase + spatially dependent filtering	(0.101 s + 5.28 s) = 5.38 s	(0.618 s + 13.7 s) = 14.3 s	(0.561 s + 20.0 s) = 20.5 s

Table 2: Total computation time for producing each image slice.

4.4 DISCUSSION

Spatially dependent filtering is a post-processing procedure that can be applied to both unwrapped phase images and complex filtered phase images. Like other adaptive filtering techniques, it exploits spatial variations in structural features of the data to optimise the filtering parameters for localised requirements. Adaptive methods have been used in MRI for various applications such as providing localised noise estimation in magnitude images [29], preserving edges during denoising [30] and aiding in image segmentation [31]. The computational cost of adaptive methods is well noted and techniques have been proposed that address this issue by optimising both hardware configuration [32] and algorithm design [29]. The spatially dependent filtering method proposed here capitalises on prior knowledge of differences between brain and non-brain voxels to improve removal of surface artefact, and on the symmetry of the Gaussian filter to avoid lengthy iterations and optimise computational efficiency.

The spatially dependent filtering method, employing higher frequency filtering near the surface and lower frequency filtering towards the centre of the brain, is a compromise between maintaining fine structural detail and estimating the bias field and surface artefacts. The effectiveness of the spatially dependent filtering method was demonstrated in the simulation dataset. The differences between ground truth and the estimated local phase image are present at the surface of the brain, where changes due to structural detail are not explicitly distinguished from surface artefact. However, the results on the 3T and 7T datasets demonstrate that more structural detail is preserved by spatially dependent filtering compared to the standard Gaussian filtering of unwrapped phase, complex filtering and the hybrid method.

Applied to unwrapped phase images, spatially dependent filtering has identical performance to the standard Gaussian filtering method in the medial cortical region of the brain due to equivalent filter parameters being applied in this region. The results of the two filtering methods differ in voxels close to the brain/non-brain surface. While the standard filtering method filters both brain and non-brain voxels without altering the filter size, the spatially dependent filtering method filters using only brain voxels, and decreases the filter size to compensate for the reduced neighbourhood of voxels that have similar signal intensities and noise levels. As a result, spatially dependent filtering demonstrates substantial image improvement with removal of surface artefacts compared to the standard Gaussian filtered image without compromising on the filtering performance elsewhere within the image.

Complex filtering introduces less surface artefact than the standard Gaussian filtering of unwrapped phase images, but this can be at the cost of contrast within the medial region of the brain (see Section 3.3). The spatially dependent filtering method efficiently removes the remaining surface artefacts, with only minor loss of contrast elsewhere in the image. Compared to spatially dependent filtering of the unwrapped phase image, spatially dependent filtering of the complex filtered phase image is generally more effective at producing images with minimal artefact near the brain/non-brain surface, while spatially dependent filtering of the unwrapped phase image maintains greater contrast within the medial cortical areas of the brain.

The hybrid method produces images with fewer surface artefacts compared to standard Gaussian filtering of unwrapped phase images and the complex filtering method. As with the phase unwrapping and complex filtering methods, the success of the hybrid method is dependent on the properties of the original phase data. Unlike the complex filtering method it does not suffer from residual phase wraps in the final image. However, as with all methods reliant on phase unwrapping, it is still subject to singularity problems. Nevertheless, spatially dependent filtering demonstrates greater efficacy in removing surface artefact compared to the hybrid method, as well as comparable or improved retention of contrast in the medial cortical areas of the brain.

The shift in mean and intensity spread ratio metrics provide a measurement of the surface artefact in the images. While the trends in the measures mostly reflect the visual assessments of the three images, the metrics are not infallible. In comparing the hybrid method phase image to the complex filtered phase image for the 7T slices, the discrepancy between the metric scores and the visually assessed improvement demonstrates the metrics' sensitivity to small, but not insignificant, areas with steep intensity gradients. In these sections, the complex filtering method retains the phase wraps, limiting the data range to $[-\pi, \pi)$, while the phase unwrapping steps in the hybrid method allow the data to extend beyond this range.

The demonstrated ability of the spatially dependent filtering method to remove surface artefact and reveal underlying structural detail has direct benefit for applications such as venography and cortical grey matter segmentation. In the lateral cortical regions of the brain, venous vessels are now visible allowing for improved reliability of venography in these areas. The improved grey matter definition also allows for greater accuracy in analysis and segmentation of cortical surfaces and cortical folding. Since the effect on contrast in the medial subcortical regions of the brain is negligible, there is only benefit to gain in using spatially dependent filtering in place of the traditional methods of phase processing.

The computation was acceptably fast for all methods. The computational efficiency of phase unwrapping is greatly influenced by the choice and implementation of algorithm, image size and number of residues and phase wraps, but it is uniformly slow in comparison to the complex filtering method which does not require phase unwrapping. Following the initial processing of the phase data, the efficiency of the spatially dependent filtering method is predominantly influenced by the number of unique values in $\boldsymbol{\alpha}$, which determines the number of iterations of (4.13). Rounding of the Gaussian filtered binary mask (4.8) ensures that the maximum number of iterations is 101. The efficiency of this algorithm is further enhanced by the implementation of the brain voxel constraint in a single equation (4.13) without the need to iterate through each voxel to determine the neighbouring brain voxels. Compared to the hybrid method, the spatially dependent filtering method is marginally faster.

Spatially dependent filtering is a versatile method and can be easily applied to 3D datasets by using 3D filters. The principles behind the method allow for the use of other symmetrical averaging filter kernels, such as mean filters and Hamming windows. The exponentiation in (4.9) can be modified by altering the base and exponent to effect steeper or milder gradients in the α map. In applications where phase unwrapping is confined to specific regions of interest (ROI), spatially dependent filtering can be applied by using the binary mask defining the ROI in place of the brain/non-brain mask.

4.5 CONCLUSION

The accuracy of information in local field phase images is crucial not only for interpreting the images, but also for processing methods that rely on the phase information, such as SWI and susceptibility maps. Spatially dependent filtering is shown to be an effective method of removing artefact at the cortical surface. The method is computationally efficient and versatile enough to be used with different symmetrical averaging filter kernels and in region specific phase unwrapping applications. It has been shown to produce more reliable phase information than standard Gaussian filtering of unwrapped phase images, complex filtering and the hybrid method, and reveals underlying structure and detail that remain obscured by other methods.

BIBLIOGRAPHY

[1] E. Mark Haacke, Yingbiao Xu, Yu-Chung N. Cheng, and Jürgen R. Reichenbach. Susceptibility weighted imaging (SWI). *Magnetic Resonance in Medicine*, 52(3):612–618, 2004.

[2] JR Reichenbach, R Venkatesan, DJ Schillinger, DK Kido, and EM Haacke. Small vessels in the human brain: MR venography with deoxyhemoglobin as an intrinsic contrast agent. *Radiology*, 204(1):272–277, July 1997.

[3] Lin Li and Zhiyue J. Wang. Magnetic susceptibility quantitation with MRI by solving boundary value problems. *Medical Physics*, 30(3):449–453, March 2003.

[4] Tian Liu, Pascal Spincemaille, Ludovic de Rochefort, Bryan Kressler, and Yi Wang. Calculation of susceptibility through multiple orientation sampling (COSMOS): a method for conditioning the inverse problem from measured magnetic field map to susceptibility source image in MRI. *Magnetic Resonance in Medicine*, 61(1):196–204, January 2009.

[5] Karin Shmueli, Jacco A. de Zwart, Peter van Gelderen, Tie-Qiang Li, Stephen J. Dodd, and Jeff H. Duyn. Magnetic susceptibility mapping of brain tissue in vivo using MRI phase data. *Magnetic Resonance in Medicine*, 62(6):1510–1522, December 2009.

[6] D.C. Noll, D.G. Nishimura, and A. Macovski. Homodyne detection in magnetic resonance imaging. *Medical Imaging, IEEE Transactions on*, 10(2):154–163, 1991.

[7] Alexander Rauscher, Jan Sedlacik, Markus Barth, Hans-Joachim Mentzel, and Jurgen R. Reichenbach. Magnetic susceptibility-weighted MR phase imaging of the human brain. *AJNR Am J Neuroradiol*, 26(4):736–742, April 2005.

[8] Hassan Bagher-Ebadian, Quan Jiang, and James R. Ewing. A modified fourier-based phase unwrapping algorithm with an application to MRI venography. *Journal of Magnetic Resonance Imaging*, 27(3):649–652, 2008.

[9] S. Chavez, Qing-San Xiang, and L. An. Understanding phase maps in MRI: a new cutline phase unwrapping method. *Medical Imaging, IEEE Transactions on*, 21(8):966–977, 2002.

[10] Jason Langley and Qun Zhao. Unwrapping magnetic resonance phase maps with chebyshev polynomials. *Magnetic Resonance Imaging*, 27(9):1293–1301, November 2009.

[11] A. Vidal-Pantaleoni, R. Oviol, and M. Ferrando. A comparison of phase unwrapping techniques in synthetic aperture radar interferometry. In *Proceedings of the International Geoscience and Remote Sensing Symposium*, pages 1354–1356, Hamburg, Germany, 1999.

[12] R. Yamaki and A. Hirose. Singularity-spreading phase unwrapping. *Geoscience and Remote Sensing, IEEE Transactions on*, 45(10):3240–3251, 2007.

[13] Anand Asundi and Zhou Wensen. Fast phase-unwrapping algorithm based on a gray-scale mask and flood fill. *Applied Optics*, 37(23):5416–5420, 1998.

[14] Marvin A. Schofield and Yimei Zhu. Fast phase unwrapping algorithm for interferometric applications. *Optics Letters*, 28(14):1194–1196, July 2003.

[15] Jeff H. Duyn, Peter van Gelderen, Tie-Qiang Li, Jacco A. de Zwart, Alan P. Koretsky, and Masaki Fukunaga. High-field MRI of brain cortical substructure based on signal phase. *Proceedings of the National Academy of Sciences*, 104(28):11796–11801, July 2007.

[16] Christian Langkammer, Ferdinand Schweser, Nikolaus Krebs, Andreas Deistung, Walter Goessler, Eva Scheurer, Karsten Sommer, Gernot Reishofer, Kathrin Yen, Franz Fazekas, Stefan Ropele, and Jürgen R. Reichenbach. Quantitative susceptibility mapping (QSM) as a means to measure brain iron? a post mortem validation study. *NeuroImage*, 62(3):1593–1599, September 2012.

[17] Tian Liu, Ildar Khalidov, Ludovic de Rochefort, Pascal Spincemaille, Jing Liu, and Yi Wang. Improved background field correction using effective dipole fitting. In *Proceedings of the ISMRM/ESMRMB Joint Annual Meeting*, Stockholm, Sweden, May 2010.

[18] Samuel James Wharton and Richard W. Bowtell. Dipole-based filtering for improved removal of background field effects from 3D phase data. In *Proceedings of the ISMRM/ESMRMB Joint Annual Meeting*, Stockholm, Sweden, May 2010.

[19] Tian Liu, Jing Liu, Ludovic de Rochefort, Pascal Spincemaille, Ildar Khalidov, James Robert Ledoux, and Yi Wang. Morphology enabled dipole inversion (MEDI) from a single-angle acquisition: Comparison with COSMOS in human brain imaging. *Magnetic Resonance in Medicine*, 66(3):777–783, 2011.

[20] Tian Liu, Krishna Surapaneni, Min Lou, Liuquan Cheng, Pascal Spincemaille, and Yi Wang. Cerebral microbleeds: burden assessment by using quantitative susceptibility mapping. *Radiology*, 262(1):269–278, January 2012.

[21] Y. Wang, Y. Yu, D. Li, K.T. Bae, J.J. Brown, W. Lin, and E.M. Haacke. Artery and vein separation using susceptibility-dependent phase in contrast-enhanced MRA. *Journal of Magnetic Resonance Imaging*, 12(5):661–670, 2000.

[22] Zhaoyang Jin, Ling Xia, and Yiping P Du. Reduction of artifacts in susceptibility-weighted MR venography of the brain. *Journal of Magnetic Resonance Imaging: JMRI*, 28(2):327–33, August 2008.

[23] Jaladhar Neelavalli, Yu-Chung N. Cheng, Jing Jiang, and E. Mark Haacke. Removing background phase variations in susceptibility-weighted imaging using a fast, forward-field calculation. *Journal of Magnetic Resonance Imaging*, 29(4):937–948, April 2009.

[24] Alexander Rauscher, Markus Barth, Karl-Heinz Herrmann, Stephan Witoszynskyj, Andreas Deistung, and J³ergen R. Reichenbach. Improved elimination of phase effects from background field inhomogeneities for susceptibility weighted imaging at high magnetic field strengths. *Magnetic Resonance Imaging*, 26(8):1145–1151, October 2008.

[25] T.F. Chan and L.A. Vese. Active contours without edges. *Image Processing, IEEE Transactions on*, 10(2):266–277, 2001.

[26] John David Jackson. In *Classical Electrodynamics 3rd Ed*, pages 184–188. John Wiley & Sons, Inc, New York, 1998.

[27] Zhaolin Chen, Leigh A. Johnston, Dae Hyuk Kwon, Se Hong Oh, Zang-Hee Cho, and Gary F. Egan. An optimised framework for reconstructing and processing MR phase images. *NeuroImage*, 49(2):1289–1300, January 2010.

[28] Stephan Witoszynskyj, Alexander Rauscher, Jürgen R. Reichenbach, and Markus Barth. Phase unwrapping of MR images using [Phi]UN - a fast and robust region growing algorithm. *Medical Image Analysis*, 13(2):257–268, April 2009.

[29] P. Coupe, P. Yger, S. Prima, P. Hellier, C. Kervrann, and C. Barillot. An optimized blockwise nonlocal means denoising filter for 3-d magnetic resonance images. *Medical Imaging, IEEE Transactions on*, 27(4):425–441, 2008.

[30] G. Z. Yang, P. Burger, D. N. Firmin, and S. R. Underwood. Structure adaptive anisotropic image filtering. *Image and Vision Computing*, 14(2):135–145, March 1996.

[31] W.M. Wells, W.E.L. Grimson, R. Kikinis, and F.A. Jolesz. Adaptive segmentation of MRI data. *Medical Imaging, IEEE Transactions on*, 15(4):429–442, 1996.

[32] N. Srivastava, J.L. Trahan, R. Vaidyanathan, and S. Rai. Adaptive image filtering using run-time reconfiguration. In *Proceedings of the International Parallel and Distributed Processing Symposium*, Nice, France, 2003.

5

SIGMOID-SWI

A CORRECTION METHOD FOR VENOUS VESSEL BOUNDARY DELINEATION AT HIGH FIELD

Negative phase mask SWI [1, 2] is a popular MR imaging method for venography. The magnetic susceptibility of venous blood and partial volume effects lead to negative phase values that are exploited by SWI. At higher field strengths, the effects of localised magnetic susceptibility differences are amplified, leading to increased phase contrast and larger susceptibility artefacts [3, 4]. For larger veins that are oriented perpendicular to the direction of the main field, the susceptibility difference between the vein and surrounding tissue causes dipolar changes in the magnetic field immediately outside the vein. The field changes result in increased phase in the plane perpendicular to the main field, decreased phase in the direction parallel to the main field and magnitude attenuation. In SWI, this can affect the visibility of the large vein boundaries, resulting in incorrect vessel segmentation, as will be demonstrated. This chapter presents Sigmoid-SWI, a modification to the SWI phase mask that corrects the vessel boundaries by using the increased phase outside the vessel to amplify the attenuated magnitude.

5.1 THEORY

Venous vessels can be modelled as long cylinders whose effects on the surrounding magnetic field is described by [5]

$$\Delta B\left(r,\theta\right)=\frac{\Delta\chi}{2}\sin^{2}\left(\beta\right)\left(\frac{a}{r}\right)^{2}\cos\left(2\theta\right)B_{0}, \tag{5.1}$$

where $\Delta\chi$ is the difference in susceptibility between the cylinder and the surrounding tissues, β is the angle between the cylinder and the direction of the main B field, a is the radius of the cylinder and B_0 is the strength of the main B field (Fig. 13a). r and θ are coordinates of a point $\mathbf{r}$ in the plane normal to the cylinder axis, where r is the distance from the cylinder axis to $\mathbf{r}$ and θ is the angle between the direction of the main B field and $\mathbf{r}$ (Fig. 13b). In axial slices, where the vein is perpendicular to the main B field, $\theta = \frac{\pi}{2}$ and $\beta = \frac{\pi}{2}$, the magnitude of ΔB is greatest and ΔB opposes the direction of the main B field.

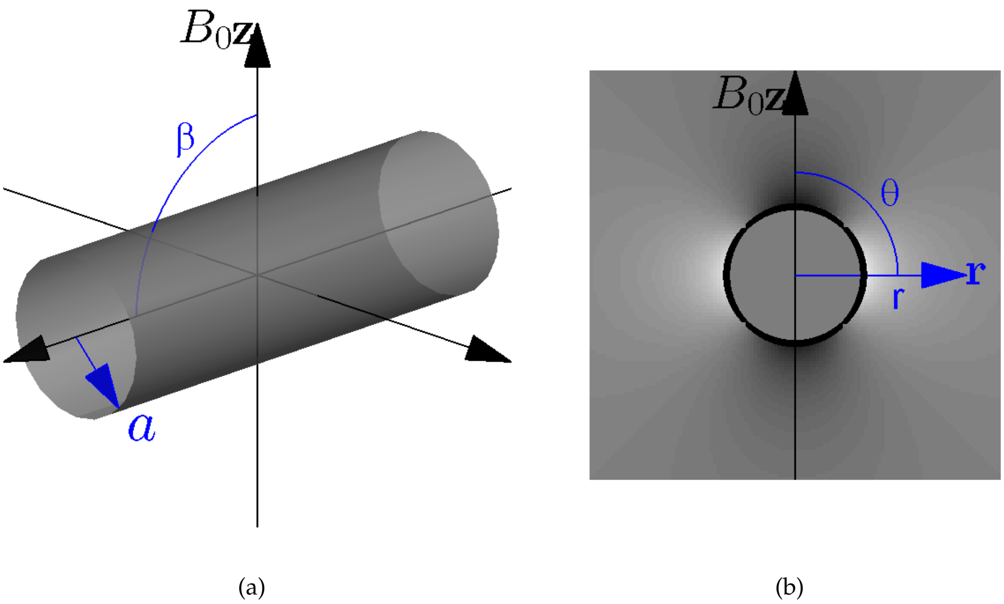

(a)

(b)

Figure 13: Parameter definitions for deriving the change in B field outside (a) a cylinder perpendicular to the main field and (b) the change in phase produced by this cylinder.

The phase,

$$\phi = -\gamma \Delta B.\mathrm{TE}, \tag{5.2}$$

where $\gamma = 2.67513 \times 10^8$ rad.s^{-1}T^{-1} is the gyromagnetic ratio of the ^{1}H proton and TE is the echo time, implies that, in an axial slice, voxels surrounding veins perpendicular to the Bo field will have positive phase. The product $\gamma \Delta B$ describes the shift in Larmor frequency resulting from the cylinder. At $B_0 = 7$ T, typical acquisition bandwidth per voxel is 30 Hz, corresponding to $\Delta B \approx 0.7 \times 10^{-6}$ T. The susceptibility of deoxygenated blood in venous vessels is $\Delta\chi \approx 1.6$ ppm [6]. The largest field shifts occur in the voxels adjacent to the vein, that is, $r_A = a + w$, where w is the width of a voxel. Substitution of these values into (5.1) results in $\frac{a}{a+w} = 0.37$. The minimum vein radius required to produce a frequency shift large enough to cause a one voxel spatial shift of protons at position $\left(r_A, \frac{\pi}{2}\right)$, and therefore substantially affect the magnitude intensity, is $R_{min} = \frac{a}{w} = 0.58$, where R_{min} is a fraction of the voxel width.

SWI is calculated voxel-wise from the magnitude and phase data as

$$S(\mathbf{v}) = \rho(\mathbf{v}) F(\mathbf{v})^n \tag{5.3}$$

where $S(\mathbf{v})$ is the intensity in the SWI image of voxel $\mathbf{v}$, $\rho(\mathbf{v})$ is the magnitude of the voxel, n is an exponent, typically chosen as $n = 4$ [1], and $F(\mathbf{v})$ is the phase mask. The positive phase mask is defined as

$$F_{+}(\mathbf{v}) = \begin{cases} 1, & \phi(\mathbf{v}) < 0 \\ \frac{\pi - \phi(\mathbf{v})}{\pi}, & \phi(\mathbf{v}) \geq 0 \end{cases} \tag{5.4}$$

and the negative phase mask is defined as

$$F_{-}(\mathbf{v}) = \begin{cases} \frac{\pi + \phi(\mathbf{v})}{\pi}, & \phi(\mathbf{v}) \leq 0 \\ 1, & \phi(\mathbf{v}) > 0 \end{cases} \tag{5.5}$$

where $\phi(\mathbf{v})$ is the phase intensity of the voxel. A negative shift will occur in the phase of voxels containing veins provided the spatial resolution in the direction of the main B field is lower than the resolutions in the transverse plane [7]. Although the shift may be visually imperceptible in the phase image, the SWI method is successful at increasing the visibility of veins of subvoxel diameter. However, the attenuation in the magnitude image due to veins parallel to the main B field and having radius larger than R_{min} is not addressed by SWI. This signal loss in voxels surrounding the veins results in blurred vessel edges and a widened appearance of veins. Without correction of the attenuation, overestimation of vessel width will occur.

5.2 METHOD

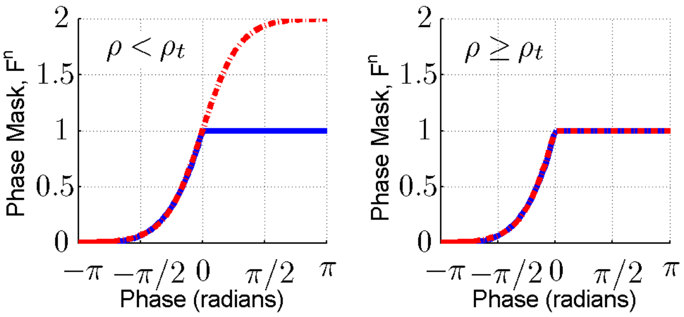

Figure 14: Comparison of (blue) SWI phase mask, F_{-}^{4}, and (red) sigmoid-SWI phase mask, F_S.

Our proposed modified phase mask, $F_S(\mathbf{v})$, compensates for the attenuation of the magnitude surrounding large veins while maintaining the general contrast of conventional SWI. This is achieved by applying a sigmoid filter to voxels whose phase is less than zero and/or whose magnitude is less than the local gaussian average of non-brain voxels:

$$F_S(\mathbf{v}) = \begin{cases} \frac{2}{1+e^{-k\phi(\mathbf{v})}} & , \phi(\mathbf{v}) \leq 0 \text{ or } \rho(\mathbf{v}) < \rho_t(\mathbf{v}) \\ 1 & , \text{otherwise} \end{cases} \tag{5.6}$$

where $k = 2.15$ is a constant chosen such that F_S simulates F_-^4 when $\phi(\mathbf{v}) \leq 0$ (Fig. 14). $\rho_t(\mathbf{v})$ is the local average intensity of brain voxels in the magnitude data, calculated as

$$\rho_t(\mathbf{v}) = \left(\frac{(\boldsymbol{\rho} \cdot \mathbf{M}) * \mathbf{G}}{\mathbf{M} * \mathbf{G}}\right)_{\mathbf{v}} \tag{5.7}$$

where $\boldsymbol{\rho}$ is the magnitude map, $\mathbf{M}$ is a brain/non-brain mask where the value 0 indicates non-brain and 1 indicates brain, $\mathbf{G}$ is a Gaussian window kernel, $\cdot$ indicates voxel-wise multiplication and $*$ indicates the convolution operation. The modified phase mask has a similar attenuation profile to the F_-^4 when phase is negative, but demonstrates amplification properties when phase is positive and the magnitude is below ρ_t (Fig. 14).

5.2.1 *Experimental data*

MRI data of a healthy male volunteer (age 27) was acquired on a 7T Siemens system with an 8 channel transmit-receive head coil (Neuroscience Research Institute, Incheon, South Korea). Axial T2*-weighted gradient echo (GRE) images were acquired with TE = 21.6 ms, TR = 750 ms, FA = 30°, bandwidth = 30 Hz per pixel, slice thickness = 2mm, FOV = 256 × 224 mm^2 , matrix size = 1024 × 896, spatial resolution was 0.25 × 0.25 × 2 mm^3, a total of 17 slices and total scan time of 11.5 min. Magnitude and wrapped phase data were reconstructed using the optimised complex reconstruction method [8]. Phase was unwrapped using PhUN [9] and background field removed using a spatially dependent filtering method (Chapter 4 and [10]). The Gaussian window kernel in (5.7) was set to 50 voxels wide with a standard deviation of 10 voxels. The brain/non-brain mask was calculated using active-snake contours [11].

Line profiles from the magnitude, phase, SWI, and sigmoid-SWI image were taken from three regions of interest (ROI) containing vessels oriented perpendicular to the main field. True vessel boundaries were localised at the transitions between positive and negative phase. In the SWI and sigmoid-SWI image, the intensity mean along the line profiles was calculated, excluding voxels designated as vessels in the phase profile. The apparent vessel boundaries in the SWI and sigmoid-SWI were then localised at the transitions below and above their respective means.

5.3 RESULTS AND DISCUSSION

The effects of the high field strength on magnitude and phase intensity surrounding large veins is visible in the acquired data (Fig 15a and 15b). The magnitude image demonstrates attenuation in voxels immediately surrounding large veins that are oriented perpendicular to the main magnetic field, while the phase image demonstrates higher phase values surrounding these veins, as seen in the line profiles in Fig. 16.

The true vessel width, as derived from the phase, is 3 voxels for the yellow ROI and 4 voxels for the blue ROI (red vertical lines, Fig. 16). The estimation of the vessel width assumes that phase values within the voxel will be negative and im-

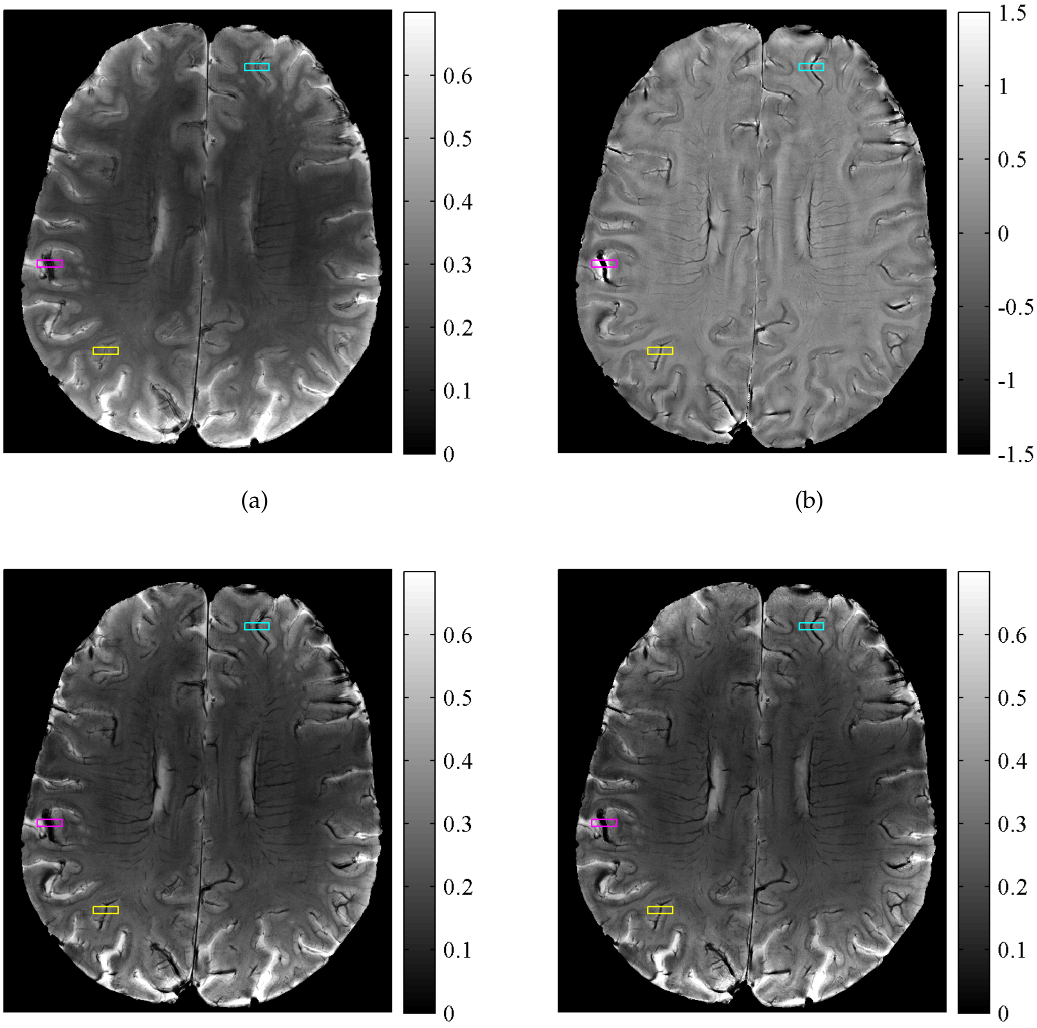

(a) (b)

(c) (d)

Figure 15: (a) Magnitude, (b) phase (in rads), (c) SWI and (d) sigmoid-SWI. ROIs are outlined in yellow, blue and pink. The main magnetic field is directed out of the page.

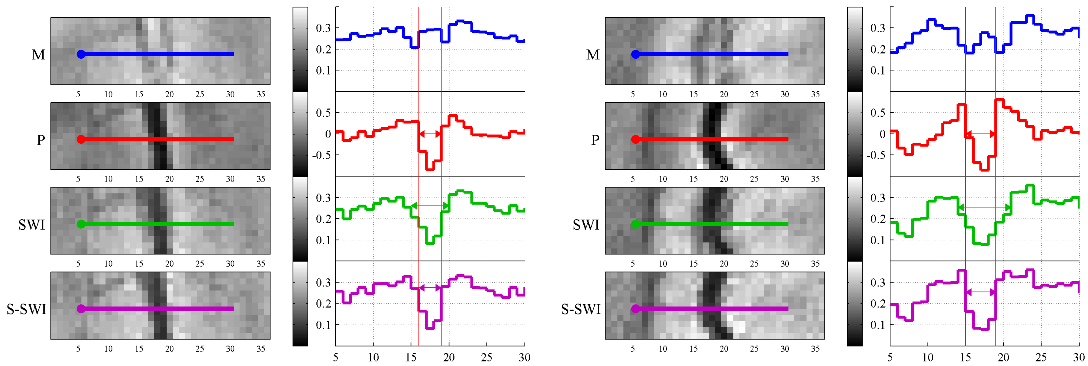

(a) (b)

Figure 16: Line profile comparisons for the (a) yellow ROI and (b) blue ROI outlined in Fig. 15. Line profiles are shown for (M) magnitude, (P) phase, SWI, and (S-SWI) sigmoid-SWI. Red vertical lines indicate the true boundary of the vessel, as delineated by phase information. Arrows in the line profiles indicate vessel width, derived as positions where the intensity crosses zero in the phase image and the mean intensity outside the vein in the SWI and sigmoid-SWI, as indicated by the vertical positioning of the arrows.

mediately outside the voxel will be positive, a result of the susceptibility effects described by (5.1). The estimation does not take into account partial volume effects which are difficult to model, due to the quadratic nature of the change in B field, the non-linearity of phase averaging, the anisotropy of the voxel dimensions and the unknown positioning of the vessel with respects to the voxel limits. Nevertheless, it is reasonable to assume the vessel border will occur within the region comprising adjacent positive and negative phase voxels.

The SWI image (Fig 15c) demonstrates attenuated values immediately outside the veins. The line profiles (Fig. 16) demonstrate weaker vessel edges compared to the phase profile. Estimation of the boundary of the vessels from the SWI data is complicated by these gradients. Venography derived from SWI employ minimum intensity projection (mIP) techniques under the assumption that vein voxels have lower intensities than non-venous voxels. A similar assumption is made in this chapter for localising the boundary of the vessels: vein voxels are assumed to have an intensity below the mean of non-venous voxels. Using this assumption, vessel widths of 5 and 7 voxels are derived for the yellow and blue ROIs, respectively (Fig 16, green arrows), and are 2 and 3 voxels greater than the phase-derived vessel widths.

The sigmoid-SWI image (Fig 15d) is overall similar to the SWI. However, on closer examination, the sigmoid-SWI produces more accurate vessel delineation, as follows. The sigmoid-SWI line profiles (Fig. 16) have steeper gradients than the SWI profiles and corrected vessel widths are 3 and 4 voxels for the yellow and

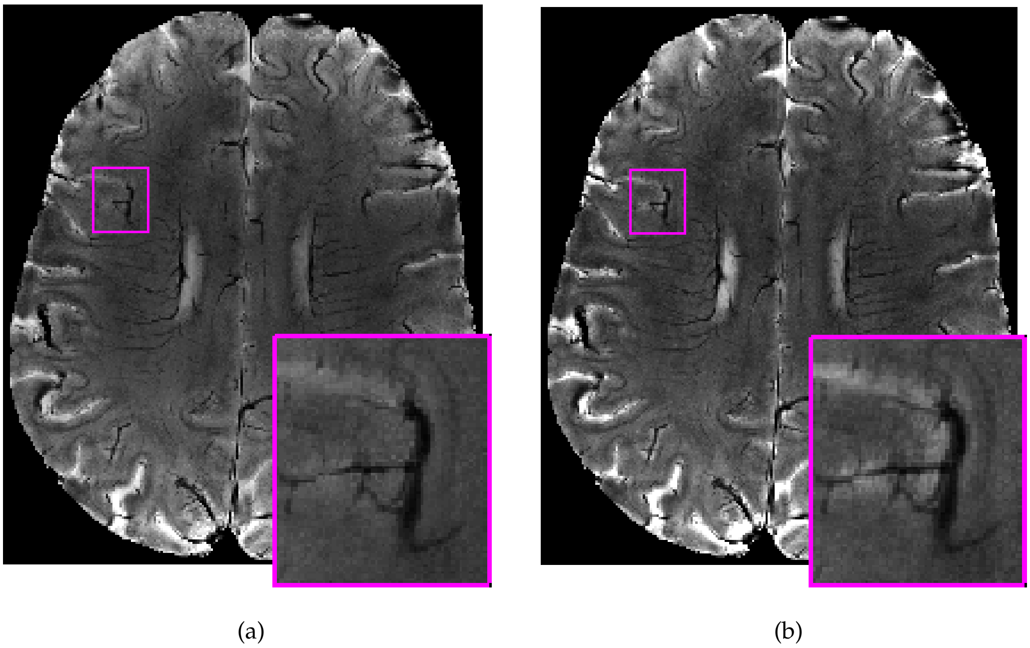
(a) (b)

Figure 17: Comparison of (a) sigmoid-SWI using threshold, ρ_t, and (b) sigmoid-SWI with no thresholding (i.e. $\rho_t = \infty$)

blue ROIs, respectively (Fig 16, purple arrows), in agreement with vessel widths derived from the phase.

The implementation of the local average threshold, ρ_t, ensures that the sigmoid-SWI image maintains the general contrast of SWI. Omitting the threshold and applying the sigmoid filter over all voxels results in intensity increases in voxels with positive phase (Fig 17). These high intensity areas suggest changes in the structure or composition of the tissue; however, they are a result of the dipolar nature of phase. Inclusion of the threshold avoids these misleading artefacts and ensures recognisable contrast akin to conventional SWI.

The effectiveness of sigmoid-SWI is limited in situations where the absolute change in B field is large enough that phase differences greater than π occur between adjacent voxels. An example of this is demonstrated in Fig. 18. In the raw phase data, these shifts wrap to produce a phase difference less than π (light blue arrows), thus obscuring the true location of the large phase difference. Determining the positioning of these shifts is one of the difficulties faced by phase unwrapping algorithms. Information can sometimes be gathered from the magnitude, where an assumption is made that the structures that have differing magnetic susceptibility properties also have different relaxation properties, and their boundaries can therefore be determined by changes in magnitude intensity. This assumption is normally valid in the case of veins bordering grey or white matter, as the T_2^* contrast has been demonstrated to increase with higher field strengths [4]. However, if the changes in the B field are large enough, the magnitude signal

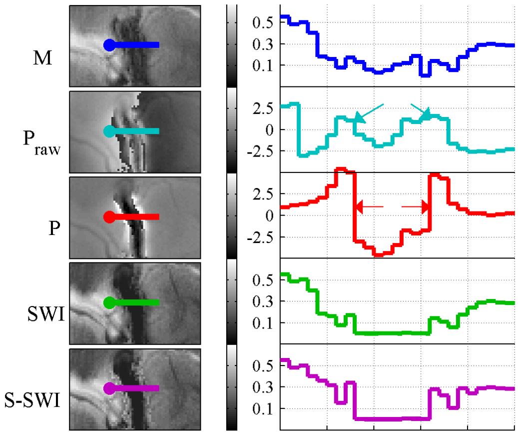

Figure 18: Line profiles for the pink ROI in Fig 15. The (M) magnitude image shows low signal and SNR in the vicinity of the large vein. The (P_{raw}) raw phase image is wrapped such that true phase gradients greater than π appear as small phase shifts (light blue arrows). The determination of the location of these gradients (red arrows) in the (P) unwrapped phase image dictates the vessel boundaries and directly affects the results in the (SWI) susceptibility-weighted image and the (S-SWI) sigmoid-SWI image.

and signal-to-noise ratio (SNR) can decrease to a level where structural information is indistinguishable from noise and the assumption is no longer valid, as is demonstrated in Fig. 18. In this example, the estimated location of the large phase gradients and thus the vessel width cannot be validated, given the low magnitude signal. The estimation results in zero intensity voxels in the SWI and sigmoid-SWI where the vessel is deemed to be located. Non-vessel voxels located near the vessel boundary are attenuated in the SWI image and demonstrate amplified intensity in the sigmoid-SWI image. Since the magnitude intensity and SNR of these voxels is very low, the sigmoid-SWI method has amplified the noise. Translation of the vessel boundaries from the unwrapped phase to the sigmoid-SWI image still occurs, and therefore the effectiveness of the sigmoid-SWI method in delineating the vessels in these situations relies on the accuracy of the phase unwrapping method used.

5.4 CONCLUSIONS AND FUTURE WORKS

The results in this chapter have demonstrated that while SWI clearly shows the location of veins, the vein boundaries are blurred in larger vessels due to the attenuation in the magnitude image. The proposed sigmoid-SWI technique successfully corrects the delineation of the veins, while preserving SWI values within the vessel.

BIBLIOGRAPHY

[1] E. Mark Haacke, Yingbiao Xu, Yu-Chung N. Cheng, and Jürgen R. Reichenbach. Susceptibility weighted imaging (SWI). *Magnetic Resonance in Medicine*, 52(3):612–618, 2004.

[2] JR Reichenbach, R Venkatesan, DJ Schillinger, DK Kido, and EM Haacke. Small vessels in the human brain: MR venography with deoxyhemoglobin as an intrinsic contrast agent. *Radiology*, 204(1):272–277, July 1997.

[3] Juliane Budde, G. Shajan, Jens Hoffmann, Kâmil Uğurbil, and Rolf Pohmann. Human imaging at 9.4 T using T_2*-, phase-, and susceptibility-weighted contrast. *Magnetic Resonance in Medicine*, 65(2):544–550, 2011.

[4] Peter Koopmans, Rashindra Manniesing, Wiro Niessen, Max Viergever, and Markus Barth. MR venography of the human brain using susceptibility weighted imaging at very high field strength. *Magnetic Resonance Materials in Physics, Biology and Medicine*, 21(1):149–158, 2008.

[5] E. Mark Haacke, Robert W. Brown, Michael R. Thompson, and Ramesh Venkatesan. *Magnetic resonance imaging: physical principles and sequence design*. John Wiley & Sons, Inc, New York, 1999.

[6] William M. Spees, Dmitriy A. Yablonskiy, Mark C. Oswood, and Joseph J.H. Ackerman. Water proton MR properties of human blood at 1.5 Tesla: Magnetic susceptibility, T1, T2, T_2*, and non-Lorentzian signal behavior. *Magnetic Resonance in Medicine*, 45(4):533–542, 2001.

[7] Andreas Deistung, Alexander Rauscher, Jan Sedlacik, Jörg Stadler, Stephan Witoszynskyj, and Jürgen R. Reichenbach. Susceptibility weighted imaging at ultra high magnetic field strengths: Theoretical considerations and experimental results. *Magnetic Resonance in Medicine*, 60(5):1155–1168, 2008.

[8] Zhaolin Chen, Leigh A. Johnston, Dae Hyuk Kwon, Se Hong Oh, Zang-Hee Cho, and Gary F. Egan. An optimised framework for reconstructing and processing MR phase images. *NeuroImage*, 49(2):1289–1300, January 2010.

[9] Stephan Witoszynskyj, Alexander Rauscher, Jürgen R. Reichenbach, and Markus Barth. Phase unwrapping of MR images using [Phi]UN - a fast and robust region growing algorithm. *Medical Image Analysis*, 13(2):257–268, April 2009.

[10] Amanda Ng, Leigh Johnston, Zhaolin Chen, Zang-Hee Cho, Jingxin Zhang, and Gary Egan. Spatially dependent filtering for removing phase distortions at the cortical surface. *Magnetic Resonance in Medicine*, 2011.

[11] T.F. Chan and L.A. Vese. Active contours without edges. *Image Processing, IEEE Transactions on*, 10(2):266–277, 2001.

6

OPTIMISED CONTRAST IMAGES

ENHANCED IMAGE CONTRAST FROM MRI MAGNITUDE AND PHASE DATA

While several studies have explained and quantified biophysical mechanisms of magnitude and phase image contrast [1, 2], the combination of the magnitude and phase information, forming a single image volume with increased contrast, has been largely the purview of Susceptibility Weighted Imaging (SWI) [3, 4, 5]. The popularity of SWI [6, 7, 8, 9, 10, 11] and its inclusion in clinical studies is due to its simplicity, and its ability to enhance vasculature while not losing magnitude contrast. Variations on SWI have been proposed in the literature, such as the method proposed by Abduljalil et al[12] that utilises both negative and positive phase intensities in mask creation. The underlying fact remains, however, that SWI and its variants are heuristic schemes, rather than algorithms that are the result of a mathematically constructed optimisation able to guarantee desired image properties.

This chapter presents the Optimised Contrast Image (OCI) method, which produces an image volume with optimised tissue contrast, based on the distribution of voxel intensities in the magnitude-phase domain. The OCI method is based on a Gaussian mixture model classification of tissue classes, which weights the projection of magnitude-phase intensity vectors onto an optimised image projection axis. A tuning parameter in the OCI method enables a variety of contrast to be produced, from images with intra-class contrast emphasised, to those with enhanced inter-class contrast. The OCI method is compared to positive and negative mask SWI and an adaptation of Abduljalil's method, in application to 3T and 7T cortical sections. The results presented demonstrate the flexibility of OCI in producing improved contrast and preservation of structural detail from the magnitude and phase images.

6.1 THEORY

6.1.1 *The projection framework for magnitude-phase combination*

Prior to presenting details of the Optimised Contrast Image method, we define a projection framework that formalises notions of image formation from two-dimensional data, and which will assist comparison between methods.

Let ρ denote magnitude, ϕ denote phase, and $\boldsymbol{v} = \left[\begin{smallmatrix}\rho \\ \phi\end{smallmatrix}\right]$ the two-dimensional intensity vector. A projection maps $\boldsymbol{v}$ onto a given axis; the magnitude image is a projection of $\boldsymbol{v}$ onto the magnitude axis, and similarly the phase image is the projection of $\boldsymbol{v}$ onto the phase axis. The projection axis need not be restricted to either the magnitude or phase axis however, but can be a line in any direction. Let the unit vector $\hat{\boldsymbol{u}}$ denote the projection axis that makes an angle $\theta_{\hat{\boldsymbol{u}}}$ with the magnitude axis,

$$\hat{\boldsymbol{u}} = \begin{bmatrix} \cos\theta_{\hat{\boldsymbol{u}}} \\ \sin\theta_{\hat{\boldsymbol{u}}} \end{bmatrix}.$$

Projection of a two-dimensional data vector, $\boldsymbol{v}$, onto axis $\hat{\boldsymbol{u}}$ results in projected image intensity $\boldsymbol{v} \cdot \hat{\boldsymbol{u}}$, where $\cdot$ denotes the dot product of two vectors.

The reduction of magnitude and phase data to a single image intensity dimension can be more than a straight-forward projection. A transformation, T, may remap vectors $\boldsymbol{v}$ prior to projection,

$$T\left(\begin{bmatrix} \rho \\ \phi \end{bmatrix}\right) = \begin{bmatrix} \rho' \\ \phi' \end{bmatrix}.$$

Let $s : \mathbf{R}^2 \to \mathbf{R}$ denote the complete mapping associated with transformation and projection (see Fig. 19),

$$s(\boldsymbol{v}; T, \hat{\boldsymbol{u}}) = T(\boldsymbol{v}) \cdot \hat{\boldsymbol{u}}.$$

Trivially, for magnitude and phase images,

$$\begin{aligned} T_m\left(\begin{bmatrix} \rho \\ \phi \end{bmatrix}\right) &= \begin{bmatrix} \rho \\ \phi \end{bmatrix}, \quad \hat{\boldsymbol{u}}_m = \begin{bmatrix} 1 \\ 0 \end{bmatrix} \\ T_p\left(\begin{bmatrix} \rho \\ \phi \end{bmatrix}\right) &= \begin{bmatrix} \rho \\ \phi \end{bmatrix}, \quad \hat{\boldsymbol{u}}_p = \begin{bmatrix} 0 \\ 1 \end{bmatrix}. \end{aligned}$$

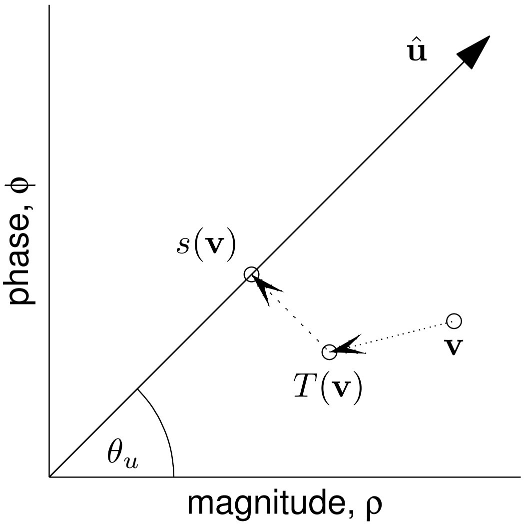

Figure 19: The projection framework, denoting the transformation, T, and projection onto axis $\hat{\boldsymbol{u}}$ of the two-dimensional data vector $\boldsymbol{v}$.

6.1.2 *The Optimised Contrast Image method*

The Optimised Contrast Image (OCI) method is an algorithm that determines an optimised projection axis, $\hat{\boldsymbol{u}}_{oci}$, and transformation, T_{oci}, for the projection from complex-valued MRI signal intensities to scalar-valued image intensities, such that contrast is maximised in the output image. Contrast can be selected to be within tissue types, between tissue types or a weighted combination of the two. The OCI procedure is based on a bivariate Gaussian mixture model (GMM) classification of the magnitude-phase intensity distribution into a pre-selected N tissue classes defined by mean vectors, $\Phi = \{\boldsymbol{\mu}_1, \dots, \boldsymbol{\mu}_N\}$, and corresponding covariance matrices, $\Psi = \{\Sigma_1, \dots, \Sigma_N\}$. The classes are ordered by mean magnitude intensity such that $\rho_1 \le \rho_2 \le ... \le \rho_N$ (see Fig. 20).

In projection framework notation, the OCI method is defined by

$$s(\boldsymbol{v}; T_{oci}, \hat{\boldsymbol{u}}_{oci}) = T_{oci}(\boldsymbol{v}) \cdot \hat{\boldsymbol{u}}_{oci}, \tag{6.1}$$

$$T_{oci}(\boldsymbol{v}) = \boldsymbol{v} + \sum_{k=1}^{N} p_k(\boldsymbol{v}) \, ||\boldsymbol{\mu}_k - \boldsymbol{\mu}_{k,oci}|| \, \hat{\boldsymbol{u}}_{oci}. \tag{6.2}$$

Here $p_k(\boldsymbol{v})$ is the probability (normalised likelihood) of the intensity vector, $\boldsymbol{v}$, belonging to the k^{th} mixture class. The optimised projection axis, $\hat{\boldsymbol{u}}_{oci}$, and shifted class mean vectors, $\Phi_{oci} = \{\boldsymbol{\mu}_{1,oci}, \dots, \boldsymbol{\mu}_{N,oci}\}$, are determined via optimisation of a cost function that weights intra- and inter-class contrast in the resultant image,

$$J(\alpha, \hat{\boldsymbol{u}}, \Phi, \Psi) = \alpha J_{inter}(\hat{\boldsymbol{u}}, \Phi, \Psi) + (1 - \alpha) J_{intra}(\hat{\boldsymbol{u}}, \Phi, \Psi), \tag{6.3}$$

via a tuning parameter, $0 \le \alpha \le 1$.

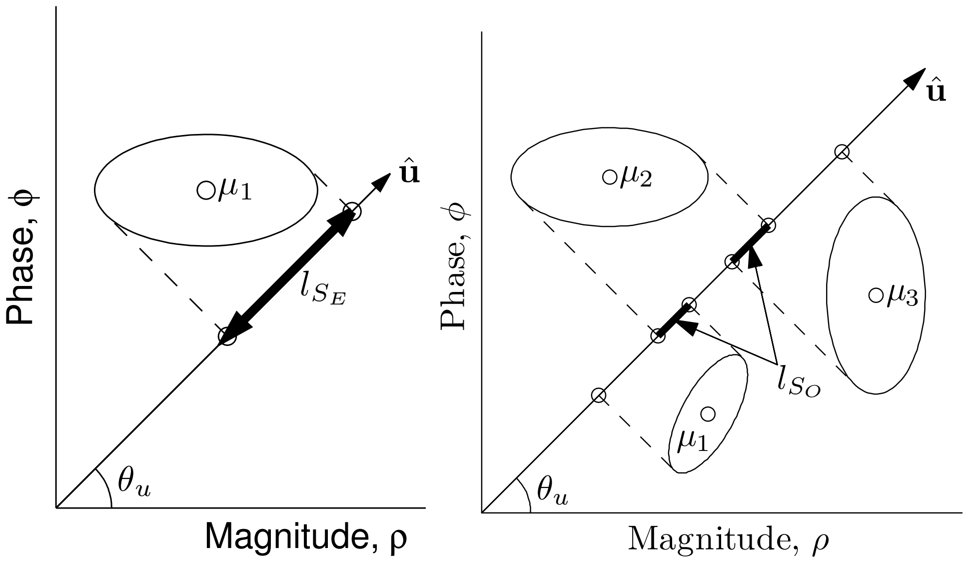

(a) (b)

Figure 20: The OCI method.

Before defining the contrast cost functions, J_{inter} and J_{intra}, definitions of ellipse shadow functions and associated measures are required. Let E_k denote the covariance ellipse formed by the k^{th} GMM tissue class that is centred at $\boldsymbol{\mu}_k$, with extent defined by two standard deviations of the covariance matrix Σ_k. We firstly define the shadow function, $S_E(r, \hat{\boldsymbol{u}}, \boldsymbol{\mu}_k, \Sigma_k)$, to be the indicator function formed by the perpendicular projection of E_k onto the axis $\hat{\boldsymbol{u}}$ (see Fig. 20a),

$$S_E(r,\hat{\boldsymbol{u}},\boldsymbol{\mu}_k,\Sigma_k) \tag{6.4}$$
$$\triangleq \begin{cases} 1, & \text{if } \exists c : r \begin{bmatrix} \cos\theta_{\hat{\boldsymbol{u}}} \\ \sin\theta_{\hat{\boldsymbol{u}}} \end{bmatrix} + c \begin{bmatrix} \sin\theta_{\hat{\boldsymbol{u}}} \\ \cos\theta_{\hat{\boldsymbol{u}}} \end{bmatrix} \in E_k \\ 0, & \text{otherwise} \end{cases} .$$

The length of the k^{th} shadow function is given by

$$l_{S_E}(\hat{\boldsymbol{u}},\boldsymbol{\mu}_k,\Sigma_k) \triangleq \arg\max_r \left[S_E(r,\hat{\boldsymbol{u}},\boldsymbol{\mu}_k,\Sigma_k) = 1\right]$$
$$- \arg\min_r \left[S_E(r,\hat{\boldsymbol{u}},\boldsymbol{\mu}_k,\Sigma_k) = 1\right], \tag{6.5}$$

and can be mathematically calculated by considering an ellipse centred at the origin with axis lengths a and b and rotated an angle θ from the magnitude axis, where

$$a = 2\sqrt{\lambda_1}, b = 2\sqrt{\lambda_2}, \theta = \angle\hat{\boldsymbol{e}}_1.$$

λ_1 and λ_2 are the eigenvalues of the covariance matrix Σ and $\hat{\boldsymbol{e}}_1$ is the eigenvector associated with λ_1. The points, $\boldsymbol{Q}$, on the ellipse are given by

$$\boldsymbol{Q} = \begin{bmatrix} \cos\theta & -\sin\theta \\ \sin\theta & \cos\theta \end{bmatrix} \begin{bmatrix} a\cos t \\ b\sin t \end{bmatrix}, \qquad 0 \le t < 2\pi.$$

The distance, L, of the projection of the vector from the origin to the point $\boldsymbol{Q}$ onto $\hat{\boldsymbol{u}}$ is given by

$$\begin{aligned} L &= \boldsymbol{Q}\cdot\hat{\boldsymbol{u}} = \begin{bmatrix} \cos\theta & -\sin\theta \\ \sin\theta & \cos\theta \end{bmatrix} \begin{bmatrix} a\cos t \\ b\sin t \end{bmatrix} \cdot \begin{bmatrix} \cos\theta_{\hat{u}} \\ \sin\theta_{\hat{u}} \end{bmatrix} && (6.6) \\ &= a\cos t\cos(\theta_{\hat{u}}-\theta) + b\sin t\sin(\theta_{\hat{u}}-\theta). && (6.7) \end{aligned}$$

l_{S_E} is given by twice L_{max}, the maximum of the magnitude of L, which occurs when $\frac{dL}{dt} = 0$.

$$\begin{aligned} \frac{dL}{dt} &= -a\cos(\theta_{\hat{u}}-\theta)\sin t + b\sin(\theta_{\hat{u}}-\theta)\cos t \\ &= 0 \\ \frac{\sin t}{\cos t} &= \frac{b\sin(\theta_{\hat{u}}-\theta)}{a\cos(\theta_{\hat{u}}-\theta)} \\ t &= \tan^{-1}\frac{b\sin(\theta_{\hat{u}}-\theta)}{a\cos(\theta_{\hat{u}}-\theta)}. && (6.8) \end{aligned}$$

Substituting (6.8) into (6.6) gives

$$\begin{aligned} L_{max} &= \Bigg| a\cos(\theta_{\hat{u}}-\theta)\cos\left(\tan^{-1}\frac{b\sin(\theta_{\hat{u}}-\theta)}{a\cos(\theta_{\hat{u}}-\theta)}\right) \\ &\qquad + b\sin(\theta_{\hat{u}}-\theta)\sin\left(\tan^{-1}\frac{b\sin(\theta_{\hat{u}}-\theta)}{a\cos(\theta_{\hat{u}}-\theta)}\right)\Bigg| && (6.9) \end{aligned}$$

Using the trigonometric identities

$$\begin{aligned} \cos\left(\tan^{-1}(x)\right) &= \frac{1}{\sqrt{1+x^2}}, \text{ and} && (6.10) \\ \sin\left(\tan^{-1}(x)\right) &= \frac{x}{\sqrt{1+x^2}} && (6.11) \end{aligned}$$

(6.9) becomes

$$\begin{aligned} l_{S_E} &= 2\left|\frac{a^2\cos^2(\theta_{\hat{u}}-\theta) + b^2\sin^2(\theta_{\hat{u}}-\theta)}{a\cos(\theta_{\hat{u}}-\theta)\sqrt{1+\frac{b^2\sin^2(\theta_{\hat{u}}-\theta)}{a^2\cos^2(\theta_{\hat{u}}-\theta)}}}\right| \\ &= 2\left|a\cos(\theta_{\hat{u}}-\theta)\sqrt{1+\frac{b^2\sin^2(\theta_{\hat{u}}-\theta)}{a^2\cos^2(\theta_{\hat{u}}-\theta)}}\right|. && (6.12) \end{aligned}$$

The range spanned by the union of all ellipse shadow functions is

$$r_{S_E}(\hat{\boldsymbol{u}},\Phi,\Psi) \triangleq \arg\max_r \left[\sum_{k=1}^{N} S_E(r,\hat{\boldsymbol{u}},\boldsymbol{\mu}_k,\Sigma_k) \neq 0 \right] - \arg\min_r \left[\sum_{k=1}^{N} S_E(r,\hat{\boldsymbol{u}},\boldsymbol{\mu}_k,\Sigma_k) \neq 0 \right]. \tag{6.13}$$

Similarly, we define the shadow overlap function, $S_O(r,\hat{\boldsymbol{u}},\Phi,\Psi)$, to be the indicator function formed by intersection of the ellipse shadow functions of two or more ellipses (see Fig. 20b),

$$S_O(r,\hat{\boldsymbol{u}},\Phi,\Psi) \triangleq \begin{cases} 1, & \text{if } \exists k \neq k' : S_E(r,\hat{\boldsymbol{u}},\boldsymbol{\mu}_k,\Sigma_k) = S_E(r,\hat{\boldsymbol{u}},\boldsymbol{\mu}_{k'},\Sigma_{k'}) = 1 \\ 0, & \text{otherwise} \end{cases} \tag{6.14}$$

The combined length of the disjoint intervals comprising the overlap shadow is denoted by $l_{S_O}(\hat{\boldsymbol{u}},\Phi,\Psi)$.

The lengths of the ellipse shadows gives a measure of intra-class contrast, as the width of the ellipse shadows determines the intensity variability within a tissue class. Similarly, the length of the overlap shadow provides a measure of inter-class contrast; less overlap between ellipse shadows results in greater contrast between tissue classes. Thus we define the intra- and inter-class contrast cost functions to be

$$J_{intra}(\hat{\boldsymbol{u}},\Phi,\Psi) \triangleq \frac{\sum_{k=1}^{N} l_{S_E}(\hat{\boldsymbol{u}},\boldsymbol{\mu}_k,\Sigma_k)}{r_{S_E}(\hat{\boldsymbol{u}},\Phi,\Psi)}, \tag{6.15}$$

$$J_{inter}(\hat{\boldsymbol{u}},\Phi,\Psi) \triangleq \frac{l_{S_O}(\hat{\boldsymbol{u}},\Phi,\Psi)}{r_{S_E}(\hat{\boldsymbol{u}},\Phi,\Psi)}. \tag{6.16}$$

The optimisation is solved in a two-step procedure. Firstly, the optimal projection axis is calculated such that the intra-class contrast is maximised,

$$\hat{\boldsymbol{u}}_{oci} = \arg\max_{\hat{\boldsymbol{u}}} \; J_{intra}(\hat{\boldsymbol{u}},\Phi,\Psi) \tag{6.17}$$

$$\text{s.t. } \boldsymbol{\mu}_k = \boldsymbol{\mu}_{k'} \quad \forall k,k' = 1,\ldots,N \tag{6.18}$$

where the constraints align the means of all classes. Secondly, the optimal mean shifts are determined by

$$\begin{aligned}\Phi_{oci} &= \arg\max_{\Phi} \; J(\hat{\boldsymbol{u}}_{oci}, \Phi, \Psi) \\ \text{s.t. } & \boldsymbol{\mu}_{k+1,oci} \cdot \hat{\boldsymbol{u}}_{oci} - l_{S_E}(\hat{\boldsymbol{u}}_{oci}, \boldsymbol{\mu}_{k,oci}, \Sigma_k) \\ & \qquad - l_{S_E}(\hat{\boldsymbol{u}}_{oci}, \boldsymbol{\mu}_{k+1,oci}, \Sigma_{k+1}) \\ & \leq \; \boldsymbol{\mu}_{k,oci} \cdot \hat{\boldsymbol{u}}_{oci} \; \leq \; \boldsymbol{\mu}_{k+1,oci} \cdot \hat{\boldsymbol{u}}_{oci} \quad \text{for } k = 1, , ..., N-1.\end{aligned} \tag{6.19}$$

The constraints ensure that the ordering of classes in the magnitude direction is retained and that adjacent classes are not shifted beyond a maximum separation between their means, defined to be the sum of two standard deviations for both classes. Note that in order for the OCI algorithm to be robust to outlier intensities, the magnitude and phase data are scaled such that the mean plus or minus two standard deviations maps to the interval $[0, 1]$.The OCI procedure is summarised in the following three steps.

Algorithm 6.1 Optimised Contrast Image algorithm

1. Estimate N-class Gaussian mixture model fit to magnitude-phase data.
   Output: Φ, Ψ, $p_k(\boldsymbol{v})$.
2. Solve contrast optimisation (6.17)–(6.19) for a chosen α.
   Output: Φ_{oci}, $\hat{\boldsymbol{u}}_{oci}$.
3. Project magnitude-phase data onto $\hat{\boldsymbol{u}}_{oci}$ via (6.1)–(6.2).
   Output: Optimised Contrast Image

6.1.3 *Susceptibility Weighted Imaging (SWI)*

In the projection framework, SWI consists of a non-linear intensity transformation, according to either a negative mask,

$$T^{-}_{swi}(\boldsymbol{v}) = \begin{cases} \begin{bmatrix} \rho \left(\frac{\pi+\phi}{\pi}\right)^{n} \\ \phi \end{bmatrix}, & \phi < 0 \\ \begin{bmatrix} \rho \\ \phi \end{bmatrix}, & \phi \geq 0 \end{cases}$$

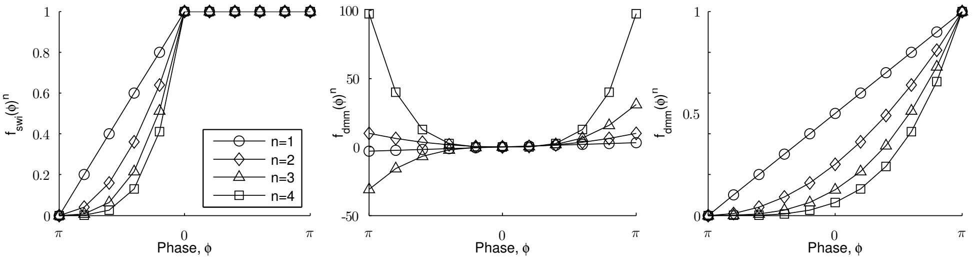

(a) (b) (c)

Figure 21: Effect of the mask on magnitude intensities for (a) SWI, (b) DMM without normalisation of the phase and (c) DMM with normalisation of the phase.

or a positive mask,

$$T^{+}_{swi}(\boldsymbol{v}) = \begin{cases} \begin{bmatrix} \rho \\ \phi \end{bmatrix}, & \phi < 0 \\ \begin{bmatrix} \rho\left(\frac{\pi-\phi}{\pi}\right)^{n} \\ \phi \end{bmatrix}, & \phi \geq 0 \end{cases}$$

SWI projects image intensities onto the magnitude axis, thus

$$\hat{\boldsymbol{u}}_{swi} = \begin{bmatrix} 1 \\ 0 \end{bmatrix}.$$

6.1.4 *Direct Multiplication Method (DMM)*

Contrast information in one half of the phase spectrum is always omitted in SWI: the positive phase values when negative masks are used, and vice-versa. Abduljalil *et al.* [12] proposed a method similar to SWI which utilises the full phase spectrum, with projection transformation and axis given by

$$\begin{aligned} T_{abd}(\boldsymbol{v}) &= \begin{bmatrix} \rho\left(\frac{\phi+\pi}{2\pi}\right)^{n} \\ \phi \end{bmatrix}, \\ \hat{\boldsymbol{u}}_{abd} &= \begin{bmatrix} 1 \\ 0 \end{bmatrix}. \end{aligned}$$

The use of the phase image with no further manipulation presents a problem, however. If the number of times the mask is applied, n, is odd, voxels with negative phase values will be severely attenuated (Fig 21b). If n is even, the effect will always be accentuation rather than attenuation, and there will be no distinction made between negative and positive phase angles.

We propose an adaptation of the method, which will be referred to as the Direct Multiplication Method (DMM). The phase is normalised by translating and scaling the range $[-\pi, \pi]$ to the range $[0, 1]$ (Fig 21c), thus eliminating the problem present in the original method. The optimal value, n^*, for voxel attenuation producing image contrast is dependent on the range and distribution of values in the phase image. For a range of normalised phase values $[\phi_{min}, \phi_{max}]$, the optimal n occurs when the difference in the corresponding magnitude transformation component is greatest and n is restricted to values greater or equal to 1. Let

$$g(n) = \left(\frac{\phi_{max} + \pi}{2\pi}\right)^n - \left(\frac{\phi_{min} + \pi}{2\pi}\right)^n.$$

The optimal n is found by turning point analysis,

$$\begin{aligned}\frac{dg(n)}{dn} &= \ln\left(\frac{\phi_{max} + \pi}{2\pi}\right)\left(\frac{\phi_{max} + \pi}{2\pi}\right)^n \\ &\quad - \ln\left(\frac{\phi_{min} + \pi}{2\pi}\right)\left(\frac{\phi_{min} + \pi}{2\pi}\right)^n = 0,\end{aligned}$$

giving a value of n^*, not to be restricted to integer values,

$$n^* = \frac{\ln\left(\frac{\ln\left(\frac{\phi_{max}+\pi}{2\pi}\right)}{\ln\left(\frac{\phi_{min}+\pi}{2\pi}\right)}\right)}{\ln\left(\frac{\phi_{min}+\pi}{\phi_{max}+\pi}\right)}.$$

6.2 METHODS

6.2.1 *Data Acquisition*

3T cortical phase and magnitude images of a healthy human volunteer were acquired using a Siemens TIM Trio 3T system with a Siemens 12 channel Head Matrix Coil (Siemens Medical Solutions, Erlangen, Germany) using the following imaging parameters: axial 2D Gradient Recall Echo, T_2^*-weighted imaging with TE $=$ 45 ms, TR $=$ 1000 ms, flip angle $=$ 45°, slice thickness $=$ 2.5 mm, FOV $= 240 \times 180$ mm^2, image matrix size $= 384 \times 448$. The magnitude image was reconstructed using SENSE. The phase image was reconstructed using a phase optimised SENSE method [13] and unwrapped using 2D complex filtering with a standard deviation of 10 k-space voxels.

7T data of a healthy male volunteer (age 27) were acquired on a 7T Siemens system (Siemens Medical Solutions, Erlangen, Germany) with an 8-channel transmit-receive head coil (Neuroscience Research Institute, Incheon, South Korea) using the following parameters: axial 2D gradient echo (GRE), T_2^*-weighted imaging with TE = 21.6 ms, TR = 750 ms, flip angle = 30°, bandwidth = 30 Hz per pixel, slice thickness = 2 mm, FOV = 256×224 mm^2, matrix size = 1024×896. Spatial resolution was$0.25 \times 0.25 \times 2$ mm^3. A total of 17 slices were acquired. The total scan time was 11 min 30 s. The magnitude and phase images were reconstructed using the optimised complex reconstruction method [13]. The phase wraps and background inhomogeneities were removed using 2D complex filtering with a standard deviation of 10 k-space voxels.

6.2.2 *Contrast quantification*

Quantitative analysis of contrast was achieved by calculation of image intensity ranges over selected line profiles through the images, and entropy calculation. All image intensities were normalised to the range $[0, 1]$. Line profile voxel intensities were normalised such that

$$s'(v) = \frac{s(v) - \min\left(s(v)\right)}{\max\left(s(v)\right) - \min\left(s(v)\right)}$$

where $\min\left(s(v)\right)$ and $\max\left(s(v)\right)$ are the minimum and maximum intensities of all voxels in the image.

Entropy, E, was calculated using

$$E = -\sum_{i=1}^{N} p(x_i) \log_2 p(x_i)$$

where $p(x_i)$ is the histogram-based probability of the voxel intensity lying in the interval $[x_i - \frac{\delta x}{2}, x_i + \frac{\delta x}{2})$ and $\delta x = x_i - x_{i-1}$. Outlier intensities above and below three standard deviations of the mean are mapped to 1 and 0 respectively, and background voxels are ignored.

6.3 RESULTS

6.3.1 *3T images*

Figure 22 presents the results applied to the 3T cortical slice. The magnitude image shows distinct inter-class contrast (Fig. 22a), while the phase image displays greater intra-class contrast (Fig. 22b). This visual evaluation is supported quantitatively by the GMM classification (Fig. 22c), which demonstrates greater separation of class means in the magnitude direction compared to the phase direction, but larger standard deviations in the phase direction compared to the magnitude direction. The GMM provided distinct classification of tissue classes (Fig. 22c-d), with the 1st (green) class representing predominantly white matter (WM) voxels, the 2nd (red) class representing predominantly grey matter (GM) voxels and the 3rd (light blue) class representing predominantly cerebrospinal fluid (CSF) voxels. The 4th (blue) class has a much larger standard deviation than the other classes and represents not only background voxels, but voxels on the periphery of the brain that have high magnitude intensity and/or very high or low phase intensities.

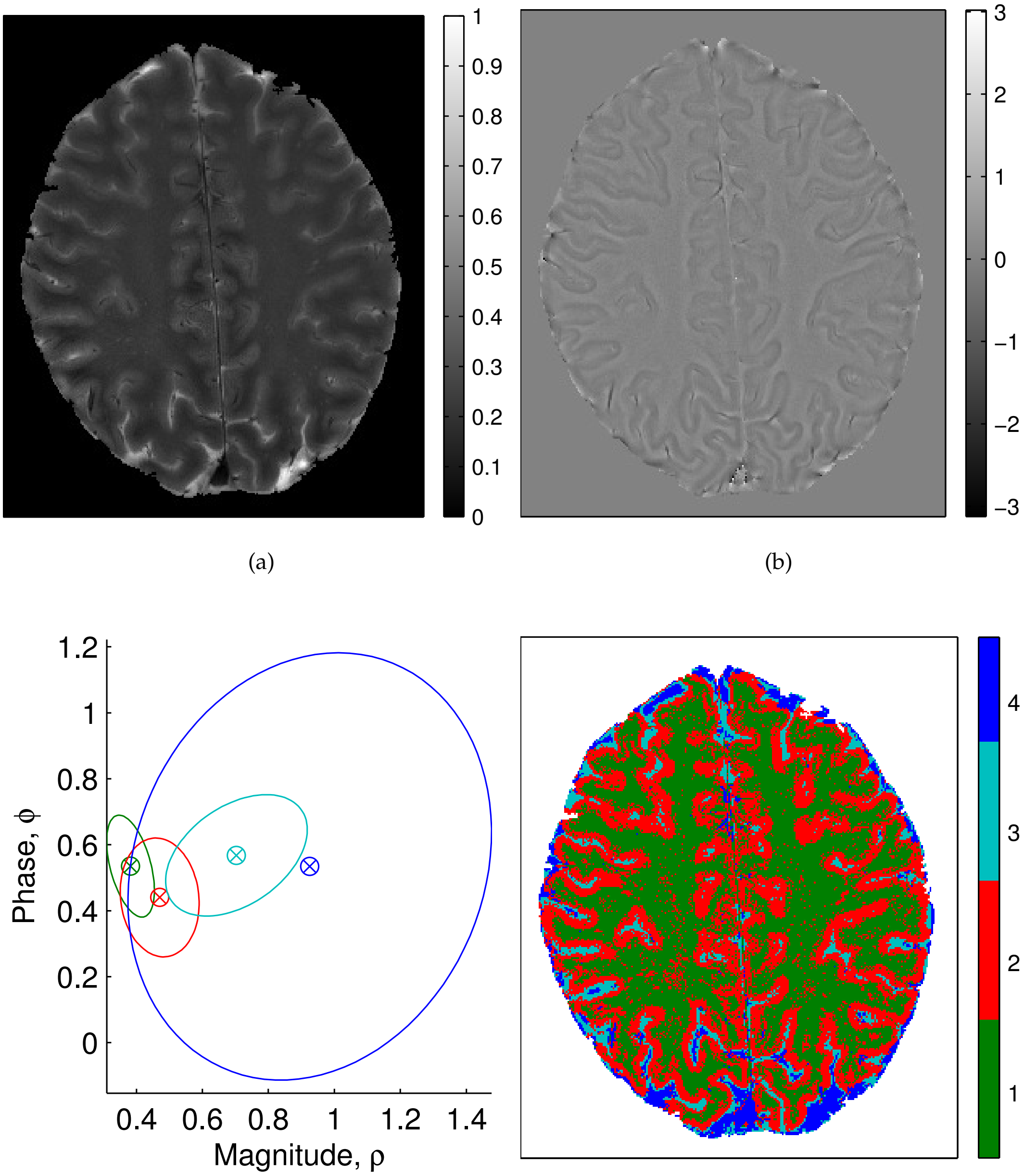

(a) (b)

(c) (d)

Figure 22: Cortical slice at 3T: (a) magnitude image, (b) phase image, (c) 4-component GMM ellipses indicating the covariance of each class, (d) classification of voxels into tissue classes.

A series of OCI results are presented in Fig. 23a-d for varying tuning parameter α values. The effect of α on inter-class and intra-class contrast is observable in the OCI images. As expected, high intra-class contrast is demonstrated at α=0, through to high inter-class contrast image at α=1.

The large covariance of the 4th tissue class and outlying voxel intensities attributed to this class affected the overall contrast in the $\alpha = 0$ image. A rescaling of the α=0 OCI image (Fig. 23b), in which the full grey-scale spans the three standard deviation intensity range, demonstrates the intricate detail contained in the image. This OCI result resembles an inverted phase image, where the inversion is a result of the constraint on class intensity ordering (6.19).

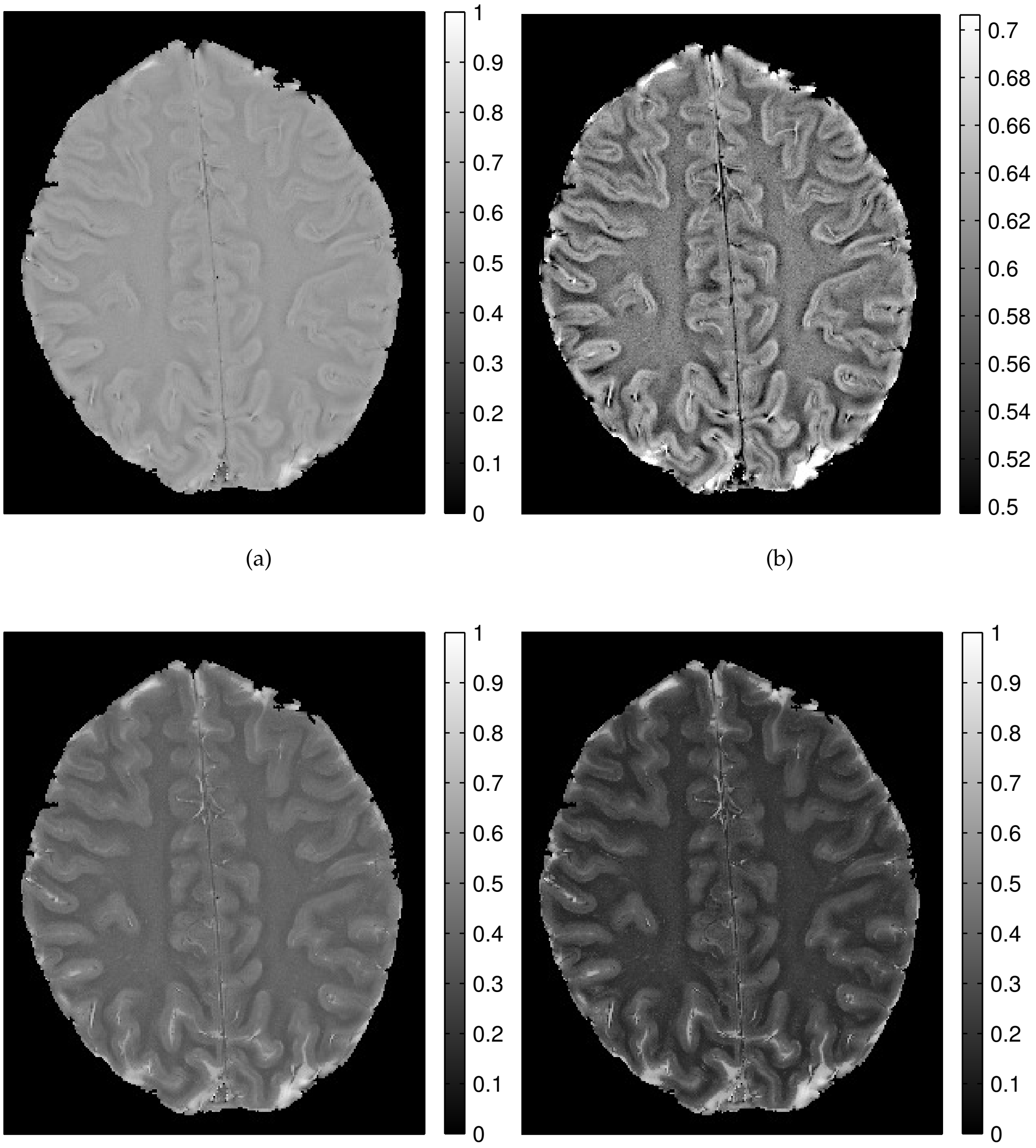

(a) (b) (c) (d)

Figure 23: OCI images: (a) α=0, (b) α=0 with the full grey-scale spanning the range defined by $\mu \pm 3\sigma$, (c) α=0.5, and (d) α=1.

The positive mask SWI image (Fig. 24a) demonstrates greater inter-class contrast, particularly at tissue borders, compared to the negative mask SWI image (Fig. 24b), the magnitude image (Fig 22a) and the phase image (Fig 22b). In comparison to the OCI images, it is most similar to the α=1 image, although inter-class contrast is greater in the OCI image. The DMM image (Fig. 24c) does not display significant improvement in contrast compared to the magnitude image and is visually the least effective method.

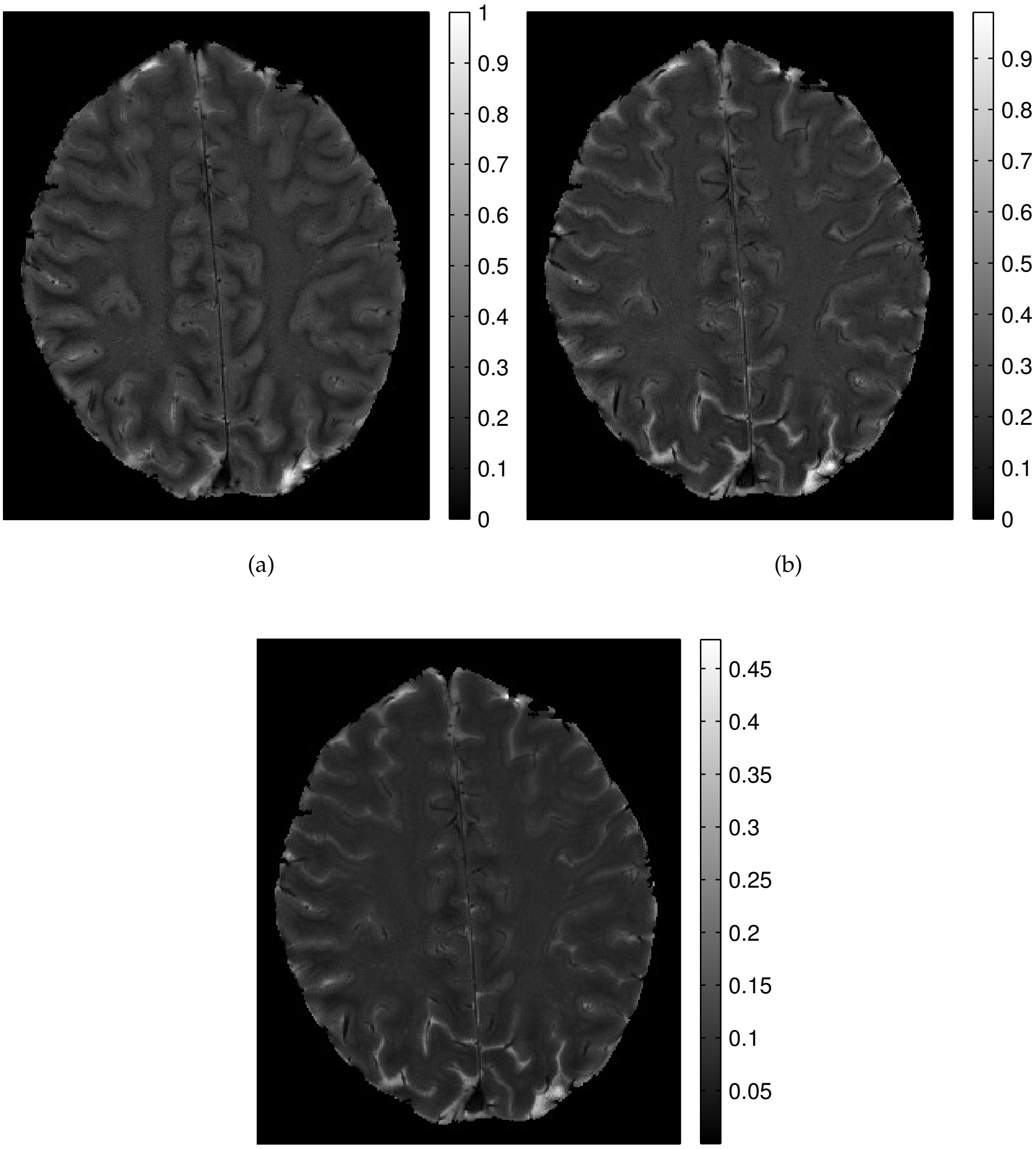

(a)

(b)

(c)

Figure 24: SWI with (a) positive mask (n=4), (b) negative mask (n=4) and(c) DMM (n=1.44).

Line profiles, taken across a several sulci (Fig. 25a-b), highlight the difference in contrast between the magnitude, phase, positive mask SWI and OCI α=1 images (Fig. 25c). The magnitude demonstrates larger intensity variation between GM and WM regions compared to the phase. The SWI profile is similar to the magnitude profile, with some diminution of the peak heights. OCI combines the contrast profiles of the magnitude and phase. It has the largest inter-class variation of the four profiles, demonstrates steep gradients at the GM/WM borders, maintains both the intra-class features of the phase profile and the high intensity peaks of the magnitude profile.

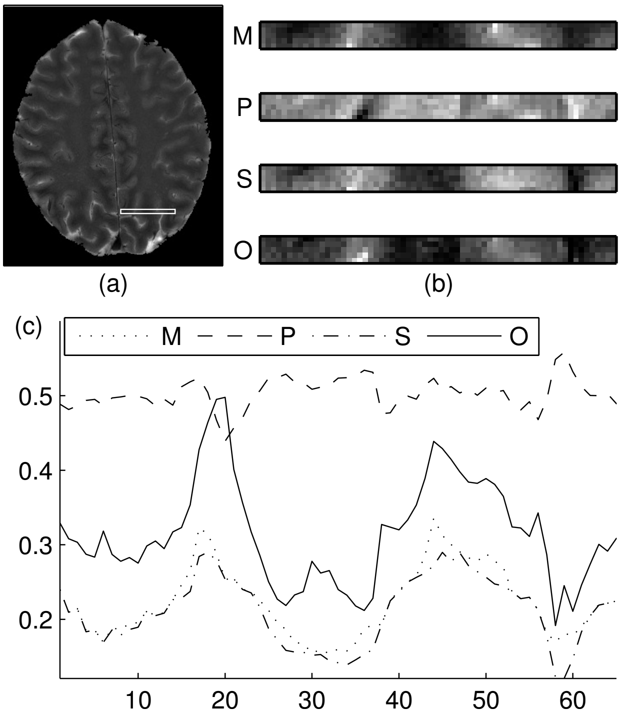

Figure 25: Line profiles from the 3T images. The rectangle in the (a) magnitude image indicates the location of the line. (b) displays the sections of each image that are plotted. The (c) plots show the profiles for the (M) magnitude, (P) phase, (S) SWI positive mask and (O) $\alpha = 1$ OCI.

OCI retains more information, as quantified by entropy (Table 3); the $\alpha = 1$ OCI image returned the highest entropy value across all images. The OCI $\alpha = 0.5$, SWI and magnitude images have comparable entropies, varying by 1.6% of the magnitude entropy. The entropy of the $\alpha = 0$ OCI is 43% higher than that of phase, implying that while the image does resemble the phase, information from the magnitude has been incorporated. The DMM entropy is the second lowest and the phase entropy is the lowest at 37.5% lower than the magnitude entropy.

Table 3: Entropies for the 3T images.

Image	Entropy
OCI $\alpha = 1$	4.83
SWI$^+$	4.50
OCI $\alpha = 0.5$	4.49
SWI$^-$	4.46
magnitude	4.43
OCI $\alpha = 0$	4.15
DMM	3.56
phase	2.77

A comparison of the histograms of voxels in each class (Fig. 26) illustrates the increase in distances between the distribution means as α tends from 0 to 1. At $\alpha = 0$, the standard deviation of each class is narrow compared to the full intensity range $[0, 1]$, but wide when considered as a proportion of the standard deviation of all voxels, a result of outlying voxels affecting the intensity range of the image. As α tends towards 1, the standard deviation of each class decreases as a proportion of the standard deviation of all voxels, indicating a reduction in intra-class contrast.

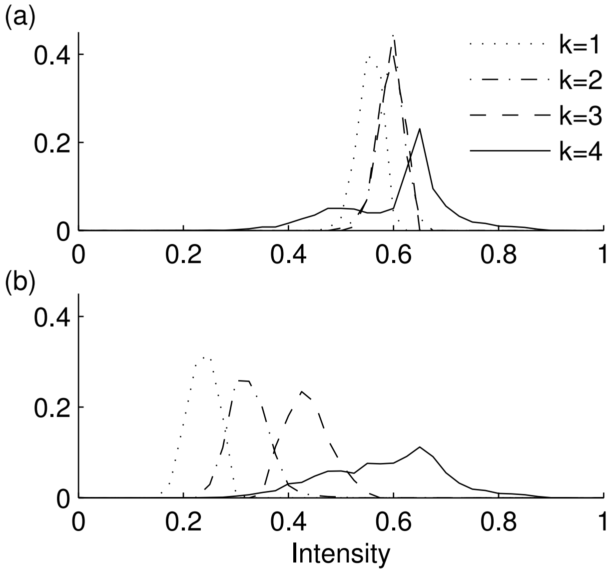

Figure 26: Histograms depicting the separation of class distributions as α varies from (a) 0 to (b) 1 in the 3T OCI images.

6.3.2 *7T images*

The cortical 7T magnitude and phase images (Fig. 27) demonstrate different contrast patterns, with the phase image showing more detail than the magnitude image. The magnitude image (Fig. 27b) demonstrates a small difference in intensity between GM and WM. The GM/WM border definition is poor, particularly in the top half of the image. In contrast, the phase image (Fig. 27c) displays distinct GM/WM border definition which is not always observable in the magnitude image. The venous structures are also more clearly visible in the phase image. The GMM classification (Fig. 27d-e) resulted in a 1st (blue) class that predominantly represents venous vessels but also low magnitude intensity GM voxels, 2nd (green) and 3rd (red) classes representing WM and GM respectively, and the 4th (cyan) class composed of CSF and high magnitude intensity WM voxels.

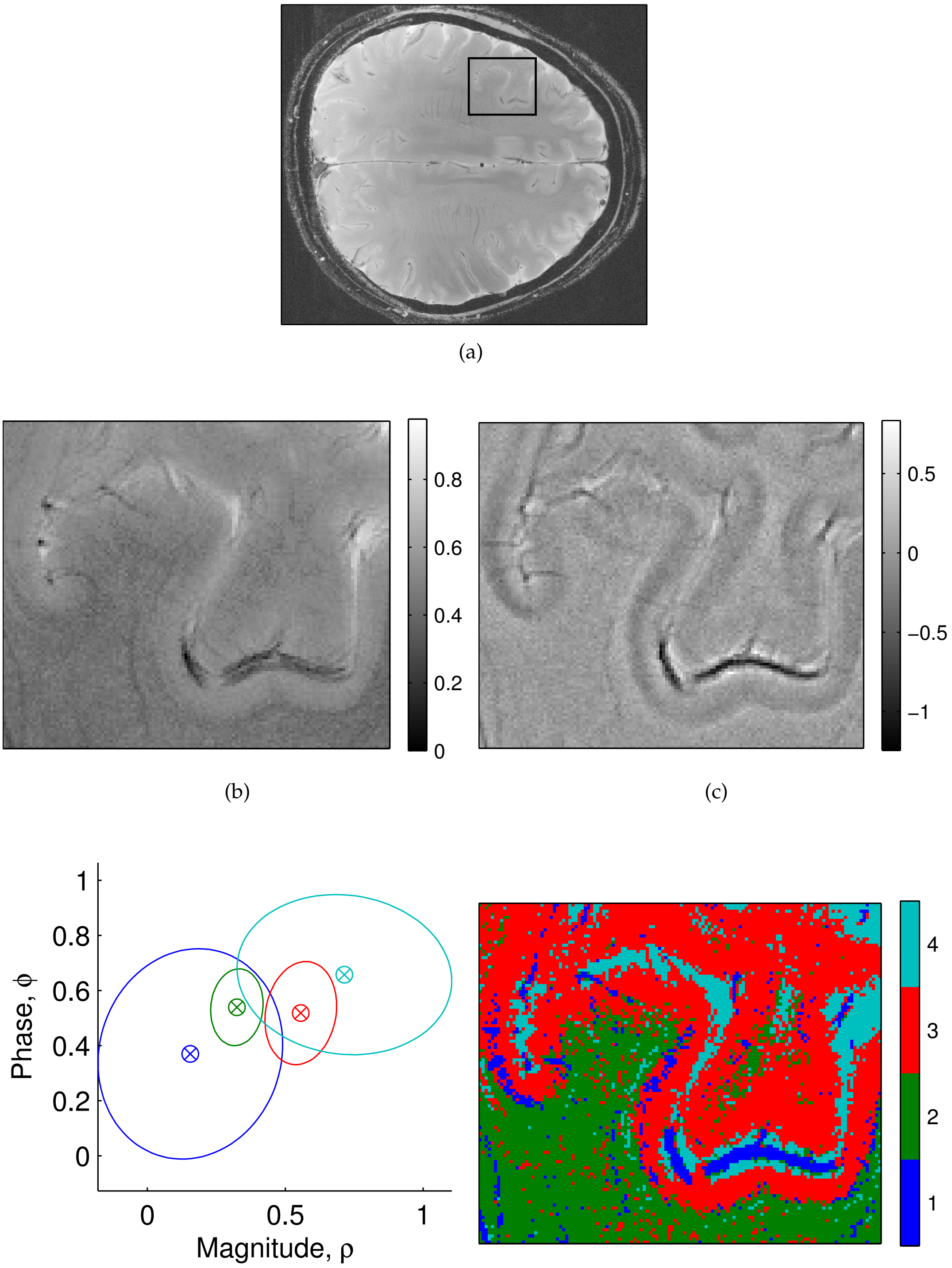

(a)

(b)

(c)

(d)

(e)

Figure 27: Cortical section at 7T: (a) position of section, (b) magnitude image, (c) phase image, (d) 4-component GMM ellipses indicating the covariance of each class, (e) classification of voxels into tissue classes.

The OCI images (Fig 28) show increasing inter-class contrast as α tends towards 1. The $\alpha = 0$ image demonstrates high intra-class contrast and resembles an inverted phase image with bright venous vessels in the GM, although the vessels in the WM in the lower left quadrant are not visible. As α tends towards 1, the vessels in the GM become less prominent, while, at $\alpha = 0.5$, the vessels in the WM are visible. At $\alpha = 1$, the GM/WM border in the top right quadrant becomes less distinct than at lower α, however the detail in the lower half of the image becomes clearer, with greater GM/WM contrast and more visible vessels in the WM. The large venous vessel between the GM/GM border in the lower right quadrant is visible in all OCI images, with the GM/CSF border also retaining visibility.

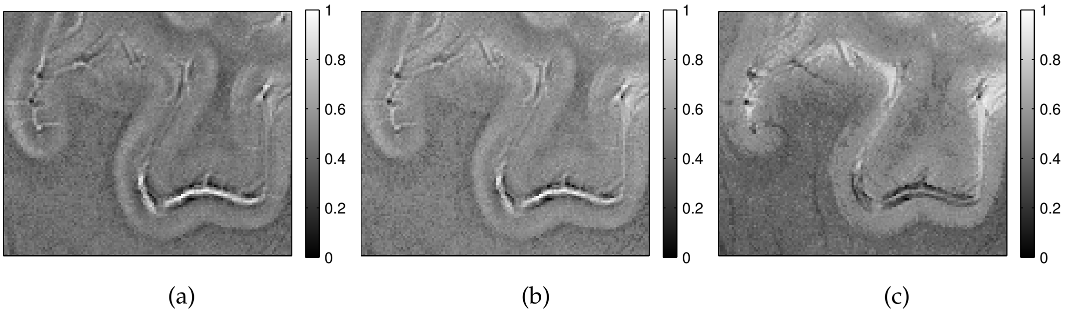

(a) (b) (c)

Figure 28: OCI images at 7T: (a) α=0, (b) α=0.5, and (c) α=1.

The SWI images accentuate different features within the image. The positive mask SWI (Fig. 29a) delineates tissue borders clearly and displays intensity contrast between the GM and WM. Veins and tissue borders are more visible in the negative mask SWI (Fig. 29b) compared to the magnitude image (Fig 27b), although the tissue borders lack distinct delineation. The voxels around and including the large vessel between the GM surfaces are particularly attenuated in the negative mask SWI. The low intensity voxels in the magnitude and phase images combine to create a wide dark band that hides the edge profile visible in the phase image (Fig 27c). In comparison to the contrast effects of the SWI method, the DMM image (Fig. 29c) does not demonstrate significant improvement over the magnitude or phase image.

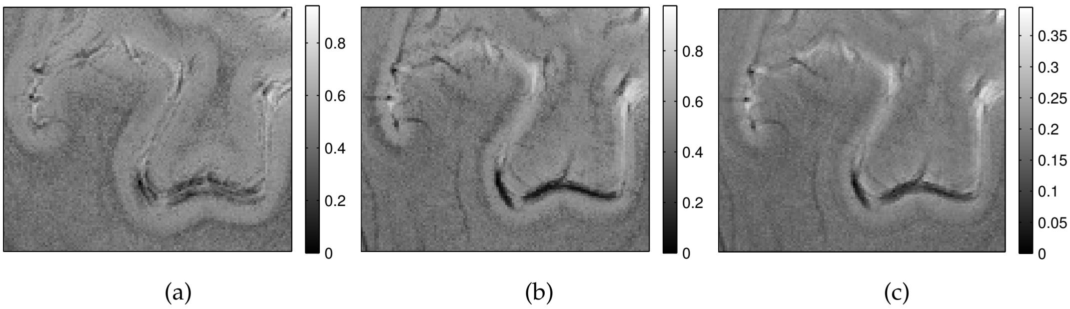

(a) (b) (c)

Figure 29: SWI with (a) positive mask (n=4), (b) negative mask (n=4) and (c) DMM (n=1.43).

Figure 30 displays line profiles across the large vessel in the lower right quadrant of the images. The magnitude and phase profiles indicate a one voxel variation in the location of the GM/CSF border, although the profiles are in agreement regarding the positioning of the CSF/vein border. The delineation of the large vessel in the OCI image retains not only the visibility of the vessel, but also the definition of the GM/CSF border. In comparison positive mask SWI profile demonstrates that the definition of the GM/CSF border around the large vessel is lost although the vessel remains visible. The negative mask SWI profile indicates a GM/CSF border corresponding to the magnitude image, while the contrast at the CSF/vein border is lost.

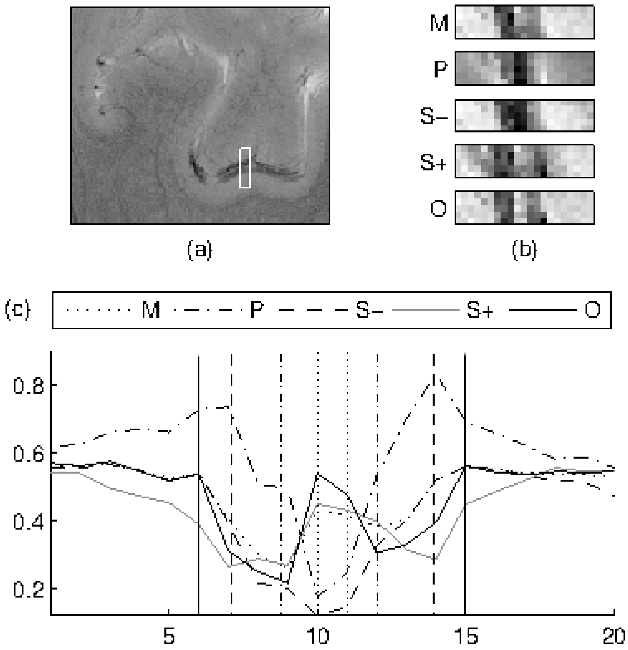

Figure 30: Line profiles from the 7T images. The location of the line is indicated in the (a) magnitude image and the relevant sections of each image are shown in (b). The (c) plots show the profiles for the (M) magnitude, (P) phase, (S-) SWI negative mask, (S+) SWI positive mask and (O) $\alpha = 1$ OCI. The vertical lines represent the magnitude (solid) and phase (dashed) CSF/GM boundary, and the magnitude (dash-dotted) and phase (dotted) CSF/vessel boundary.

The entropy (Table 4) of the phase image is 33% lower than that of the magnitude. All OCI images have greater entropies than the magnitude, ranging from 1.1% higher at $\alpha = 0$ to 10.1% higher at $\alpha = 1$, the highest of all the image entropies. The entropies of the negative and positive mask SWI are 3.8% and 1.6% higher than the magnitude. The DMM has an entropy 18.1% lower than the magnitude.

Table 4: Entropies for the 7T images.

Image	Entropy
OCI $\alpha = 1$	6.74
SWI^{-}	6.35
OCI $\alpha = 0.5$	6.30
SWI^{+}	6.22
OCI $\alpha = 0$	6.19
magnitude	6.12
DMM	5.01
phase	4.08

The histograms of classified voxel intensities (Fig. 31) demonstrate a widening distance between class means and narrowing of the standard deviations with increasing α, indicating that the inter-class contrast increases and the intra-class contrast reduces as α increase.

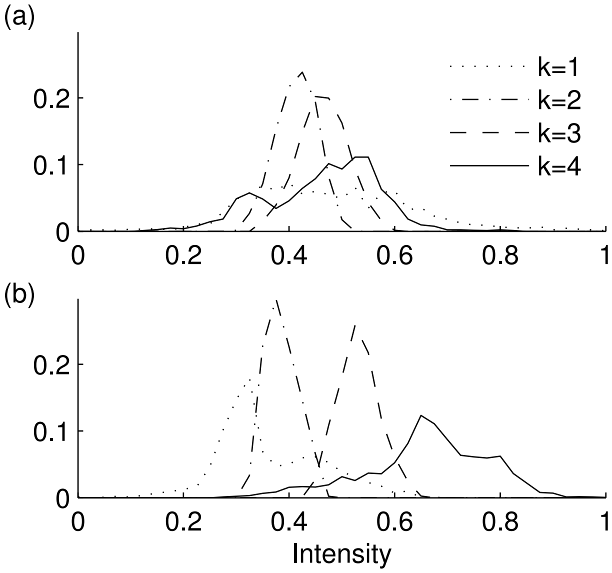

Figure 31: Histograms depicting the separation of class distributions as α varies from (a) 0 to (b) 1 in the 7T OCI images.

6.4 DISCUSSION

The OCI method is a classification-based contrast enhancement method based on a Gaussian mixture model representation of the bivariate image data. We have demonstrated that the OCI method is flexible and effective in combining phase and magnitude information, producing images with greater intra- and inter-class contrast and clearer border definition compared to the DMM and SWI methods.

The success of the OCI method relies on the representation of the data by a GMM. Each class in the GMM should be representative of one specific structure or tissue type, therefore the number of classes in the model should equal the number of distinct structures. Modelling of too few classes will restrict the methods ability to enhance inter-class contrast at high α, while too many classes will increase the methods sensitivity to noisy voxels. The covariances of the individual Gaussian distributions greatly influence the ability of the OCI method to enhance the contrast in the image. If the covariance of one class is considerably larger than the other classes, it will dominate the grey-scale range. At low α, this would cause a reduction in the intensity range of the other classes relative to the full extent of the grey-scale, thus reducing intra-class contrast in the smaller classes. The dominance of the large class also increases the sensitivity of the overall image contrast to outlying voxel intensities. At high α, the large class will continue to dominate the full contrast range and will result in reduced inter-class contrast for smaller adjacent classes. The remaining parameters combine with the covariance to the determine the weighting of class shifts attributed to each voxel. If the GMM parameters result in the majority of voxels being predominantly weighted to the same class, then the OCI method will have little effect in enhancing either intra-class or inter-class contrast.

The tuning parameter α weights the intra- and inter-class contrasts in the image. At low α, intra-class contrast dominates over inter-class contrast. Given the tendency in MRI for the phase image to have greater intra-class contrast than inter-class contrast compared to the magnitude image, the $\alpha = 0$ OCI is expected to resemble the phase image, which has been observed in our results. As α tends towards 1, greater emphasis is placed on inter-class contrast and the results indicate an increased contrast between the different classes. At $\alpha = 1$, the optimisation is no longer dependent on the intra-class contrast. Without the constraint placed on the separation of shifted means in (6.19), the shifts could tend towards ∞, resulting in a highly quantised image.

The OCI method inherently reduces noise as α increases. The weighting of shifts avoids the amplification of noisy voxels that can result from hard classification. Furthermore, the separation of classes as α tends towards 1 effectively reduces the standard deviation of the class relative to the standard deviation of all voxels, thus reducing the noise within each class. Nevertheless, the OCI method does not seek to distinguish between noise and 'true' signal intensity variation. Therefore, given data where the majority of intensity variation is attributable to noise, the OCI method would treat the variation as intra-class contrast and effect an amplification of the noise, particularly at low α.

The OCI method performs well compared to other methods at combining magnitude and phase data to produce an optimised contrast image. The entropies of the SWI and higher α OCI images are similar and higher than both the magnitude and phase images, implying that both methods successfully combine information from the magnitude and phase to produce images with greater overall contrast. The entropy, however, is not dependent on the spatial variation of intensities and therefore does not give indication of the level of intra-class contrast or delineation of class borders. These are apparent in the line profiles, which indicate a greater degree of intra-class contrast and clearer delineation between classes in the higher α OCI images compared to all other images.

The OCI method demonstrates applicability in GM/WM contrast enhancement and in venography. Of the three SWI-based methods, DMM is the least successful at producing an image with contrast that is enhanced over the magnitude or the phase image. The positive mask method is the most successful of the SWI methods at enhancing GM/WM contrast, while the negative mask method demonstrates its applicability in the area of venography.

The contrast pattern in the positive mask SWI images are similar to the contrast patterns in the OCI $\alpha = 1$ images. Both methods prove useful in enhancing GM/WM tissue contrast. At 3T, distinct contrast is apparent between tissue classes in the magnitude image. The GM/WM contrast is reflected in both the positive mask SWI and OCI images, although the OCI images demonstrate clearer edge-definition and enhancement of CSF, which appears attenuated in the positive mask SWI image. At 7T, the tissue contrast enhancement is again apparent, although to a lesser degree than at 3T due to the low contrast in the original magnitude data.

The negative mask SWI method produced images with distinctly different contrast patterns to the OCI. The overall effectiveness of SWI as a venography method is demonstrated in the 7T images, with small venous vessels appearing throughout the image. Similar vessels appear in the OCI $\alpha = 1$ image, although the pattern of vessels differs. In situations where low magnitude intensity exists alongside low phase intensity, the results have demonstrated that discrepancies in border definition can occur. Using negative phase as a measure of the presence of venous vessels, a notion that forms the basis of the SWI method, OCI is shown in the 7T data to faithfully represent the vessel width, while the negative mask SWI overestimates the width of the vessel.

6.5 CONCLUSION

The ability of the proposed OCI method to optimise for a chosen combination of intra- and inter-class contrast makes it a valuable tool for visualising structural details in MRI data. The method is classification-based and can be compared to a segmentation method based on bivariate classification. However, the projection of voxels onto an optimised axis and the soft classification of voxels implemented by the weighted shifts allows for the production of an image which not only depicts the segmentation, but also retains the localised detail in the original data. We have demonstrated the improvement in contrast and edge definition provided by OCI over three variants of SWI.

BIBLIOGRAPHY

[1] Jeff H. Duyn, Peter van Gelderen, Tie-Qiang Li, Jacco A. de Zwart, Alan P. Koretsky, and Masaki Fukunaga. High-field MRI of brain cortical substructure based on signal phase. *Proceedings of the National Academy of Sciences*, 104(28):11796–11801, July 2007.

[2] Xiang He and Dmitriy A. Yablonskiy. Biophysical mechanisms of phase contrast in gradient echo MRI. *Proceedings of the National Academy of Sciences*, 106(32):13558–13563, 2009.

[3] Y. Wang, Y. Yu, D. Li, K.T. Bae, J.J. Brown, W. Lin, and E.M. Haacke. Artery and vein separation using susceptibility-dependent phase in contrast-enhanced MRA. *Journal of Magnetic Resonance Imaging*, 12(5):661–670, 2000.

[4] Jürgen R Reichenbach and E. Mark Haacke. High-resolution BOLD venographic imaging: a window into brain function. *NMR in Biomedicine*, 14(7-8):453–467, 2001.

[5] E. Mark Haacke, Yingbiao Xu, Yu-Chung N. Cheng, and Jürgen R. Reichenbach. Susceptibility weighted imaging (SWI). *Magnetic Resonance in Medicine*, 52(3):612–618, 2004.

[6] Vivek Sehgal, Zachary Delproposto, E. Mark Haacke, Karen A. Tong, Nathaniel Wycliffe, Daniel K. Kido, Yingbiao Xu, Jaladhar Neelavalli, Djamel Haddar, and Jürgen R. Reichenbach. Clinical applications of neuroimaging with susceptibility-weighted imaging. *Journal of Magnetic Resonance Imaging*, 22(4):439–450, 2005.

[7] Valentina Brainovich, Umberto Sabatini, and Gisela E. Hagberg. Advantages of using multiple-echo image combination and asymmetric triangular phase masking in magnetic resonance venography at 3T. *Magnetic Resonance Imaging*, 27(1):23–37, 2009.

[8] Marc Hermier and Norbert Nighoghossian. Contribution of susceptibility-weighted imaging to acute stroke assessment. *Stroke*, 35(8):1989–1994, 2004.

[9] Hao-Li Liu, Yau-Yau Wai, Wen-Shiang Chen, Jin-Chung Chen, Po-Hong Hsu, Xin-Yu Wu, Wen-Cheng Huang, Tzu-Chen Yen, and Jiun-Jie Wang. Hemorrhage detection during focused-ultrasound induced blood-brain-barrier opening by using susceptibility-weighted magnetic resonance imaging. *Ultrasound Med Biol*, 34(4):598–606, 2008.

[10] Andreas Deistung, Hans-Joachim Mentzel, Alexander Rauscher, Stephan Witoszynskyj, Werner A Kaiser, and Jürgen R Reichenbach. Demonstration of paramagnetic and diamagnetic cerebral lesions by using susceptibility weighted phase imaging (SWI). *Z Med Phys*, 16(4):261–7, 2006.

[11] Peter Koopmans, Rashindra Manniesing, Wiro Niessen, Max Viergever, and Markus Barth. MR venography of the human brain using susceptibility weighted imaging at very high field strength. *Magnetic Resonance Materials in Physics, Biology and Medicine*, 21(1):149–158, 2008.

[12] Amir M. Abduljalil, Petra Schmalbrock, Vera Novak, and Donald W. Chakeres. Enhanced gray and white matter contrast of phase susceptibility-weighted images in ultra-high-field magnetic resonance imaging. *Journal of Magnetic Resonance Imaging*, 18(3):284–290, 2003.

[13] Zhaolin Chen, Leigh A. Johnston, Dae Hyuk Kwon, Se Hong Oh, Zang-Hee Cho, and Gary F. Egan. An optimised framework for reconstructing and processing MR phase images. *NeuroImage*, 49(2):1289–1300, January 2010.

7

DIFFUSION-GUIDED QUANTITATIVE SUSCEPTIBILITY MAPPING

In recent years, there has been an increased interest in the area of quantitative susceptibility mapping (QSM). Magnetic susceptibility is a unit-less constant which describes the rate at which magnetisation occurs in matter, such as biological tissue, in response to an applied magnetic field. This magnetisation presents as perturbations in the B field which are proportional to phase intensities in MR phase data. Having reliable estimates of susceptibility can help in the analysis of the chemical composition of tissues. In particular, the ability to quantify iron content is of clinical importance, as changes in iron deposition within specific areas of the brain are known to be biomarkers of neurodegenerative diseases, such as Freidrich's Ataxia, Alzheimer's and Parkinson's diseases [1, 2].

7.1 BACKGROUND AND THEORY

Beginning in the 1980s, attempts have been made to quantify susceptibility from MRI data. Contrast in phase images were shown to be related to susceptibility differences associated with large abnormal pathologies, such as haematomas and tumours [3, 4, 5]. During the 1990s, methods such as finite elements and Fourier-based convolution were used to model the observed magnetic B field perturbations induced by arbitrarily-shaped objects of uniform susceptibility [6, 7, 8, 9, 10] and arbitrary susceptibility distributions [11, 12, 13, 14]. In 2004, Li and Leigh [15] demonstrated that the inverse could be achieved, where an arbitrary susceptibility distribution could be estimated from known B field perturbation data by solving a large linear system using a singular value decomposition method. However, the scaling of the method was limited due to exponential increase in computation and memory requirements.

Advances in high field MR technology have led to increased phase contrast [16], from which field perturbation maps with intricate structural detail can be calculated. With this increase contrast, spherical model-based susceptibility derivation has prevailed. Several approaches to the problem have been proposed: thresholded k-space kernel methods [17, 18, 19], calculation of susceptibility through multiple orientation sampling (COSMOS) [20] and regularisation-based methods [21, 22, 23, 24].

The primary reason for the variety of approaches to the QSM problem is the ill-posed nature of the inverse of the linear system:

$$\Delta B\left(\boldsymbol{r}\right) = \Delta\chi\left(\boldsymbol{r}\right) \otimes F_S\left(\boldsymbol{r}\right) \tag{7.1}$$

where $\Delta B\left(\boldsymbol{r}\right)$ is the change in B field at voxel $\boldsymbol{r}$ (the field map), $\Delta\chi$ is the change in susceptibility and F_S is the spherical model kernel based on the change in B induced by a sphere. The Fourier-based convolution QSM methods [17, 18, 19, 20, 21, 22, 23, 24] employ the convolution theorem to reduce the computational expense of the problem:

$$\Delta B\left(\boldsymbol{r}\right) = \mathrm{FT}^{-1}\left(\widetilde{\Delta\chi}\left(\boldsymbol{k}\right) \cdot \widetilde{F_S}\left(\boldsymbol{k}\right)\right) \tag{7.2}$$

where $\widetilde{X}$ denotes the Fourier transform of the function X, FT^{-1} is the inverse Fourier transform and $\cdot$ represents voxel-wise multiplication. The Fourier transform of $F_S\left(\boldsymbol{r}\right)$ is commonly applied using the continuous Fourier transform, giving

$$\widetilde{F_S}\left(\boldsymbol{k}\right) = \frac{1}{3} - \frac{k_z^2}{k_x^2 + k_y^2 + k_z^2} \tag{7.3}$$

where $\boldsymbol{k} = \left(k_x, k_y, k_z\right)$ are cartesian coordinates in the Fourier domain. In 3D k-space, there exists two cones where $\widetilde{F_S}\left(\boldsymbol{k}\right) = 0$, defined when $\frac{k_z^2}{k_x^2+k_y^2+k_z^2} = \frac{1}{3}$ (Fig. 32). From (7.2), one can see that where $\widetilde{F_S}\left(\boldsymbol{k}\right) = 0$, the value $\widetilde{\Delta\chi}\left(\boldsymbol{k}\right)$ can take on any value without affecting $\Delta B\left(\boldsymbol{r}\right)$. As such, there are an infinite number of solutions to (7.2) and thus the linear system is ill-posed.

The data, ΔB, and the estimated susceptibility map, $\Delta\chi$, are discretised representations of real world values. To compute the voxel-wise multiplication in (7.2), $\widetilde{F_S}\left(\boldsymbol{k}\right)$ is discretised by evaluation at the $\boldsymbol{k}$ coordinates that correspond to the array representation of $\widetilde{\Delta\chi}$. Implicit in this is the assumption that either the discretised continuous Fourier transform of $F_S\left(\boldsymbol{r}\right)$ approximates the discrete Fourier transform of $F_S\left(\boldsymbol{r}\right)$, or that $\widetilde{\Delta\chi}\left(\boldsymbol{k}\right)$ is the discretised continuous Fourier transform of $\Delta\chi\left(\boldsymbol{r}\right)$ and the inverse discrete Fourier transform correctly inverts a continuous Fourier transform. Analytically, this holds true as the array dimensions approach infinity. However, QSM is a computational method and thus the array dimensions never approach infinity. As such, error is introduced by this mismatch of Fourier transforms, which could affect results, given the ill-posed nature of the system.

The thresholded k-space division (TKD) method [17] seeks to overcome the ill-posed nature of the system by placing a minimum threshold on $\left|\widetilde{F_S}\left(\boldsymbol{k}\right)\right|$. Any

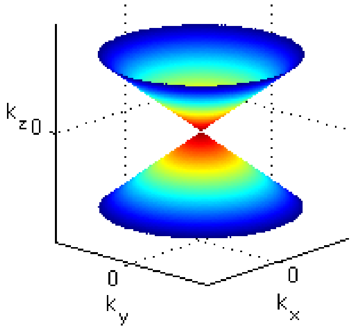

Figure 32: Zero cones in k-space spherical model kernel.

absolute value below this threshold is set to the threshold value. Eq. (7.2) is then rearranged into a division,

$$\Delta\chi\left(\boldsymbol{r}\right) = \mathrm{DFT}^{-1}\left(\frac{\widetilde{\Delta B}\left(\boldsymbol{k}\right)}{\widetilde{F}_{S,thr}\left(\boldsymbol{k}\right)}\right), \tag{7.4}$$

using the thresholded k-space kernel, $\widetilde{F}_{S,thr}\left(\boldsymbol{k}\right)$. DFT^{-1} refers to the inverse discrete fourier transform. This method has a demonstrated ability to resolve susceptibility values from field maps. However the susceptibility values are sensitive to the threshold and the maps are often marked by cross-shaped artefacts [17]. A similar method sets $\widetilde{\Delta B}\left(\boldsymbol{k}\right) = 0$, at points where $\left|\widetilde{F}_S\left(\boldsymbol{k}\right)\right|$ is below a threshold [19]. The results also demonstrated cross-shaped artefacts when applied to a dataset acquired at a single orientation. Li et al [18] proposed a thresholded k-space method where the approximate first-order derivative of (7.1),

$$\widetilde{\Delta B}\left(\boldsymbol{k}\right) + \frac{2\left(k_x^2 + k_y^2\right)k_z}{\left(k_x^2 + k_y^2 + k_z^2\right)^2} \cdot \widetilde{\Delta\chi}\left(\boldsymbol{k}\right) \approx 0, \tag{7.5}$$

is applied when $\left|\widetilde{F}_S\left(\boldsymbol{k}\right)\right|$ falls below the threshold. This method demonstrated marked improvement in avoiding the cross-shaped artefacts apparent in the thresholded method. However, it was also noted that the derived susceptibility values in white matter were highly dependent on the orientation of the white matter microstructure relative to the main B field direction.

An alternative to thresholding is to define a cost function based on the linear system and solve for $\Delta\chi$ by minimising the cost. The cost function involves a regularisation term, such as the L_1 or L_2-norm of $\Delta\chi$ [21]. The Morphology Enabled Dipole Inversion (MEDI) method [22, 23] employs a regularisation term that adds a penalty to high gradients in the susceptibility map where the gradient in the magnitude is low. The cost function, formulated in matrix-vector representation, is

$$\lambda \left\|\mathbf{W}_0\left(\Delta\mathbf{B} - \mathbf{F}_{DS}\Delta\boldsymbol{\varnothing}\right)\right\|_2^2 + \left\|\mathbf{W}_1\nabla\left(\Delta\boldsymbol{\varnothing}\right)\right\|_1 \tag{7.6}$$

where $\|\cdot\|_1$ is the L_1-norm, $\|\cdot\|_2$ is the L_2-norm, $\mathbf{W}_0$ and $\mathbf{W}_1$ are weighting matrices, ∇ is the gradient operator and $\mathbf{F}_{DS}$ is the matrix representation of the convolution with F_S. Although the notation is in matrix form, $\mathbf{F}_{DS}$ is computed by employing the convolution theorem with the continuous Fourier transform of F_S. λ is a parameter that controls the cost of the regularisation term $\left\|\mathbf{W}_1\nabla\left(\Delta\boldsymbol{\varnothing}\right)\right\|_1$ relative to $\left\|\mathbf{W}_0\left(\Delta\mathbf{B} - \mathbf{F}_{DS}\Delta\boldsymbol{\varnothing}\right)\right\|_2^2$. $\mathbf{W}_0$ is defined as a diagonal matrix corresponding to a binary mask such that

$$\mathbf{W}_0 = \begin{cases} 0, & \text{for a background voxel where } \Delta\chi \text{ is known to be zero} \\ 1, & \text{for a foreground voxel.} \end{cases} \tag{7.7}$$

$\mathbf{W}_1$ is defined as a diagonal matrix corresponding to a binary mask such that

$$\mathbf{W}_1 = \begin{cases} 0, & |\nabla\rho| > 5\sigma_{BG} \\ 1, & \text{otherwise} \end{cases} \tag{7.8}$$

where ρ is the MR magnitude data, $|\nabla\rho|$ is the magnitude of the gradient of ρ and σ_{BG} is the standard deviation of the background noise in ρ.

Eq. (7.6) is minimised for a range of λ values, and the chosen solution is that which corresponds to

$$\left\|\mathbf{W}_0\left(\Delta\mathbf{B} - \mathbf{F}_{DS}\Delta\boldsymbol{\varnothing}\right)\right\|_2^2 \approx \varepsilon \tag{7.9}$$

where ε is less than the expected noise level. When λ is too low, the system becomes under-regularised and cross-shaped artefacts appear in the susceptibility maps. When λ is too high, the system becomes over-regularised and the susceptibility maps are over-smoothed [22].

The current gold standard method is the COSMOS method [20]. It requires three field maps where the object being imaged is oriented at three different angles to the main B field direction. By including the information from the three acquisitions, the linear system becomes over-determined. Theoretically, the angles that produce the most accurate susceptibility map are 0°, 60° and 120° [20]. These angles are impractical for human scanning when imaging the head. However, smaller angles of $< 50°$ for back-front rotation and $< 34°$ for left-right rotation have been achieved [24]. The COSMOS susceptibility maps do not suffer from the cross-shaped artefacts and have demonstrated relatively accurate susceptibility values on a gadolinium phantom.

All the methods described are based on a spherical model of the effects of susceptibility on the B field. He and Yablonskiy [25] have demonstrated, however, that white matter does not conform to the spherical assumption and a cylindrical model is more appropriate. Structurally, white matter consists of bundles of the myelinated axons of neurons, long thin fibres that are intuitively better characterised as cylinders than spheres. He and Yablonskiy considered the cylindrical nature of white matter at the nanometre-scale, suggesting that incorporating a cylindrical Lorentz cavity rather than the spherical Lorentz cavity into the formulation of (7.3) would better explain the observed frequency differences between white matter and grey matter. Lee et al [26] further investigated the susceptibility effects of white matter and concluded that anisotropic susceptibility is a more appropriate model for the observed field perturbations. Recent research into the effects of white matter microstructure on T_2^* relaxation support these findings, where the orientation of white matter fibres to the main field were found to affect phase and R_2^* $(= 1/T_2^*)$ [27, 28, 29]. These later findings, and the method proposed in this chapter, consider the cylindrical effects on the micro- and millimetre scale.

To address the shortcomings of the spherical kernel in modelling the susceptibility effects of white matter, we investigated the feasibility of a single acquisition method that employs both the spherical and cylindrical models of susceptibility effects. We present a proof-of-principle method that uses diffusion weighted imaging to determine the direction of white matter fibres, applying the cylindrical model to identified white matter voxels and the spherical model to all other voxels. Since the method employs multiple kernels, the linear system is no longer a convolution and must therefore be solved in the spatial domain. The memory and computational requirements associated with this approach presents an additional challenge which we address using high performance computing and algorithmic techniques.

7.2 METHOD

7.2.1 *Diffusion-guided quantitative susceptibility mapping*

In our proposed method, we remove the assumption that the spherical model is suitable for all voxels and apply a mix of cylindrical models with varying orientations and the spherical model depending on the voxel tissue class. We can therefore no longer apply the convolution theorem and solving for susceptibility must be achieved in the spatial domain. The spatial domain problem is presented as a large linear system

$$\mathbf{Ax} = \mathbf{b} \tag{7.10}$$

where **A** represents the superposition of the changes in flux density induced by voxel-sized spheres and cylinders. Vectors **x** and **b** represent the susceptibility map, $\Delta\chi$, and field map, ΔB, respectively. Voxel positions in the data matrix are enumerated such that each row in **x** and **b** has a one-to-one correspondence with a voxel position. The element $\mathbf{A}_{m,n}$, at row m and column n of **A**, describes the effects on voxel m induced by a cylinder or sphere at voxel n.

Diffusion weighted imaging (DWI) is an MRI technique that exploits the thermal motion, or diffusion, of water molecules to affect the contrast in acquired images. In biological tissues, H^1 nuclei are primarily bound within water molecules. The diffusion of these molecules is restricted by their microstructural environment, such as the axons of the neurons of which white matter is comprised. By applying linear field gradients to cause dephasing and rephasing along a specific direction, we can measure the amount of diffusion between the dephase and rephase along that direction. Repeating this for multiple different directions provides the data to calculate a tensor model of the diffusion characteristics at each voxel, known as diffusion tensors.

The diffusion tensors provide information on the most suitable susceptibility model (spherical or cylindrical) for each voxel. Tensor-based fractional anisotropy (FA) measures indicate how uni-directional the diffusion is, where high FA corresponds to diffusion occurring along a single direction and low FA corresponds to diffusion occurring equally in all directions. We therefore chose a threshold, T_{FA}, such that voxels with an FA value below the threshold are modelled as spheres of volume equal to the volume of the voxel, while all other voxels are modelled as segments of infinitely long cylinders. The primary eigenvectors, V1, of the tensors define the directions for the cylinder axes. The elements of **A** are therefore given by

$$\mathbf{A}_{m,n} = \begin{cases} F_s\left(\boldsymbol{r}_m - \boldsymbol{r}_n\right), & \text{if } \mathrm{FA}\left(n\right) < T_{\mathrm{FA}} \\ F_c\left(\boldsymbol{r}_m - \boldsymbol{r}_n\right), & \text{if } \mathrm{FA}(n) \geq T_{\mathrm{FA}} \end{cases} \tag{7.11}$$

where $\boldsymbol{r}_m$ and $\boldsymbol{r}_n$ are the position vectors of voxels m and n, respectively. F_s is the spherical model kernel defined in image space,

$$F_s\left(\boldsymbol{r}\right) = \begin{cases} \frac{B_0}{4\pi}\left(\frac{3\cos^2\theta - 1}{r^3}\right), & r > 0 \\ 0, & r = 0 \end{cases} \tag{7.12}$$

where r is the length of vector $\boldsymbol{r}$, and F_c is the cylindrical kernel defined in image space,

$$F_c\left(\boldsymbol{r}\right) = \begin{cases} \frac{B_0}{6}\left(3\cos^2\beta - 1\right), & r = 0 \\ P\left(\boldsymbol{r}\right)\frac{1}{2\pi}B_0\frac{1}{\left|\boldsymbol{r}-\left(\boldsymbol{r}\cdot\hat{\boldsymbol{c}}\right)\hat{\boldsymbol{c}}\right|^2}\sin^2\beta\left(2\left(\frac{\boldsymbol{r}\cdot\hat{\boldsymbol{b}}-\left(\boldsymbol{r}\cdot\hat{\boldsymbol{c}}\right)\left(\hat{\boldsymbol{b}}\cdot\hat{\boldsymbol{c}}\right)}{\left|\boldsymbol{r}-\left(\boldsymbol{r}\cdot\hat{\boldsymbol{c}}\right)\hat{\boldsymbol{c}}\right|\left|\hat{\boldsymbol{b}}-\left(\hat{\boldsymbol{b}}\cdot\hat{\boldsymbol{c}}\right)\hat{\boldsymbol{c}}\right|}\right)^2 - 1\right), & \text{otherwise,} \end{cases} \tag{7.13}$$

where β is the angle between the cylinder axis, $\hat{\boldsymbol{c}}$, and the direction of the main B field, $\hat{\boldsymbol{b}}$ (full derivation of these functions are in the Appendix). We introduce a proportionality function, $P\left(\boldsymbol{r}\right)$, to facilitate discretisation of the analytical 2D cylindrical kernel. It is defined as

$$P\left(\boldsymbol{r}\right) = \frac{\left(2\alpha - \boldsymbol{r}\cdot\hat{\boldsymbol{c}}\right)^2\left(\alpha + \boldsymbol{r}\cdot\hat{\boldsymbol{c}}\right)}{4\alpha^3} \tag{7.14}$$

where $\alpha = 0.47$ provides the optimal discretisation of the kernel (see Appendix).

A is a square matrix where the number of rows and columns is determined by the number of voxels in the data. For typical images, the number of voxels is in the range of 1 to 10 million, resulting in a matrix of the order of 10^{12} elements. Hence, finding the solution **x**, given **A** and **b**, requires numerical and algorithmic techniques to minimise the error in the result.

We use the Landweber algorithm [30] to solve the linear system in (7.10). It is an iterative method given by

$$\mathbf{x}_{n+1} = \mathbf{x}_n - \tau\mathbf{A}'\left(\mathbf{A}\mathbf{x}_n - \mathbf{b}\right) \tag{7.15}$$

where $\mathbf{x}_n$ denotes the value of x at the nth iteration, τ is the step size and $\mathbf{A}'$ denotes the transpose of **A**. All elements of $\mathbf{x}_0$ are initialised to zero. For (7.15) to converge, we need

$$0 < \tau < \frac{2}{\max\lambda_{\mathbf{A}'\mathbf{A}}} \tag{7.16}$$

where $\max\lambda_{\mathbf{A}'\mathbf{A}}$ is the largest eigenvalue of $\mathbf{A}'\mathbf{A}$ [31]. As τ approaches $\frac{2}{\max\lambda_{\mathbf{A}'\mathbf{A}}}$, Eq. (7.15) converges faster. However, explicitly calculating $\frac{2}{\max\lambda_{\mathbf{A}'\mathbf{A}}}$ is computationally expensive. Instead, a value of $\tau = 0.15$ is applied, which was heuristically determined to be adequate using small scale simulations. The Landweber algorithm does not require explicit formation of matrix **A**, which could be prohibitively large, even for a supercomputer. Instead, the element-by-element multiplications involved in $\mathbf{A}\mathbf{x}_n$ and $\mathbf{A}'\mathbf{y}$, where $\mathbf{y} = \mathbf{A}\mathbf{x}_n - \mathbf{b}$, are computed by calculating the elements of **A** immediately before being required for computations, thereby avoiding the need to store the values in memory.

We regularise the system in (7.10) using a second order derivative, the Laplacian operator. While regularisation using a first order derivative will favour uniform intensities, the Laplacian operator favours uniform gradients. It is therefore more effective in edge preservation and does not make assumptions about the uniformity in the susceptibility map relative to the magnitude data [23]. The regularisation is incorporated into (7.15) as follows

$$\mathbf{x}_{n+1} = \mathbf{x}_n - \tau\left(\kappa\mathbf{A}'\left(\mathbf{A}\mathbf{x}_n - \mathbf{b}\right) + (1-\kappa)\,\mathbf{L}'\mathbf{L}\mathbf{x}_n\right) \tag{7.17}$$

where $\mathbf{L}$ is the matrix representing the convolution of a $3 \times 3 \times 3$ Laplacian operator defined as

$$L(x,y) = \left[\begin{bmatrix} 0 & 3/96 & 0 \\ 3/96 & 10/96 & 3/96 \\ 0 & 3/96 & 0 \end{bmatrix} \begin{bmatrix} 3/96 & 10/96 & 3/96 \\ 10/96 & -1 & 10/96 \\ 3/96 & 10/96 & 3/96 \end{bmatrix} \begin{bmatrix} 0 & 3/96 & 0 \\ 3/96 & 10/96 & 3/96 \\ 0 & 3/96 & 0 \end{bmatrix}\right] \tag{7.18}$$

The weighting parameter $0 \leq \kappa \leq 1$ determines the relative costs associated with the regularisation term.

Outside of the object, the total susceptibility is assumed to be uniform with $\Delta\chi = 0$. This is a result of the removal of low frequency fluctuations during the pre-processing of the phase data. Enforcing a $x_n \equiv \Delta\chi(\boldsymbol{r}_n) = 0$ solution in vector $\mathbf{x}$ is achieved by eliminating the corresponding elements from the vector $\mathbf{x}$ and corresponding columns from the matrix $\mathbf{A}$. This has the advantage of reducing the computations required to solve (7.10).

We will refer to this method as Diffusion-Guided Quantitative Susceptibility Mapping (dQSM).

7.2.2 *Computation and method comparison*

Solving the linear system in Eq. (7.10) is computationally expensive and requires the use of a supercomputer to produce results in a feasible computation time. The computations were executed on an IBM BlueGene/Q, using 4096 processors with an allocation of 4TB of RAM. dQSM was applied to three numerical phantoms and a mouse dataset described in section 7.2.3. The same algorithm was also applied using only the spherical model kernel to observe the effects of the inclusion of the cylindrical model while excluding the effects produced by the different cost functions, (7.17) and (7.6), the use of the Fast Fourier Transform algorithm, and the use of the continuous Fourier transform (as opposed to the discrete Fourier transform) of the spherical model kernel. We will refer to this as Spherical Model Quantitative Susceptibility Mapping (sQSM). Due to limitations in time allocation on the BlueGene/Q, sQSM was only applied to the numerical phantom with zero noise and the mouse dataset.

The less computationally intensive MEDI calculations were performed on an Apple Macbook Pro with an Intel Core i7 dual core (2.7 GHz) CPU and 8GB of

	MEDI	sQSM	dQSM
Voxel modelling	spherical	spherical	spherical and cylindrical
Numerical convolution calculation	convolution theorem (Fourier transforms)	explicit calculation in image space	explicit calculation in image space
Convolution kernel	discretised continuous fourier transform in k-space	discretise image space	discretise image space
Regularisation	L1 norm of first order derivative	L2 norm of second order derivative	L2 norm of second order derivative

Table 5: Methodological differences between MEDI, sQSM and dQSM.

RAM. The MEDI method was applied to the three numerical phantoms and the mouse dataset. A comparison of methodological differences between MEDI, sQSM and dQSM is summarised in Table 5.

Quantitative noise and mean susceptibility comparisons were performed on the resultant images. Comparison of the voxels within the cylinders and spheres was conducted using signal-to-noise ratio (SNR) measurements. Since susceptibility maps contain both negative and non-negative numbers, the SNR was defined as

$$\mathrm{SNR} = \frac{\mathrm{RMS}}{\sigma}. \tag{7.19}$$

where RMS is the root mean square of the $\Delta\chi$ voxel intensities and σ is the standard deviation of the noise. The SNR of the $\Delta\chi = 0$ voxels, that is, the voxels outside of the cylinders and spheres, is considered an unreliable measure, as the ideal $\Delta\chi$ signal of zero would result in zero SNR regardless of the noise. For these voxels, we compared the standard deviation of noise instead of SNR. Noise is traditionally calculated in MR contexts by evaluating the standard deviation in background (air) regions outside the imaged object. However, the results demonstrated spatially large inhomogeneities. To separate these from the noise, high pass filtering was performed before the standard deviation of the background voxels was calculated.

7.2.3 *Data simulation, acquisition and phase processing*

Numerical phantom data

Numerical phantoms with known susceptibilities were created. The dimensions of the phantom datasets were $50 \times 140 \times 80$ voxels. Each dataset contained four cylinders and four spheres with susceptibilities of 1×10^{-7}, 2×10^{-7}, 3×10^{-7} and 4×10^{-7}. The main magnetic field was chosen to be along the z-direction and of strength $B_0 = 4.7\mathrm{T}$. The cylinders were oriented along the x-axis and therefore perpendicular to the main magnetic field. The radius of the cylinders and spheres were 5 voxels. The ΔB map was created by superimposing individual ΔB maps for each cylinder and each sphere. To calculate the individual ΔB maps, a true susceptibility map of dimensions $50 \times 140 \times 80$ was created with a single cylinder or sphere positioned in the equivalent position of the multiple cylinder/sphere ΔB map. The voxel-wise susceptibility values were calculated such that

$$\Delta\chi = \begin{cases} \Delta\chi_{\mathrm{Cyl/Sph}}, & \text{voxel completely enclosed in cylinder/sphere} \\ 0, & \text{voxel completely outside cylinder/sphere} \\ \Delta\chi A_{in}, & \text{voxel straddles the boundary of the cylinder/sphere} \end{cases} \tag{7.20}$$

where A_{in} is the proportion of the voxel area inside the cylinder/sphere. The individual ΔB maps were calculated by convolving the susceptibility map with the spherical or cylindrical model kernel. In order to compare the robustness of the methods to noise, three versions of the dataset were created with noise standard deviations of 0, 0.05 and 0.10 radians.

The V1 map was created using the cylinder axis $(1, 0, 0)$ for the cylinder voxels, and zeros $(0, 0, 0)$ otherwise. The FA map was 1 for cylinder voxels and 0 otherwise. The binary foreground/background mask was set such that the outermost voxels of the dataset were defined as background and all internal voxels defined as foreground.

To simulate a magnitude image, $m(\mathbf{r})$ (used in the MEDI method) we used a normalised true susceptibility map to compute $\mathbf{W}_1$ in (7.6). The normalisation was calculated such that

$$m(\boldsymbol{r}) = \begin{cases} 0, & \Delta\chi_{\mathrm{true}}(\boldsymbol{r}) < \mu - 2\sigma \\ \frac{\Delta\chi_{\mathrm{true}}(\boldsymbol{r}) - (\mu - 2\sigma)}{4\sigma}, & \mu - 2\sigma \leq \Delta\chi_{\mathrm{true}}(\boldsymbol{r}) \\ & \leq \mu + 2\sigma \\ 1, & \Delta\chi_{\mathrm{true}}(\boldsymbol{r}) > \mu + 2\sigma \end{cases} \tag{7.21}$$

where $\Delta\chi_{\mathrm{true}}$ is the true susceptibility intensity and μ and σ are the mean and standard deviation, respectively, of $\Delta\chi_{\mathrm{true}}$. The weighting matrix $\mathbf{W}_1$ was then defined as

$$\mathbf{W}_1 = \begin{cases} 1, & |\nabla m(\boldsymbol{r})| = 0 \\ 0, & \text{otherwise} \end{cases} \tag{7.22}$$

where ∇ is the gradient operator.

For dQSM and sQSM processing, a value of $\kappa = 0.75$ was used.

MEDI was also applied for comparison. To create the matrix $\mathbf{W}_0$ in (7.7), we used the true susceptibility distribution in place of the magnitude, ρ. The value $\lambda = 1$ was determined to be the optimal value as it was the highest λ that resulted in an image displaying no cross-shaped artefacts.

Experimental mouse brain data

Fixed mouse brain MRI data was acquired on a 4.7T Bruker with Avance III electronics and BGA12S-HP gradient set with a maximum gradient strength of 660mT/m. A 2 channel cryogenically cooled surface coil was used for transmit and receive. T_2^*-weighted imaging and diffusion weighted imaging (DWI) data were acquired with identical matrix sizes of 192 × 128 × 96 and resolutions of 100 × 100 × 100 μm^3.

The T_2^* data was acquired using a 3D EPI sequence with TR=1000ms, TE=100ms and flip angle = 30°. The data was reconstructed using the complex SENSE reconstruction method [32]. FSL Brain Extraction Tool was used to create a mask with manual correction. The phase data was unwrapped using FSL Prelude in 3D mode and using the mask. The unwrapped phase data was then filtered using the Spatially Dependent Filtering method of Chapter 4 and [33]. The field map was calculated from the filtered phase data, $\phi(\mathbf{r})$, using the relationship

$$\Delta B(\boldsymbol{r}) = \frac{-\phi(\boldsymbol{r})}{\gamma \mathrm{TE}}. \tag{7.23}$$

The DWI data was acquired using an EPI-DWI sequence with TR = 2500ms, TE = 65ms, shots = 2, δ = 3ms, Δ = 14ms, 46 directions, 4 B0 images and b-value=1700 s/mm^2. The total scan time was 6 hours 40 mins. The data was reconstructed using a complex SENSE reconstruction method. The reconstructed DWI data was then processed using the FSL tool DTIFIT [34] to return the single tensor estimates.

The image volume size was further reduced to 145 × 114 × 70 by eliminating axial, sagittal and coronal slices that did not contain brain voxels. For dQSM, a FA threshold of 0.2 was determined based on visual inspection of the FA and V1 data. FSL FLIRT was used to register a B0 image with the T_2^* image. The calculated affine transformation was then used to register the FA and V1 maps to the T_2^* map.

For dQSM and sQSM processing, a value of $\kappa = 0.25$ was used.

For MEDI the same criteria for determining λ as was used for the numerical phantom. A value of $\lambda = 0.02$ was determined to be optimal.

7.3 RESULTS

7.3.1 *Comparison of spherical and cylindrical kernels*

The accuracy of the spherical and cylindrical kernels at estimating the change in B field was confirmed using numerical computations. A susceptibility map for a cylinder of water in a vacuum was created. The susceptibility map was convolved with the spherical and cylindrical kernels and compared to theoretical values for the change in B field (Fig. 33). As the length of the cylinder in the susceptibility map increases, the error in the computed estimates decreases (Fig. 34). The error in the spherical kernel-derived ΔB map is greater than in the cylindrical kernel-derived ΔB map for the calculated ratios and appears to asymptote towards the error of the cylindrical kernel-derived ΔB map. Since data used in dQSM is discrete and finite in dimensions, it is reasonable to assume that the cylindrical kernel will provide more accurate results than the spherical kernel regardless of the radius or length of the cylindrical structures.

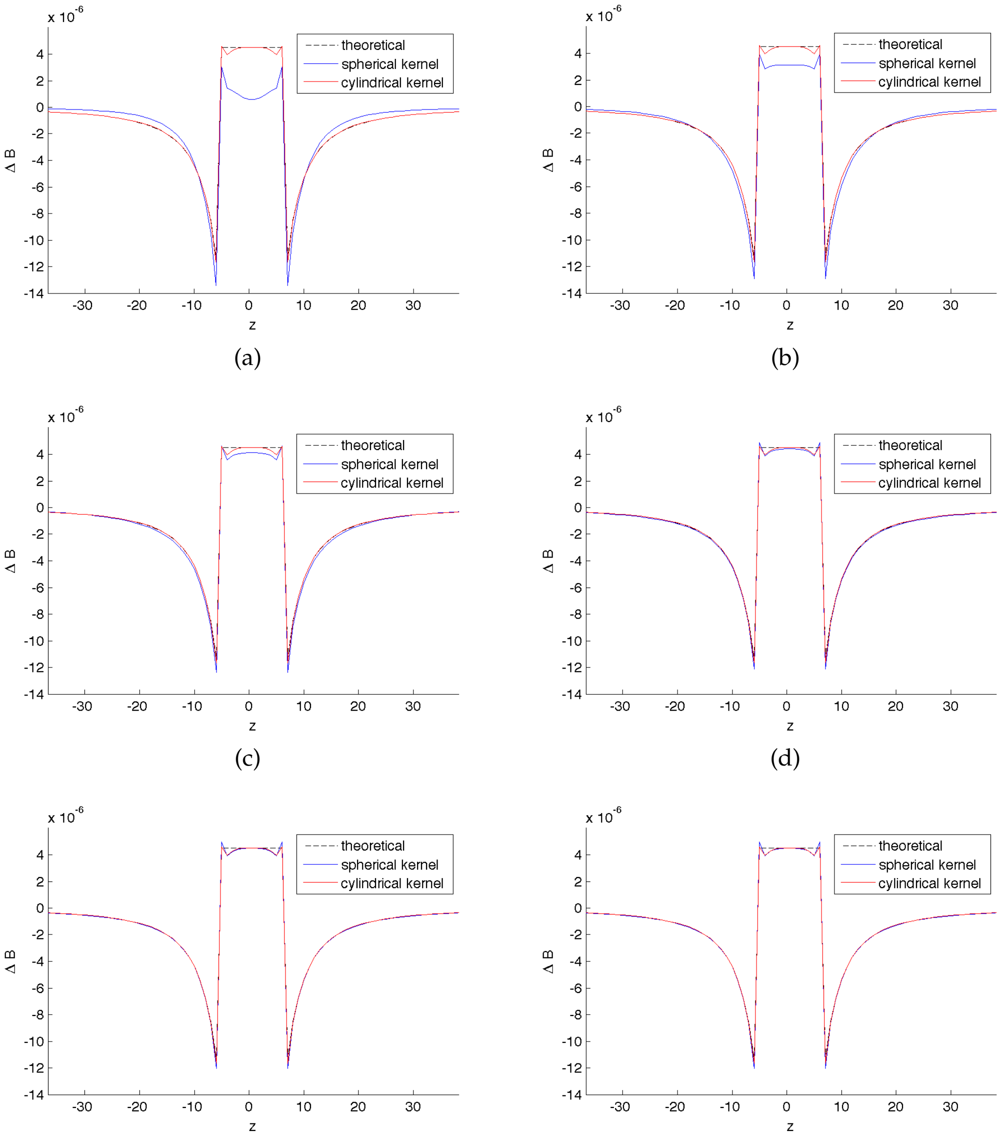

(a) (b)

(c) (d)

(e) (f)

Figure 33: Cross-sectional profile of change in B field along z direction due to an infinitely long cylinder. Theoretical values are compared to values computed by convolving spherical and cylindrical kernels with the susceptibility map where the ratio of length to radius of the cylinder in the susceptibility map is (a-f) 2, 4, 8, 16, 32 and 64.

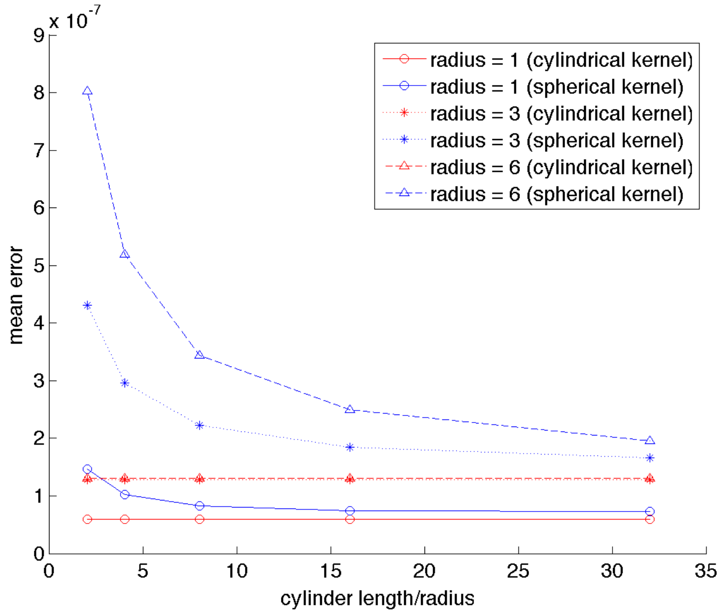

Figure 34: Cylinder length/radius ratio effects on mean error in the spherical and cylindrical kernel derived change in B field maps.

7.3.2 *Numerical Phantom Results*

The zero noise numerical phantom comprised a true susceptibility map (Fig. 35a) and the derived ΔB map (Fig. 35b). The estimated susceptibility maps exhibited obvious artefacts for the methods employing only the spherical kernel. The MEDI method (Fig. 35c) produced large regions in the background voxels of low susceptibility relative to susceptibilities in the spheres and cylinders. The sQSM map (Fig. 35d) also demonstrated attenuated regions, but at different locations to those in the MEDI derived maps. The artefacts presented as hypointense areas in the lower portion of the cross-sectional image near the sphere; however, in the coaxial image, these artefacts appear to originate from the ends of the cylinders. The susceptibility map derived using dQSM exhibited much less artefact. Some artefact was apparent, also stemming from the ends of the cylinders, however the artefact was not as severe as for the other two methods.

MEDI demonstrated better noise reduction than dQSM (Fig. 36). The standard deviation of the background noise is comparable between the two methods for the numerical phantom results based on 0.05 radian noise (Fig. 37a). The discrepancy between the standard deviation of the visual appearance of noise is due to the intensity contrast range in the images. When the phase noise is doubled, the background noise in the MEDI map decreases while the noise in the dQSM map scales with the doubling of the noise in the phase (Fig. 37b). In the sphere and cylinder voxels, the SNR is higher in the MEDI maps when the phase noise is 0.05. In the maps derived from the phase with noise of 0.10, the SNR was lower in the MEDI

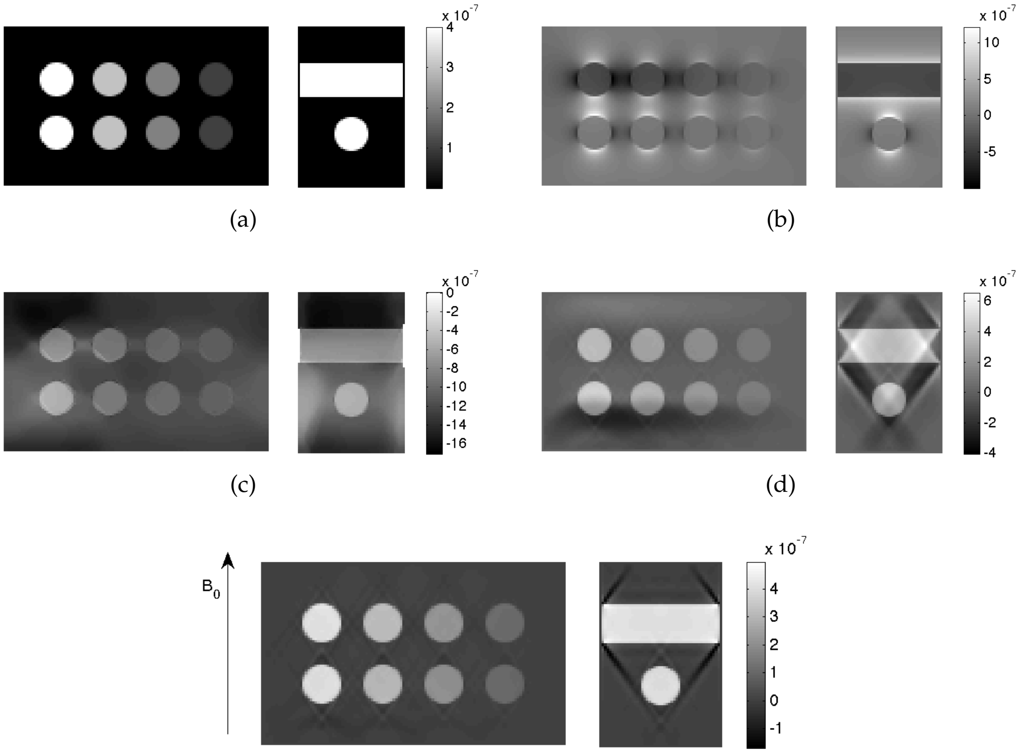

(a) (b) (c) (d) (e)

Figure 35: Susceptibility maps derived from a numerical phantom with zero noise, each showing (left) cross-sectional and (right) coaxial views. The (a) true susceptibility map was used to derive the (b) ΔB map. Susceptibility maps were then calculated using (c) MEDI ($\lambda' = 1$), (d) sQSM, and (e) dQSM. The top row objects in the images are cylinders, the bottom row are spheres. The true susceptibilities of the cylinders and spheres are, from left to right, $4e^{-7}$, $3e^{-7}$, $2e^{-7}$ and $1e^{-7}$.

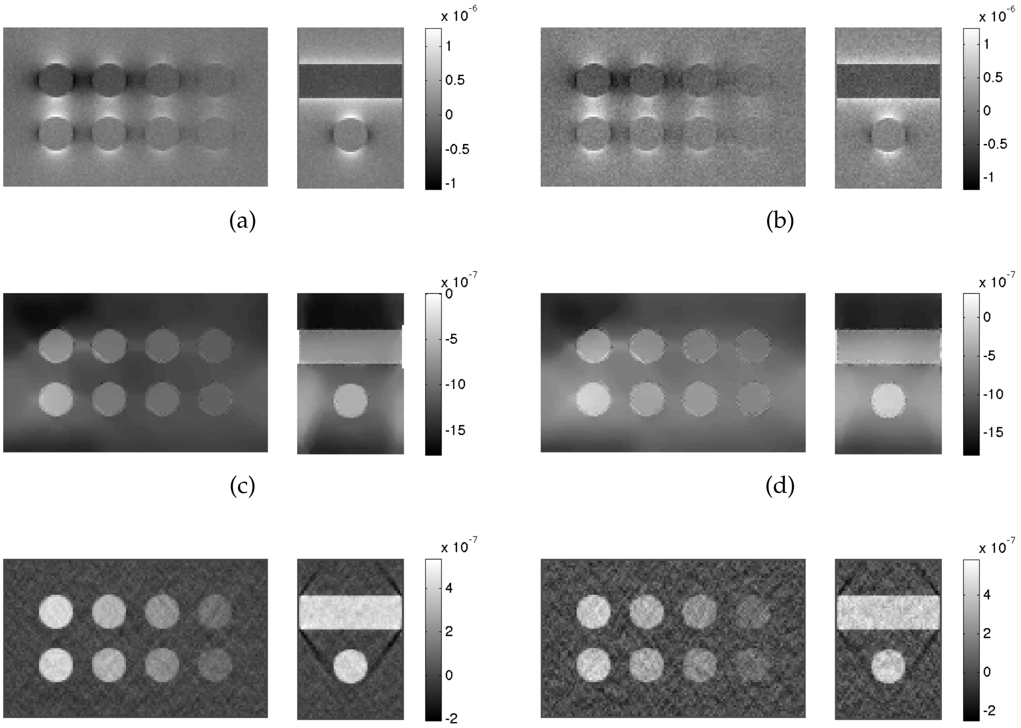

(a) (b)

(c) (d)

(e) (f)

Figure 36: Noise with standard deviations of (a,c,e) 0.05 radians and (b,d,f) 0.1 radians was added to a numerical phantom containing four cylinders (top row) and four spheres (bottom row) of susceptibility (left to right) 4e^{-7}, 3e^{-7}, 2e^{-7} and 1e^{-7}. Susceptibility maps were derived from (a,b) ΔB maps using (c,d) MEDI and (e,f) dQSM.

maps for the spheres, but higher in the cylinders. It was noted that the voxels on the edges of the spheres and cylinders which are not regularised by the MEDI method had very large noise characteristics.

Both dQSM and sQSM were significantly more accurate at calculating the susceptibility values compared to the MEDI method (Fig. 38). dQSM produced mean susceptibility values within 0.15×10^{-7} of the true value for the spheres and cylinders. In comparison, sQSM produced mean susceptibility values within 0.80×10^{-7} of the true value for the spheres and cylinders. The MEDI method was the least accurate, with susceptibility values 1.1×10^{-6} below that of the true value for the spheres and cylinders. While the increase in cylinder susceptibilities in the MEDI-derived maps correspond linearly to the increase in true susceptibility, the susceptibilities of the spheres do not have a linear correspondence.

The MEDI calculations took approximately 2 hours to run on a dual core 2.7GHz processor. In comparison, dQSM computations took between 169 and 275 minutes on a 4096 BlueGene/Q core allocation.

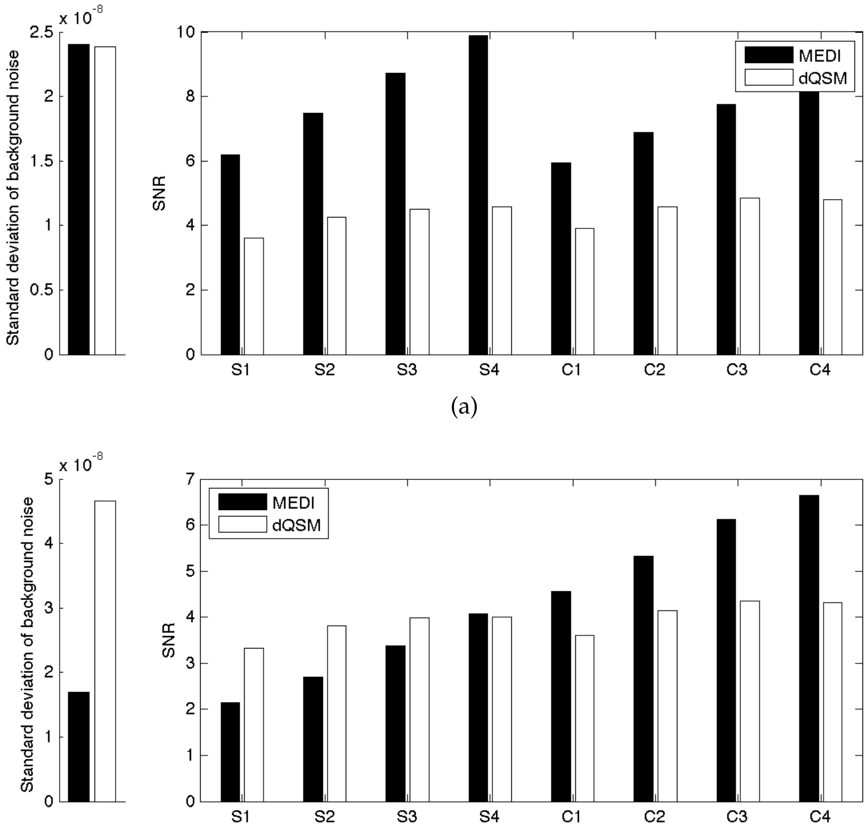

(a)

(b)

Figure 37: Noise characteristics of MEDI and dQSM results on numerical phantoms with (a) 0.05 and (b) 0.10 radians of phase noise. Noise in background voxels was evaluated using the standard deviation while noise in the foreground was evaluated using an SNR measure for voxels in the spheres (S1-4) and cylinders (C1-4) where susceptibilities are 4×10^{-7}, 3×10^{-7}, 2×10^{-7} and 1×10^{-7} respectively.

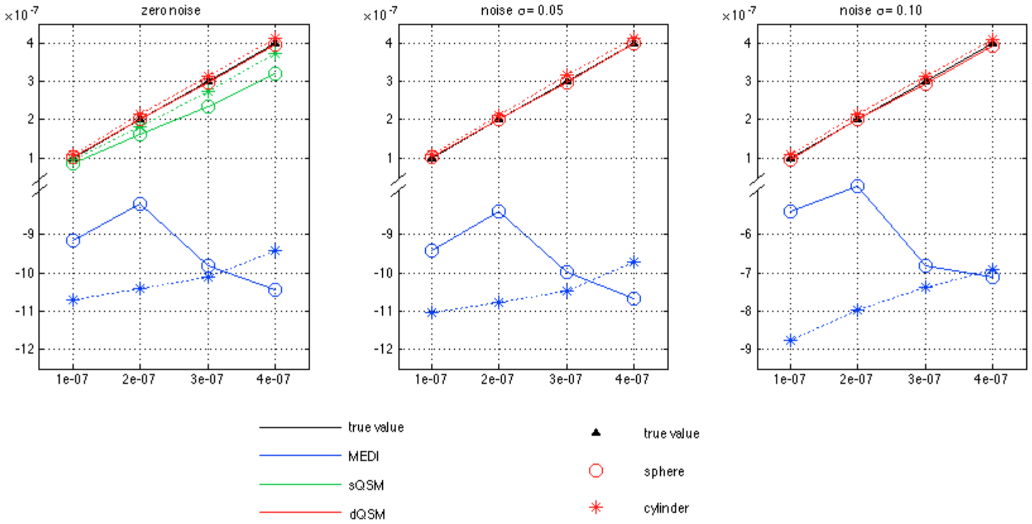

Figure 38: Comparison of estimated susceptibility values (y axis) inside the cylinders and spheres with true susceptibility value (x axis).

7.3.3 *Fixed mouse brain*

The MEDI method required a very low regularisation weighting parameter of $\lambda = 0.02$ to ensure artefacts were avoided in the susceptibility map (Fig. 39d). While this provided results with apparent structural contrast, the method was unable to resolve the dipole effects surrounding the white matter, as illustrated by the line profiles in Fig. 40.

The susceptibility maps derived using dQSM and sQSM presented with some artefacts. These methods were more successful than MEDI at resolving the white matter values, as can be seen in the line profiles (Fig. 40). sQSM produced large shadows (arrows, Fig 41e) that do not have corresponding structures in the magnitude image. These shadows are absent in the dQSM map (Fig. 41f). Susceptibility differences in the central region of the brain (rectangle, Fig. 41f) reflect structure seen in the magnitude image (rectangle, Fig. 41a). This structure does not appear in the maps derived only using the spherical model.

7.4 DISCUSSION

The susceptibility maps estimated from the numerical phantoms of cylinders and spheres demonstrated both the ability of each method to accurately determine the susceptibility of objects and the artefacts that remain in the maps. The methods employing just the spherical kernel (MEDI and sQSM) produced substantial artefacts in the derived susceptibility maps, attributed to the inaccuracy in applying a spherical model to cylindrical structures. This explanation is supported by the relatively minimal artefact in the dQSM maps. The minor artefacts that appear in the dQSM maps appear to originate from the ends of the cylinders. A plausible reason for these artefacts is a discrepancy between the simulated susceptibility distribution of the cylinders and that which would realistically occur. That is, real susceptibility properties at the ends of these cylinders would not conform to an abrupt change from an infinitely long cylindrical structure to a spherically structured medium, as has been simulated here. Also of note is the large spatial extent to which these artefacts appear relative to their suggested origin. This was a result of convolution, where the error in the susceptibility of one voxel propagates to an error in the subsequently calculated ΔB values of neighbouring voxels. While the linear system solving algorithms were designed to minimise this error, they rely on an accurate model of the system. Where the system does not accurately model the data, such as when spherical model kernels were applied to cylindrically structured tissues, the system introduced errors which were then propagated by the convolution calculations.

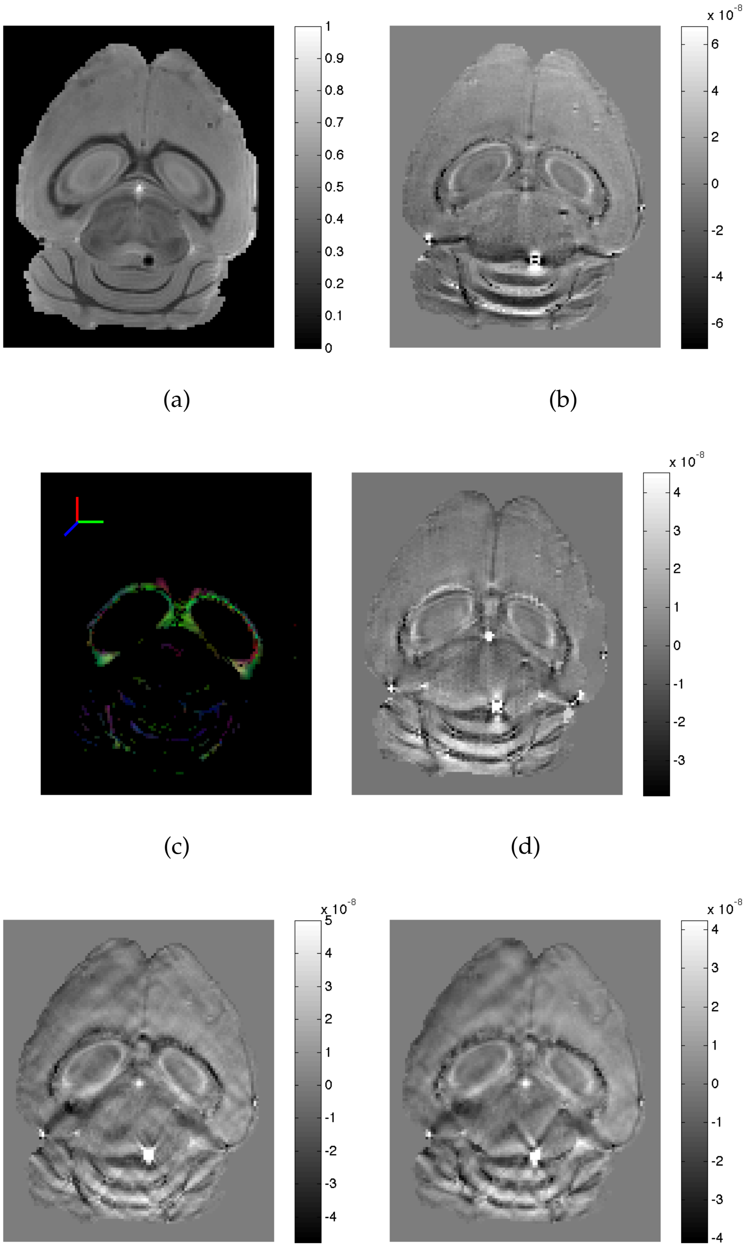

(a) (b)

(c) (d)

(e) (f)

Figure 39: Axial slice of the fixed mouse brain, showing (a) magnitude image, (b) ΔB map, (c) diffusion tensors weighted by FA, and susceptibility maps derived by (d) MEDI, (e) sQSM and (f) dQSM.

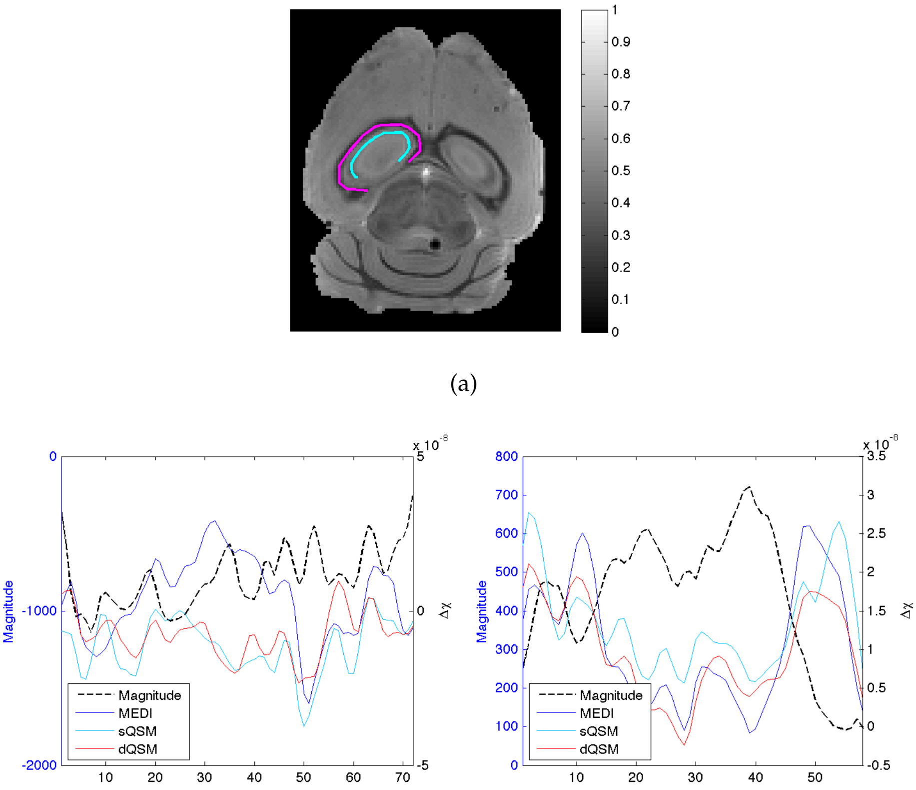

(a)

(b) (c)

Figure 40: The (a) magnitude image was used to identify line profiles in the white matter. The pink line corresponds to (b) and the blue line corresponds to (c), where the plots follow the lines in an anti-clockwise direction.

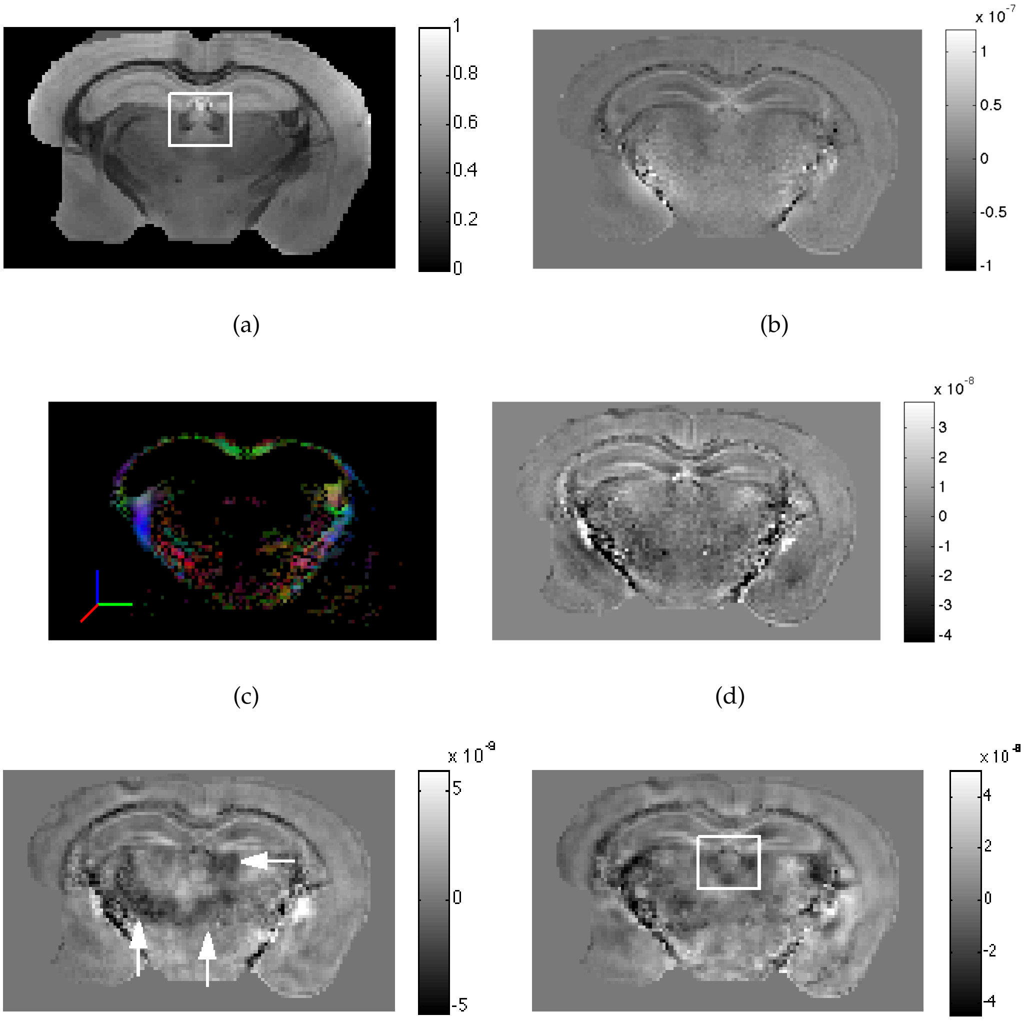

(a) (b)

(c) (d)

(e) (f)

Figure 41: Coronal slice of the fixed mouse brain, showing (a) magnitude image, (b) ΔB map, (c) diffusion tensors weighted by FA, and susceptibility maps derived by (d) MEDI method, (e) sQSM and (f) dQSM.

dQSM performed poorer in the presence of noise. MEDI and dQSM use different regularisation methods to minimise the error, being a first-order and a second order operation, respectively. They also employ different weightings on the regularisation parameter. MEDI's first-order regularisation is expected to result in better noise reduction, however the application of the magnitude gradient-based map results in unreliable susceptibility estimates in voxels at the border between structures. The decrease in noise in the MEDI susceptibility map in response to increased phase noise is counter-intuitive. The interaction between the system fidelity term and regularisation term, combined with iterative optimisation methods, could produce the results seen here, particularly given the substantial weighting that needed to be placed on the smoothing regularisation in order to avoid the cross-shaped artefact. The second order regularisation employed by dQSM aimed to address this problem while maintaining an acceptable level of noise. The smoothed mouse maps and noisy phantom maps suggest that optimisation of the regularisation weighting parameter, κ, in the dQSM method is required to achieve the optimal SNR. Unfortunately, the computational expense of dQSM prohibits an extensive search for optimal κ.

A comparison of the two methods based only on the spherical model, MEDI and sQSM, highlights the significant difference in results for what is fundamentally the same model of the physical interactions between the tissue susceptibilities and the applied magnetic field. Not only do the methods produce different mean susceptibility estimates, but the location of artefacts is very different. The major differences between the two approaches are: 1) the use of the discrete image-space kernel versus the discretised CFT-derived k-space kernel, 2) the use of a first-order versus second-order regularisation term, and 3) the computation of the $\mathbf{A}'(\mathbf{Ax}-\mathbf{b})$ terms explicitly versus fast Fourier transforms. Investigating how these differences affect the numerical modelling of the system is an interesting topic within which improvements to QSM methods may lie.

The susceptibility maps of the mouse brain further demonstrated the advantages and limitations of the methods. dQSM and sQSM performed significantly better than MEDI at resolving white matter structures. The ability of the sQSM to produce similar estimates of white matter values compared to dQSM is unsurprising given that both methods produced relatively accurate estimates of the cylinder susceptibilities in the numerical phantom. However, as was apparent in the numerical phantom results, large artefacts, appearing as hypointense regions, occurred in the sQSM maps that were not present in the dQSM maps. This suggests that dQSM has an enhanced ability to produce accurate estimates of susceptibility in regions outside of, but within proximity of cylindrical structures. Further evidence in support of this ability is the presence of the subcortical structure in the dQSM and magnitude image, but not in any other maps, including the diffusion tensor map that indicates the presence of white matter.

While dQSM produced more accurate susceptibility maps than the MEDI method, the computational expense is far greater than that of the MEDI method. The very large difference in computational expense is due to the application of the convolution theorem in the MEDI method. The fast Fourier transform algorithm employed in the MEDI method has a computational efficiency of $O\left(N \log N\right)$ operations per iteration. Since dQSM does not involve a true convolution, i.e. the choice of kernel is spatially dependent, it is restricted to longer computations in the spatial domain, having a computational efficiency of $O\left(N^2\right)$ operations per iteration. Although dQSM is more accurate than methods involving only a spherical kernel, the computation time is prohibitively long for most research requirements, let alone clinical applications. This highlights the need for further research into faster algorithms to solve this particular large scale linear system. Recently, a GPU acceleration of the dQSM algorithm was implemented, with significant decreases of computation time for the mouse dataset from 16 hours on 4096 BlueGene/Q CPU cores to a projected 1.1 hours on 16 Kepler K10 GPUs [35].

The current gold standard approach to QSM is the COSMOS method, requiring multiple acquisitions at different orientations to the main B field. Multiple acquisitions are not ideal clinically and may not be feasible due to patient discomfort and setup times. As such, only single acquisition approaches were evaluated in this chapter. To extend dQSM to multiple orientations, one has to consider not only the spherical kernel, but the multiple arbitrarily oriented cylinder kernels. For spherically modelled voxels, three COSMOS-type acquisitions will address the under-determined nature of the spherical kernel by ensuring that all points in k-space have a non-zero value for at least one of the acquisitions. This is achieved by ensuring that the zero cones do not overlap. The cylindrical kernel is also under-determined. In k-space, there also exists points where the kernel is zero, presenting as a cross-shape on the kernel (Fig. 42). At least two acquisitions are required to compensate for the under-determined kernel, however the orientations must be such that the zero voxels do not overlap. The requirements on the three COSMOS orientations are sufficient to meet this criterium, regardless of the orientation of the cylinder. Therefore it is possible to apply a multiple orientation approach to dQSM.

7.5 CONCLUSION

The results of dQSM presented in this chapter suggests greater accuracy in susceptibility estimation compared to methods based solely on a spherical model, particularly in the presence of structurally cylindrical tissues such as white matter. The major disadvantage is the very long computation time, which makes the method, as described here, infeasible for everyday research and clinical applications. It is,

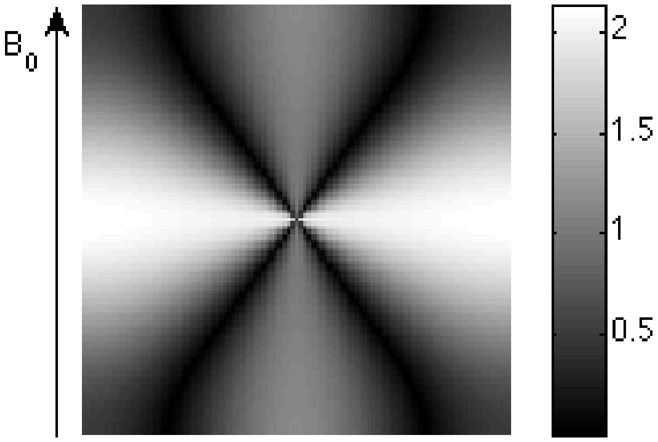

Figure 42: Fourier transform of the cylindrical kernel, showing the plane normal to the cylinder axis.

however, a proof of concept demonstrating that a mixed model provides a more accurate approach to QSM and that further investigation into optimising dQSM numerical implementation is warranted.

7.6 APPENDIX

The analytical expression for the change in the magnetic B field induced by a sphere and by a cylinder are well-known and mathematical derivations, with varying degrees of detail, have been published [36, 37]. The Lorentz Sphere correction to the change in B field due to a sphere has also been published. Here, we provide a complete, detailed derivation of change in B field induced by a sphere as well as a detailed derivation of the change in B field due to a cylinder. We also perform the Lorentz correction for both expressions and formulate the discrete convolution kernels required for the dQSM computations.

The following mathematical notations are employed:

$\hat{\boldsymbol{x}}, \hat{\boldsymbol{y}}, \hat{\boldsymbol{z}}$ unit vectors defining a cartesian coordinate system

$\hat{\boldsymbol{r}}, \hat{\boldsymbol{\theta}}, \hat{\boldsymbol{\phi}}$ unit vectors defining a spherical coordinate system

$\hat{\boldsymbol{r}}, \hat{\boldsymbol{\phi}}, \hat{\boldsymbol{z}}$ unit vectors defining a cylindrical coordinate system

$\boldsymbol{r} = (x, y, z)$ position vector in image space in cartesian coordinates. x, y and z are the projections of $\boldsymbol{r}$ on $\hat{\boldsymbol{x}}$, $\hat{\boldsymbol{y}}$ and $\hat{\boldsymbol{z}}$, respectively.

$\boldsymbol{r} = (r, \theta, \varphi)$ position vector in image space in spherical coordinates. r is the length of the position vector, θ is the angle between $\boldsymbol{r}$ and $\hat{\boldsymbol{z}}$, and φ is the angle between $\boldsymbol{r}$ and $\hat{\boldsymbol{x}}$.

$\boldsymbol{r} = (r, \varphi, z)$ position vector in image space in cylindrical coordinates. r is the distance from the z axis, φ is the angle between $\boldsymbol{r}$ and $\hat{\boldsymbol{x}}$ and z is the projection of $\hat{\boldsymbol{r}}$ on $\hat{\boldsymbol{z}}$.

$\boldsymbol{k} = (k_x, k_y, k_z)$ position vector in k-space defined in cartesian coordinates

$\boldsymbol{H}, H$ vector describing the magnitude and direction of the magnetic field intensity, magnitude of the magnetic field intensity

$\boldsymbol{B}, B$ vector describing the magnitude and direction of the magnetic flux density, magnitude of the magnetic field intensity

$\boldsymbol{H}_0, \boldsymbol{B}_0$ magnetic flux density and field intensity of the external applied magnetic field

χ magnetic volume susceptibility

μ magnetic permeability

F_S, F_C 3D kernel describing the effects on the magnetic flux density induced by a sphere (S) or a cylinder (C)

A1 The change in B field induced by a sphere

The spherical model of the influence of magnetic susceptibility, χ, on magnetic flux density, $\boldsymbol{B}$, is derived as the change in $\boldsymbol{B}$ due to a sphere of homogeneous and isotropic susceptibility[1] exposed to an external uniform magnetic field, $\boldsymbol{B}_0$. The coordinate system is defined such that the centre of the sphere is located at the origin and the $\hat{\boldsymbol{z}}$ is parallel to the direction of $\boldsymbol{B}_0$. The sphere has radius a. The susceptibility inside and outside the sphere is denoted by χ_{in} and χ_{out}, respectively. The outside medium is considered to extend to $\pm\infty$ in all directions.

The magnetic field intensity, $\boldsymbol{H}$, is a vector field describing the direction and intensity of the magnetic field at any given point and is related to the magnetic flux density according to

$$\boldsymbol{B} = \mu \boldsymbol{H} \tag{7.24}$$

where μ is the magnetic permeability of the medium. Its relation to susceptibility is given by

$$\mu = (1 + \chi)\,\mu_0 \tag{7.25}$$

where $\mu_0 = 4\pi \times 10^{-7}$ H.M^{-1} is a constant known as the permeability of free space. To facilitate our derivations, we define a scalar field, Ω, such that

$$\boldsymbol{H} = -\nabla\Omega \tag{7.26}$$

---

[1] Note that the term susceptibility will be used to refer to magnetic susceptibility, as distinct from electric susceptibility.

where ∇ is the gradient operator defined in cartesian coordinates as

$$\nabla f = \frac{\partial f}{\partial x}\hat{\boldsymbol{x}} + \frac{\partial f}{\partial y}\hat{\boldsymbol{y}} + \frac{\partial f}{\partial z}\hat{\boldsymbol{z}}, \tag{7.27}$$

in spherical coordinates as

$$\nabla f = \frac{\partial f}{\partial r}\hat{\boldsymbol{r}} + \frac{1}{r}\frac{\partial f}{\partial \theta}\hat{\boldsymbol{\theta}} + \frac{1}{r\sin\theta}\frac{\partial f}{\partial \varphi}\hat{\boldsymbol{\varphi}}, \tag{7.28}$$

and in cylindrical coordinates as

$$\nabla f = \frac{\partial f}{\partial r}\hat{\boldsymbol{r}} + \frac{1}{r}\frac{\partial f}{\partial \varphi}\hat{\boldsymbol{\theta}} + \frac{\partial f}{\partial z}\hat{\boldsymbol{z}}. \tag{7.29}$$

Since the relationship to $\boldsymbol{H}$ is a gradient function, constant offsets in Ω can be ignored, that is

$$\Omega = f\left(x,y,z\right) + c \equiv f\left(x,y,z\right).$$

Conditions

Let Ω_{in} be the scalar potential inside the sphere and Ω_{out} is the scalar potential outside the sphere. We derive below the following conditions on Ω_{in} and Ω_{out}:

1. For $r < a$, $\nabla^2\Omega_{in} = 0$, and for $r > a$, $\nabla^2\Omega_{out} = 0$.
2. For $r \gg a$, $\Omega_{out} = -H_0 r\cos\theta$.
3. For all r, Ω must be finite.
4. For $r = a$, $\mu_{in}\frac{\partial\Omega_{in}}{\partial r} = \mu_{out}\frac{\partial\Omega_{out}}{\partial r}$.
5. For $r = a$, $\frac{\partial\Omega_{in}}{\partial\theta} = \frac{\partial\Omega_{out}}{\partial\theta}$.

Condition 1: Laplace's equation.

Combining (7.24),(7.26) and Maxwell's second equation,

$$\nabla\cdot\boldsymbol{B} = 0 \tag{7.30}$$

the following condition can be derived

$$\begin{aligned}\nabla\cdot(\mu\boldsymbol{H}) &= 0\\ \nabla\cdot(\mu(-\nabla\Omega)) &= 0\\ -\mu\nabla\cdot\nabla\Omega &= 0\\ \nabla^2\Omega &= 0.\end{aligned} \tag{7.31}$$

This is Laplace's equation and is applicable, though independently, to both the scalar potential inside and the scalar potential outside the sphere. Thus,

$$\nabla^2 \Omega_{in} = 0 \tag{7.32}$$

and

$$\nabla^2 \Omega_{out} = 0. \tag{7.33}$$

Condition 2: magnetic field is equal to the applied field far from the sphere.

Let $\boldsymbol{H}_0$ denote the field far away from the sphere. When $r \gg a$, the influence of the sphere on the magnetic field is negligible, such that

$$-\nabla \Omega_{out} = \boldsymbol{H}_0$$

gives

$$\frac{\partial \Omega_{out}}{\partial x} \hat{\boldsymbol{x}} + \frac{\partial \Omega_{out}}{\partial y} \hat{\boldsymbol{y}} + \frac{\partial \Omega_{out}}{\partial z} \hat{\boldsymbol{z}} = -H_0 \hat{\boldsymbol{z}}.$$

Thus, Ω_{out} is a function of z only, and

$$\begin{aligned} \frac{d\Omega_{out}}{dz} &= -H_0 \\ \Omega_{out} &= -H_0 z. \end{aligned}$$

Since $z = r\cos\theta$,

$$\Omega_{out} = -H_0 r \cos\theta. \tag{7.34}$$

Condition 3: Ω must be finite.

If Ω is infinite, $\nabla^2\Omega$ would be undefined. Since $\nabla^2\Omega = 0$, Ω must therefore be finite.

Condition 4: at the sphere's surface, the normal component of the magnetic flux density is continuous

Consider a cylinder with closed surfaces at the ends (a pillbox) whose axis is normal to the surface of the sphere. If the lateral surface of the pillbox is very small, the only contributions to the magnetic flux density, $\boldsymbol{B}$, through the surface of the pillbox will be through the surfaces at the ends of the cylinder, S_{in} and S_{out}. Let the components of $\boldsymbol{B}$ that are normal to the ends of the pillbox be $B_{n,in}$ and $B_{n,out}$. If the area, A, of the ends of the pillbox is also considered small, then from Maxwell's second equation in the integral form

$$\oint_S \boldsymbol{B}.d\mathbf{S} = 0,$$

we have

$$\begin{aligned}
-\oint_{S_{in}} B_{n,in}.d\mathbf{S} + \oint_{S_{out}} B_{n,out}.d\mathbf{S} &= 0 \\
B_{n,in}.A - B_{n,out}.A &= 0 \\
B_{n,in} &= B_{n,out}
\end{aligned}$$

or, by (7.24),

$$\mu_{in} H_{n,in} = \mu_{out} H_{n,out}.$$

From (7.26) and (7.28),

$$\begin{aligned}
H_{n,in} &= -\frac{\partial \Omega_{in}}{\partial r}, \\
H_{n,out} &= -\frac{\partial \Omega_{out}}{\partial r},
\end{aligned}$$

and so,

$$\mu_{in} \frac{d\Omega_{in}}{dr} = \mu_{out} \frac{d\Omega_{out}}{dr}. \tag{7.35}$$

Condition 5: at the sphere's surface, the tangential components of magnetic field intensity inside and outside the sphere are equal

Consider a small rectangular closed loop that crosses the sphere's surface and lies in a plane normal to the sphere's surface and parallel to $\hat{\mathbf{z}}$. The sides of the rectangle normal to the sphere's surface are negligibly small compared to the sides of the rectangle parallel to the sphere's surface. These parallel sides, L_{in} and L_{out}, are very small, such that $\boldsymbol{H}$ is uniform over their lengths, ΔL. Using Maxwell's fourth equation, and noting that the sphere's surface contains no free currents or charges,

$$\oint \mathbf{H}.d\mathbf{L} = 0$$

gives

$$\int_{L_{in}} H_{t,in}.d\mathbf{L} - \int_{L_{out}} H_{t,out}.d\mathbf{L} = 0,$$

where the subscript t denotes a tangential component of $\boldsymbol{H}$ along the sides of the rectangle. Thus,

$$\begin{aligned}
H_{t,in}\Delta L - H_{t,out}\Delta L &= 0, \\
H_{t,in} &= H_{t,out}.
\end{aligned}$$

Since the rectangle is parallel to $\hat{\mathbf{z}}$ and lies on the surface of the sphere, (7.26) and (7.28) give

$$H_{t,in} = \frac{1}{r}\frac{\partial \Omega_{in}}{\partial \theta}$$

and

$$H_{t,out} = \frac{1}{r}\frac{\partial \Omega_{out}}{\partial \theta}.$$

Thus

$$\begin{aligned} \frac{1}{r}\frac{\partial \Omega_{in}}{\partial \theta} &= \frac{1}{r}\frac{\partial \Omega_{out}}{\partial \theta}, \\ \frac{\partial \Omega_{in}}{\partial \theta} &= \frac{\partial \Omega_{out}}{\partial \theta}. \end{aligned} \tag{7.36}$$

The general solution to Laplace's equation in spherical coordinates

Laplace's equation (7.31) in spherical coordinates is

$$\begin{aligned} \nabla^2 \Omega &= \frac{1}{r^2}\frac{\partial}{\partial r}\left(r^2 \frac{\partial \Omega}{\partial r}\right) + \frac{1}{r^2 \sin\theta}\frac{\partial}{\partial \theta}\left(\sin\theta \frac{\partial \Omega}{\partial \theta}\right) + \frac{1}{r^2 \sin^2\theta}\frac{\partial^2 \Omega}{\partial \varphi^2}. \\ &= 0. \end{aligned} \tag{7.37}$$

The solution is derived by separating the independent variables, r, θ and φ. The scalar potential can be written as

$$\Omega = R\left(r\right)\Theta\left(\theta\right)\Phi\left(\varphi\right). \tag{7.38}$$

Substituting this into (7.37), we have

$$\frac{1}{r^2}\frac{\partial}{\partial r}\left(r^2 \frac{\partial\left(R\Theta\Phi\right)}{\partial r}\right) + \frac{1}{r^2 \sin\theta}\frac{\partial}{\partial \theta}\left(\sin\theta \frac{\partial\left(R\Theta\Phi\right)}{\partial \theta}\right) + \frac{1}{r^2 \sin^2\theta}\frac{\partial^2\left(R\Theta\Phi\right)}{\partial \varphi^2} = 0.$$

Rearrangement and multiplication by $\frac{r^2}{R\Theta\Phi}$ yields

$$\frac{1}{R}\frac{d}{dr}\left(r^2\frac{dR}{dr}\right) + \frac{1}{\Theta}\frac{1}{\sin\theta}\frac{d}{d\theta}\left(\sin\theta\frac{d\Theta}{d\theta}\right) + \frac{1}{\Phi}\frac{1}{\sin^2\theta}\frac{d^2\Phi}{d\varphi^2} = 0. \tag{7.39}$$

Let

$$\frac{1}{R}\frac{d}{dr}\left(r^2\frac{dR}{dr}\right) = p \tag{7.40}$$

$$\frac{1}{\Theta}\frac{1}{\sin\theta}\frac{d}{d\theta}\left(\sin\theta\frac{d\Theta}{d\theta}\right) + \frac{1}{\Phi}\frac{1}{\sin^2\theta}\frac{d^2\Phi}{d\varphi^2} = -p. \tag{7.41}$$

Separation of variables is again applied to the second equation,

$$\frac{1}{\Theta}\sin\theta\frac{d}{d\theta}\left(\sin\theta\frac{d\Theta}{d\theta}\right) + \frac{1}{\Phi}\frac{d^2\Phi}{d\varphi^2} = -p\sin^2\theta. \tag{7.42}$$

While $\hat{z}$ is defined by the direction of the applied magnetic field, the positioning of $\hat{x}$ and $\hat{y}$ are arbitrary. Therefore, for Ω to be invariant with respects to the definition of the coordinate system,

$$\Phi(\varphi) = E \tag{7.43}$$

where E is a constant. Thus,

$$\frac{1}{\Phi}\frac{d^2\Phi}{d\varphi^2} = 0. \tag{7.44}$$

Substituting (7.44) into (7.42), we have

$$\frac{1}{\Theta}\sin\theta\frac{d}{d\theta}\left(\sin\theta\frac{d\Theta}{d\theta}\right) + p\sin^2\theta = 0.$$

To solve this, we use a change of variables, $w = \cos\theta$ and therefore $\frac{d\theta}{dw} = \frac{-1}{\sin\theta}$, and rearrange to form the Legendre Differential Equation,

$$\begin{aligned}
\sin\theta\frac{d}{d\theta}\left(\sin\theta\frac{d\Theta}{d\theta}\right) + \left(p\sin^2\theta\right)\Theta &= 0,\\
-\sin^2\theta\frac{d}{dw}\left(-\sin^2\theta\frac{d\Theta}{dw}\right) + \left(p\sin^2\theta\right)\Theta &= 0,\\
\left(1-w^2\right)\frac{d}{dw}\left[\left(1-w^2\right)\frac{d\Theta}{dw}\right] + \left[p\left(1-w^2\right)\right]\Theta &= 0,\\
\left(1-w^2\right)\frac{d^2\Theta}{dw^2} - 2w\frac{d\Theta}{dw} + n\left(n+1\right)\Theta &= 0,
\end{aligned}$$

where we have substituted $p = n\left(n+1\right)$. The solutions to this equation are known as the Legendre polynomials,

$$\Theta_n\left(\cos\theta\right) = \frac{1}{2^n n!}\frac{d^n}{d\left(\cos\theta\right)^n}\left(\cos^2\theta - 1\right)^n. \tag{7.45}$$

The first few solutions are

$$\begin{aligned}
\Theta_0\left(\theta\right) &= 1,\\
\Theta_1\left(\theta\right) &= \cos\theta,\\
\Theta_2\left(\theta\right) &= \frac{1}{2}\left(3\cos^2\theta - 1\right),
\end{aligned} \tag{7.46}$$

where successive solutions have increasing powers of $\cos\theta$. (7.40) is expanded to give the Euler equation,

$$r^2\frac{d^2R}{dr^2} + 2r\frac{dR}{dr} - n\left(n+1\right)R = 0$$

which has the solution

$$R_n(r) = C_n r^n + D_n \frac{1}{r^{n+1}}. \tag{7.47}$$

The solution of (7.38) is then

$$\begin{aligned}\Omega &= R(r)\,\Theta(\theta)\,\Phi(\varphi)\\ &= \sum_{n=0}^{\infty}\left(C_n r^n + D_n \frac{1}{r^{n+1}}\right)\Theta_n(\theta)\,E.\end{aligned} \tag{7.48}$$

Since C_n and D_n are unknown constant coefficients, we can let $E = 1$. Expanding the $n < 2$ terms, we have

$$\Omega \;=\; C_0 + D_0\frac{1}{r} + C_1 r\cos\theta + D_1\frac{1}{r^2}\cos\theta + \sum_{n=2}^{\infty}\left(C_n r^n + D_n\frac{1}{r^{n+1}}\right)\Theta_n(\theta).$$

Applying condition 2: $\Omega_{out} = -H_0 r\cos\theta$ where $r \gg a$

When r approaches ∞, the $\frac{1}{r^{n+1}}$ terms in (7.48) approach zero and

$$\Omega_{out,r\to\infty} = C_{out,0} + C_{out,1} r\cos\theta + \sum_{n=2}^{\infty} C_{out,n} r^n \Theta_n(\theta).$$

Since $\Omega_{out} = -H_0 r\cos\theta$ when $r \to \infty$ and referring to (7.46), we can see that only the $n = 1$ term has a first order $\cos\theta$ term. Therefore

$$\Omega_{out,r\to\infty} \;=\; C_{out,1} r\cos\theta$$

and

$$C_{out,n} \;=\; \begin{cases} -H_0, & n = 1\\ 0, & \text{otherwise.}\end{cases} \tag{7.49}$$

Applying condition 3: Ω must be finite

When $r = 0$, the $\frac{1}{r^{n+1}}$ terms approach ∞. Since Ω must be finite,

$$D_{in,n} = 0, \text{ for all } n. \tag{7.50}$$

To summarise,

$$\begin{aligned}\Omega_{in} &= C_{in,0} + C_{in,1} r\cos\theta + \sum_{n=2}^{\infty} C_{in,n} r^n \Theta_n(\theta),\\ \Omega_{out} &= -H_0 r\cos\theta + D_{out,0}\frac{1}{r} + D_{out,1}\frac{1}{r^2}\cos\theta + \sum_{n=2}^{\infty} D_{out,n}\frac{1}{r^{n+1}}\Theta_n(\theta).\end{aligned}$$

Applying condition 4: $\mu_{in}\frac{d\Omega_{in}}{dr} = \mu_{out}\frac{d\Omega_{out}}{dr}$ *where* $r = a$

We substitute (7.49) and (7.50) into (7.48), then let $r = a$

$$\begin{aligned}
\mu_{in}\frac{\partial}{\partial r}\Omega_{in}\bigg|_{r=a} &= \mu_{in}\frac{\partial}{\partial r}\left[C_{in,0} + C_{in,1}r\cos\theta + \sum_{n=2}^{\infty} C_{in,n}r^{n}\Theta_n\right]_{r=a} \\
&= \mu_{in}\left[C_{in,1}\cos\theta + \sum_{n=2}^{\infty} C_{in,n}na^{n-1}\Theta_n\right], \qquad (7.51) \\
\mu_{out}\frac{\partial}{\partial r}\Omega_{out}\bigg|_{r=a} &= \mu_{out}\frac{\partial}{\partial r}\left[-H_0 r\cos\theta + D_{out,0}\frac{1}{r} + D_{out,1}\frac{1}{r^2}\cos\theta \right. \\
&\quad \left. + \sum_{n=2}^{\infty}\left(D_{out,n}\frac{1}{r^{n+1}}\right)\Theta_n\right] \\
&= \mu_{out}\left[-H_0\cos\theta - D_{out,0}\frac{1}{a^2} - 2D_{out,1}\frac{1}{a^3}\cos\theta \right. \\
&\quad \left. + \sum_{n=2}^{\infty}\left(D_{out,n}\left(-n-1\right)\frac{1}{a^{n+2}}\right)\Theta_n\right]. \qquad (7.52)
\end{aligned}$$

Equating coefficients of terms independent of θ, we have

$$D_{out,0} = 0.$$

Equating coefficients of first order $\cos\theta$ terms, we have

$$\mu_{in}C_{in,1} = -\mu_{out}\left(H_0 + 2D_{out,1}\frac{1}{a^3}\right). \qquad (7.53)$$

Applying condition 5: $\frac{\partial\Omega_{in}}{\partial\theta} = \frac{\partial\Omega_{out}}{\partial\theta}$ *for* $r = a$

Differentiating with respect to θ and letting $r = a$, we have

$$\begin{aligned}
\frac{\partial}{\partial\theta}\Omega_{in}\bigg|_{r=a} &= \frac{\partial}{\partial\theta}\left[C_{in,0} + C_{in,1}r\cos\theta + \sum_{n=2}^{\infty} C_{in,n}r^{n}\Theta_n\right]_{r=a} \\
&= -C_{in,1}a\sin\theta + \sum_{n=2}^{\infty} C_{in,n}a^{n}\frac{\partial}{\partial\theta}\Theta_n, \qquad (7.54) \\
\frac{\partial}{\partial\theta}\Omega_{out}\bigg|_{r=a} &= \frac{\partial}{\partial\theta}\left[-H_0 r\cos\theta + D_{out,1}\frac{1}{r^2}\cos\theta + \sum_{n=2}^{\infty}\left(D_{out,n}\frac{1}{r^{n+1}}\right)\Theta_n\right] \\
&= -H_0 a\sin\theta + D_{out,1}\frac{1}{a^2}\sin\theta + \sum_{n=2}^{\infty}\left(D_{out,n}\frac{1}{a^{n+1}}\right)\frac{\partial}{\partial\theta}\Theta_n. \qquad (7.55)
\end{aligned}$$

Equating coefficients of $\sin\theta$, we have

$$C_{in,1}a = -H_0 a + D_{out,1}\frac{1}{a^2}.$$

Combining with (7.53),

$$\begin{aligned}
-a\frac{\mu_{out}}{\mu_{in}}\left(H_0+2D_{out,1}\frac{1}{a^3}\right) &= -H_0a+D_{out,1}\frac{1}{a^2}, \\
H_0+2D_{out,1}\frac{1}{a^3} &= \frac{\mu_{in}}{\mu_{out}}H_o-\frac{\mu_{in}}{\mu_{out}}D_{out,1}\frac{1}{a^3}, \\
D_{out,1}\left(\frac{2}{a^3}+\frac{\mu_{in}}{\mu_{out}}\frac{1}{a^3}\right) &= H_0\left(\frac{\mu_{in}}{\mu_{out}}-1\right), \\
D_{out,1} &= H_0a^3\left(\frac{\mu_{in}}{\mu_{out}}-1\right)\left(2+\frac{\mu_{in}}{\mu_{out}}\right)^{-1} \\
&= H_0a^3\left(\frac{\mu_{in}-\mu_{out}}{2\mu_{out}+\mu_{in}}\right), \\
C_{in,1} &= H_0\left(\frac{\mu_{in}-\mu_{out}}{2\mu_{out}+\mu_{in}}-1\right) \\
&= H_0\left(\frac{-3\mu_{out}}{2\mu_{out}+\mu_{in}}\right).
\end{aligned}$$

$C_{in,0}$ is a constant and can be ignored, as previously mentioned,

$$C_{in,0} = 0.$$

The remaining coefficients to be determined are those corresponding to $n \geq 2$. Equating coefficients of $\frac{\partial}{\partial\theta}\Theta_n$ in (7.54) and (7.55),

$$\begin{aligned}
C_{in,n}a^n &= D_{out,n}\frac{1}{a^{n+1}}, \text{ where } n \geq 2 \\
\Rightarrow C_{in,n} &= D_{out,n}\frac{1}{a^{2n+1}}.
\end{aligned} \tag{7.56}$$

Equating coefficients of Θ_n $(n \geq 2)$ in (7.51) and (7.52),

$$\begin{aligned}
\mu_{in}C_{in,n}na^{n-1} &= -\mu_{out}D_{out,n}\left(n+1\right)\frac{1}{a^{n+2}}, \\
C_{in,n} &= -\frac{\mu_{out}}{\mu_{in}}\cdot\frac{n+1}{n}\cdot\frac{1}{a^{2n+1}}D_{out,n}.
\end{aligned} \tag{7.57}$$

Equating (7.56) and (7.57),

$$\begin{aligned}
D_{out,n} &= -\frac{\mu_{out}}{\mu_{in}}\cdot\frac{n+1}{n}\cdot D_{out,n}, \\
D_{out,n}\left(1+\frac{\mu_{out}}{\mu_{in}}\cdot\frac{n+1}{n}\right) &= 0.
\end{aligned}$$

Hence,

$$D_{out,n} = 0,$$

and

$$C_{in,n} = 0.$$

With the substitutions of coefficients, $\mu = \mu_o (1 + \chi)$ and $r \cos\theta = z$, our scalar functions are

$$\begin{aligned} \Omega_{in} &= \frac{-3(1+\chi_{out})}{3+2\chi_{out}+\chi_{in}} H_0 z, && (7.58) \\ \Omega_{out} &= -H_0 z + \frac{\chi_{in}-\chi_{out}}{3+2\chi_{out}+\chi_{in}} a^3 H_0 \frac{r\cos\theta}{r^3}. && (7.59) \end{aligned}$$

Equations for the field induced inside the sphere

The magnetic field intensity, $\boldsymbol{H}_{in}$, inside the sphere can be obtained from (7.58)

$$\begin{aligned} \boldsymbol{H}_{in} &= -\nabla\Omega_{in} \\ &= \frac{3(1+\chi_{out})}{3+2\chi_{out}+\chi_{in}} \boldsymbol{H}_0. \end{aligned}$$

The magnetisation, $\boldsymbol{M}_{in}$, is then derived as follows

$$\begin{aligned} \boldsymbol{M}_{in} &= \chi_{in}\boldsymbol{H}_{in} \\ &= \frac{3\chi_{in}(1+\chi_{out})}{3+2\chi_{out}+\chi_{in}} \boldsymbol{H}_0. \end{aligned}$$

and the magnetic flux density inside the sphere, $\boldsymbol{B}_{in}$, is

$$\begin{aligned} \boldsymbol{B}_{in} &= \mu_{in}\boldsymbol{H}_{in} \\ &= \frac{3(1+\chi_{out})(1+\chi_{in})}{3+2\chi_{out}+\chi_{in}} \boldsymbol{B}_0. \end{aligned}$$

Equations for the field induced outside the sphere

The magnetic field intensity, $\boldsymbol{H}_{out}$, outside the sphere can be obtained from (7.59)

$$\begin{aligned} \mathbf{H}_{out} &= \boldsymbol{H}_0 + \frac{\chi_{in}-\chi_{out}}{3+2\chi_{out}+\chi_{in}} a^3 H_0 \left(-\nabla\frac{r\cos\theta}{r^3}\right) \\ &= \boldsymbol{H}_0 + \frac{\chi_{in}-\chi_{out}}{3+2\chi_{out}+\chi_{in}} a^3 H_0 \left(2\frac{\cos\theta}{r^3}\hat{\boldsymbol{r}} + \frac{\sin\theta}{r^3}\hat{\boldsymbol{\theta}}\right) \\ &= \boldsymbol{H}_0 + \frac{\chi_{in}-\chi_{out}}{3+2\chi_{out}+\chi_{in}} a^3 H_0 \left(2\frac{(\hat{\boldsymbol{z}}\cdot\hat{\boldsymbol{r}})}{r^3}\hat{\boldsymbol{r}} + \frac{(\hat{\boldsymbol{z}}\cdot\hat{\boldsymbol{r}})\hat{\boldsymbol{r}}-\hat{\boldsymbol{z}}}{r^3}\right) \\ &= \boldsymbol{H}_0 + \frac{\chi_{in}-\chi_{out}}{3+2\chi_{out}+\chi_{in}} a^3 H_0 \left(\frac{3(\hat{\boldsymbol{z}}\cdot\hat{\boldsymbol{r}})\hat{\boldsymbol{r}}-\hat{\boldsymbol{z}}}{r^3}\right). \end{aligned}$$

The equality $\sin\theta\hat{\boldsymbol{\theta}} = (\hat{\boldsymbol{z}}\cdot\hat{\boldsymbol{r}})\hat{\boldsymbol{r}} - \hat{\boldsymbol{z}}$ follows from $\hat{\boldsymbol{z}} = (\hat{\boldsymbol{z}}\cdot\hat{\boldsymbol{r}})\hat{\boldsymbol{r}} - \sin\theta\hat{\boldsymbol{\theta}}$, illustrated in Fig. 43.

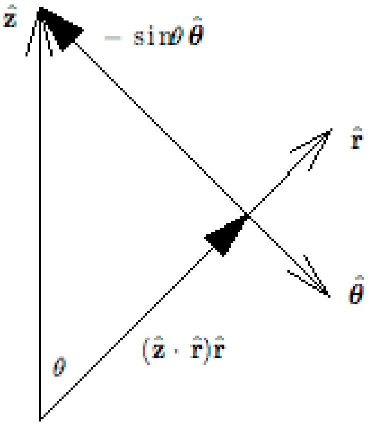

Figure 43: Illustration of the derivation of $\sin\theta\hat{\boldsymbol{\theta}} = -\left(\hat{\boldsymbol{z}}\cdot\hat{\boldsymbol{r}}\right)\hat{\boldsymbol{r}} + \hat{\boldsymbol{z}}$

The magnetisation is

$$\boldsymbol{M}_{out} = \chi_{out}\boldsymbol{H}_0 + \frac{\chi_{out}\left(\chi_{in}-\chi_{out}\right)}{3+2\chi_{out}+\chi_{in}} a^3 H_0 \left(\frac{3\left(\hat{\boldsymbol{z}}\cdot\hat{\boldsymbol{r}}\right)\hat{\boldsymbol{r}}-\hat{\boldsymbol{z}}}{r^3}\right),$$

and the magnetic flux density, $\boldsymbol{B}_0$, outside the sphere is

$$\boldsymbol{B}_{out} = \left(1+\chi_{out}\right)\boldsymbol{B}_0 + \frac{\left(1+\chi_{out}\right)\left(\chi_{in}-\chi_{out}\right)}{3+2\chi_{out}+\chi_{in}} a^3 B_0 \left(\frac{3\left(\hat{\boldsymbol{z}}\cdot\hat{\boldsymbol{r}}\right)\hat{\boldsymbol{r}}-\hat{\boldsymbol{z}}}{r^3}\right).$$

The first term is the applied field and the magnetisation induced in the outside medium due to its own susceptibility. The second term is the change in the magnetic field induced by the sphere.

A2 The change in B field induced by a cylinder

We will now derive the changes in the magnetic flux density due to an infinitely long cylinder of radius a. We define $\hat{z}$ as parallel to the axis of the cylinder. Later, we will generalise the equations for arbitrary cylinder axis orientations. The applied magnetic field, $\mathbf{H}_0$, makes an angle β with the cylinder axis (in this instance, $\hat{z}$) and is parallel to the x-z plane. In cylindrical coordinates, it is defined as

$$\boldsymbol{H}_0 = H_0\left(\sin\beta\hat{\boldsymbol{x}} + \cos\beta\hat{\boldsymbol{z}}\right). \tag{7.60}$$

Conditions that must be satisfied

The boundary conditions are similar to those that must be satisfied for the spherical derivation. We list them here, but will not derive them again.

1. Laplace's equation: For $r < a$, $\nabla^2\Omega_{in} = 0$ and for $r > a$, $\nabla^2\Omega_{out} = 0$.

2. For $r \gg a$, $\Omega_{out} = -H_0 \left(x \sin \beta + z \cos \beta \right)$.
3. For all r, Ω is finite.
4. For $r = a$, $\frac{\partial \Omega_{in}}{\partial \varphi} = \frac{\partial \Omega_{out}}{\partial \varphi}$.
5. For $r = a$, $\mu_{in} \frac{\partial \Omega_{in}}{\partial r} = \mu_{out} \frac{\partial \Omega_{out}}{\partial r}$.
6. For $r = a$, $\frac{\partial \Omega_{in}}{\partial z} = \frac{\partial \Omega_{out}}{\partial z}$.

Solving condition 1: Laplace equation in cylindrical coordinates

The Laplace equation in cylindrical coordinates is

$$\nabla^2 \Omega = \frac{1}{r} \frac{\partial}{\partial r} \left(r \frac{\partial \Omega}{\partial r} \right) + \frac{1}{r^2} \frac{\partial^2 \Omega}{\partial \varphi^2} + \frac{\partial^2 \Omega}{\partial z^2} = 0.$$

We define the scalar potential as $\Omega \left(r, \theta, z \right) = R \left(r \right) \Phi \left(\varphi \right) Z \left(z \right)$, thus

$$\frac{1}{r} \frac{\partial}{\partial r} \left(r \frac{\partial \left(R \Phi Z \right)}{\partial r} \right) + \frac{1}{r^2} \frac{\partial^2 \left(R \Phi Z \right)}{\partial \varphi^2} + \frac{\partial^2 \left(R \Phi Z \right)}{\partial z^2} = 0.$$

We separate variables by multiplying both sides by $\frac{r^2}{R \Phi Z}$,

$$\frac{r}{R} \frac{d}{dr} \left(r \frac{dR}{dr} \right) + \frac{1}{\Phi} \frac{d^2 \Phi}{d\varphi^2} + \frac{1}{Z} \frac{d^2 Z}{dz^2} = 0. \tag{7.61}$$

The positioning of the origin along the axis of the cylinder is arbitrary, therefore Ω must be independent of z and $\frac{\partial^2 \Omega}{\partial z^2} = 0$,

$$\begin{aligned} \frac{d^2 Z}{dz^2} &= 0 \\ \Rightarrow Z &= Gz + H. \end{aligned}$$

Substituting back into (7.61), we then let

$$\begin{aligned} \frac{r}{R} \frac{d}{dr} \left(r \frac{dR}{dr} \right) &= -n^2, \\ \frac{1}{\Phi} \frac{d^2 \Phi}{d\varphi^2} &= n^2. \end{aligned}$$

For $n = 0$

$$\begin{aligned} r \frac{d}{dr} \left(r \frac{dR}{dr} \right) &= 0, \\ R &= C_0 + D_0 \ln r; \end{aligned}$$

and

$$\begin{aligned} \frac{d^2\Phi}{d\varphi^2} &= 0 \\ \Rightarrow \Phi &= E_0 + F_0\varphi. \end{aligned}$$

For $n > 0$

$$\begin{aligned} r\frac{d}{dr}\left(r\frac{dR}{dr}\right) + n^2 R &= 0, \\ R &= C_n r^n + D_n \frac{1}{r^n}; \end{aligned}$$

and

$$\begin{aligned} \frac{d^2\Phi}{d\varphi^2} - n^2\Phi &= 0, \\ \Phi &= E_n \cos n\varphi + F_n \sin n\varphi \end{aligned}$$

where both the r^n and $\frac{1}{r^n}$ solutions of R must be explicitly included since $r \geq 0$.

Combining all the solutions, we have

$$\begin{aligned} \Omega &= R\Phi Z \\ &= \left(C_0 + D_0 \ln r\right)\left(E_0 + F_0\varphi\right)\left(Gz + H\right) \\ &\quad + \sum_{n=1}^{\infty}\left(C_n r^n + D_n \frac{1}{r^n}\right)\left(E_n \cos n\varphi + F_n \sin n\varphi\right)\left(Gz + H\right). \end{aligned}$$

We know that Φ must be cyclic, therefore n must be an integer and $F_0 = 0$. We expand the terms, set the constant term to zero, and rename the coefficients:

$$\begin{aligned} \Omega &= D_0 z + E_0 \ln r + F_0 z \ln r \\ &\quad + \sum_{n=1}^{\infty} C_n r^n \left(E_n \cos n\varphi + F_n z \cos n\varphi + G_n \sin n\varphi + H_n z \sin n\varphi\right) \\ &\quad + \sum_{n=1}^{\infty} D_n \frac{1}{r^n} \left(E_n \cos n\varphi + F_n z \cos n\varphi + G_n \sin n\varphi + H_n z \sin n\varphi\right). \end{aligned} \tag{7.62}$$

Applying condition 2: for $r \gg a$, $\Omega_{out} = -H_0\left(x \sin\beta + z\cos\beta\right)$

Since $x = r\cos\phi$,

$$\Omega_{out} = -H_0\left(r\cos\varphi \sin\beta + z\cos\beta\right). \tag{7.63}$$

Equating like terms between (7.62) and (7.63) and considering $r \to \infty$, we have:

$$\begin{aligned} D_{out,0} &= -H_0 \cos\beta, \\ E_{out,0} &= 0, \\ F_{out,0} &= 0. \end{aligned}$$

For $n = 1$

$$\begin{aligned} C_{out,1} E_1 &= -H_0 \sin\beta, \\ F_{out,1} &= 0, \\ G_{out,1} &= 0, \\ H_{out,1} &= 0. \end{aligned}$$

For $n \geq 2$

$$C_{out,n\geq 2} = 0.$$

For $n \geq 1$, $\frac{1}{r^n} \to 0$. Substituting these constants back into (7.62)

$$\begin{aligned} \Omega_{out} = -H_0 z \cos\beta - H_0 r \cos\varphi \sin\beta \\ + \sum_{n=1}^{\infty} D_{out,n} \frac{1}{r^n} \left(E_{out,n} \cos n\varphi + F_{out,n} z \cos n\varphi \right. \\ \left. + G_{out,n} \sin n\varphi + H_{out,n} z \sin n\varphi \right). \end{aligned} \tag{7.64}$$

Applying condition 3: Ω must be finite

When $r = 0$, $\ln r \to \infty$ and $\frac{1}{r^n} \to \infty$. Therefore, to ensure Ω is finite,

$$\begin{aligned} E_{in,0} &= 0, \\ F_{in,0} &= 0, \\ D_{in,n\geq 1} &= 0. \end{aligned}$$

Substituting into (7.62),

$$\begin{aligned} \Omega_{in} = D_{in,0} z + \sum_{n=1}^{\infty} C_{in,n} r^n \left(E_{in,n} \cos n\varphi + F_{in,n} z \cos n\varphi \right. \\ \left. + G_{in,n} \sin n\varphi + H_{in,n} z \sin n\varphi \right). \end{aligned} \tag{7.65}$$

Applying condition 4: for $r = a$, $\frac{\partial \Omega_{in}}{\partial \varphi} = \frac{\partial \Omega_{out}}{\partial \varphi}$

Using the expressions in (7.64) and (7.65) and substituting $r = a$,

$$\left.\frac{\partial \Omega_{out}}{\partial \varphi}\right|_{r=a} = H_0 a \sin\varphi \sin\beta + \sum_{n=1}^{\infty} D_{out,n} \frac{1}{a^n} \left(-E_{out,n} n \sin n\varphi \right.$$
$$\left. - F_{out,n} zn \sin n\varphi + G_{out,n} n \cos n\varphi + H_{out,n} zn \cos n\varphi \right),$$

$$\left.\frac{\partial \Omega_{in}}{\partial \varphi}\right|_{r=a} = \sum_{n=1}^{\infty} C_{in,n} a^n \left(-E_{in,n} n \sin n\varphi - F_{in,n} zn \sin n\varphi \right.$$
$$\left. + G_{in,n} n \cos n\varphi + H_{in,n} zn \cos n\varphi \right).$$

We apply the equality $\frac{\partial \Omega_{out}}{\partial \varphi} = \frac{\partial \Omega_{in}}{\partial \varphi}$ and equate the coefficients,

$$\begin{aligned}
D_{out,1} E_{out,1} &= H_0 a^2 \sin\beta + C_{in,1} E_{in,1} a^2, \\
D_{out,n\geq 2} E_{out,n\geq 2} &= C_{in,n\geq 2} E_{in,n\geq 2} a^{2n}, \\
D_{out,n\geq 1} F_{out,n\geq 1} &= C_{in,n\geq 1} F_{in,n\geq 1} a^{2n}, \\
D_{out,n\geq 1} G_{out,n\geq 1} &= C_{in,n\geq 1} G_{in,n\geq 1} a^{2n}, \\
D_{out,n\geq 1} H_{out,n\geq 1} &= C_{in,n\geq 1} H_{in,n\geq 1} a^{2n}.
\end{aligned} \tag{7.66}$$

Applying condition 5: for $r = a$, $\mu_{in} \frac{\partial \Omega_{in}}{\partial r} = \mu_{out} \frac{\partial \Omega_{out}}{\partial r}$

Using the expressions in (7.64) and (7.65) and substituting $r = a$,

$$\mu_{in} \left.\frac{\partial \Omega_{in}}{\partial r}\right|_{r=a} = \mu_{in} \sum_{n=1}^{\infty} C_{in,n} n a^{n-1} \left(E_{in,n} \cos n\varphi + F_{in,n} z \cos n\varphi \right.$$
$$\left. + G_{in,n} \sin n\varphi + H_{in,n} z \sin n\varphi \right),$$

$$\mu_{out} \left.\frac{\partial \Omega_{out}}{\partial r}\right|_{r=a} = -\mu_{out} H_0 \cos\varphi \sin\beta + \mu_{out} \sum_{n=1}^{\infty} D_{out,n} \frac{-n}{a^{n+1}} \times$$
$$\left(E_{out,n} \cos n\varphi + F_{out,n} z \cos n\varphi + G_{out,n} \sin n\varphi + H_{out,n} z \sin n\varphi \right).$$

We apply the equality $\mu_{in}\frac{\partial\Omega_{in}}{\partial r} = \mu_{out}\frac{\partial\Omega_{out}}{\partial r}$ and equate coefficients,

$$\begin{aligned}
C_{in,1}E_{in,1} &= \frac{\mu_{out}}{\mu_{in}}\left(-H_0\sin\beta - D_{out,1}E_{out,1}\frac{1}{a^2}\right),\\
C_{in,n\geq 2}E_{in,n\geq 2} &= \frac{\mu_{out}}{\mu_{in}}\left(-D_{out,n\geq 2}E_{out,n\geq 2}\frac{1}{a^{2n}}\right),\\
C_{in,n\geq 1}F_{in,n\geq 1} &= \frac{\mu_{out}}{\mu_{in}}\left(-D_{out,n\geq 1}F_{out,n\geq 1}\frac{1}{a^{2n}}\right),\\
C_{in,n\geq 1}G_{in,n\geq 1} &= \frac{\mu_{out}}{\mu_{in}}\left(-D_{out,n\geq 1}G_{out,n\geq 1}\frac{1}{a^{2n}}\right),\\
C_{in,n\geq 1}H_{in,n\geq 1} &= \frac{\mu_{out}}{\mu_{in}}\left(-D_{out,n\geq 1}H_{out,n\geq 1}\frac{1}{a^{2n}}\right).
\end{aligned}$$

Combining these expressions,

$$\begin{aligned}
D_{out,1}E_{out,1} &= \frac{\mu_{in}-\mu_{out}}{\mu_{in}+\mu_{out}}H_0 a^2\sin\beta,\\
D_{out,n\geq 2}E_{out,n\geq 2} &= \frac{\mu_{out}}{\mu_{in}}\left(-D_{out,n\geq 2}E_{out,n\geq 2}\right),\\
D_{out,n\geq 1}F_{out,n\geq 1} &= \frac{\mu_{out}}{\mu_{in}}\left(-D_{out,n\geq 1}F_{out,n\geq 1}\right),\\
D_{out,n\geq 1}G_{out,n\geq 1} &= \frac{\mu_{out}}{\mu_{in}}\left(-D_{out,n\geq 1}G_{out,n\geq 1}\right),\\
D_{out,n\geq 1}H_{out,n\geq 1} &= \frac{\mu_{out}}{\mu_{in}}\left(-D_{out,n\geq 1}H_{out,n\geq 1}\right).
\end{aligned}$$

Thus,

$$D_{out,n\geq 2}E_{out,n\geq 2}\left(1+\frac{\mu_{out}}{\mu_{in}}\right) = 0,$$

giving

$$D_{out,n\geq 2}E_{out,n\geq 2} = 0.$$

Similarly,

$$D_{out,n\geq 1}F_{out,n\geq 1} = D_{out,n\geq 1}G_{out,n\geq 1} = D_{out,n\geq 1}H_{out,n\geq 1} = 0,$$

and therefore

$$C_{in,1}E_{in,1} = -\frac{2\mu_{out}}{\mu_{in}+\mu_{out}}H_0\sin\beta,$$

and

$$\begin{aligned}
C_{in,n\geq 2}E_{in,n\geq 2} = C_{in,n\geq 1}F_{in,n\geq 1} = 0,\\
C_{in,n\geq 1}G_{in,n\geq 1} = C_{in,n\geq 1}H_{in,n\geq 1} = 0.
\end{aligned}$$

Substituting these coefficients into (7.64) and (7.65), we have

$$\Omega_{out} = -H_0 z\cos\beta - H_0 r\cos\varphi\sin\beta + \frac{\mu_{in}-\mu_{out}}{\mu_{in}+\mu_{out}}H_0 a^2\sin\beta\frac{1}{r}\cos\varphi, \quad (7.67)$$

and

$$\Omega_{in} = D_{in,0}z - \frac{2\mu_{out}}{\mu_{in}+\mu_{out}}H_0\sin\beta\left(r\cos\varphi\right). \quad (7.68)$$

Applying condition 6: for $r = a$, $\frac{\partial\Omega_{in}}{\partial z} = \frac{\partial\Omega_{out}}{\partial z}$

Differentiating (7.67) and (7.68) with respects to z and substituting $r = a$,

$$\begin{aligned}\frac{\partial\Omega_{out}}{\partial z} &= -H_0\cos\beta,\\ \frac{\partial\Omega_{in}}{\partial z} &= D_{in,0},\end{aligned}$$

we have

$$D_{in,0} = -H_0\cos\beta.$$

Substituting $\mu_{in} = \mu_0\left(1+\chi_{in}\right)$, $\mu_{out} = \mu_0\left(1+\chi_{out}\right)$ and $x = r\cos\varphi$, our scalar fields are

$$\begin{aligned}\Omega_{in} &= -H_0 z\cos\beta - \frac{2\left(1+\chi_{out}\right)}{2+\chi_{in}+\chi_{out}}H_0 x\sin\beta,\\ \Omega_{out} &= -H_0 z\cos\beta - H_0 x\sin\beta + \frac{\chi_{in}-\chi_{out}}{2+\chi_{in}+\chi_{out}}H_0 a^2\sin\beta\frac{1}{r^2}r\cos\varphi.\end{aligned}$$

Expressions for the field induced inside the cylinder

The magnetic field intensity inside the cylinder is

$$\begin{aligned}\boldsymbol{H}_{in} &= -\nabla\Omega_{in}\\ &= H_0\cos\beta\hat{\boldsymbol{z}} + \frac{2\left(1+\chi_{out}\right)}{2+\chi_{in}+\chi_{out}}H_0\sin\beta\hat{\boldsymbol{x}}.\end{aligned}$$

The magnetisation inside the cylinder is

$$\begin{aligned}\boldsymbol{M}_{in} &= \chi_{in}\boldsymbol{H}_{in}\\ &= \chi_{in}H_0\cos\beta\hat{\boldsymbol{z}} + \frac{2\chi_{in}\left(1+\chi_{out}\right)}{2+\chi_{in}+\chi_{out}}H_0\sin\beta\hat{\boldsymbol{x}}.\end{aligned}$$

The magnetic flux density inside the cylinder is

$$\begin{aligned}\boldsymbol{B}_{in} &= \mu_{in}\boldsymbol{H}_{in}\\ &= \left(1+\chi_{in}\right)B_0\cos\beta\hat{\boldsymbol{z}} + \frac{2\left(1+\chi_{in}\right)\left(1+\chi_{out}\right)}{2+\chi_{in}+\chi_{out}}B_0\sin\beta\hat{\boldsymbol{x}}.\end{aligned}$$

Expressions for the field induced outside the cylinder

The magnetic field intensity outside the cylinder is

$$\begin{aligned}\boldsymbol{H}_{out} &= -\nabla\Omega_{out}\\ &= H_0\cos\beta\hat{\boldsymbol{z}} + H_0\sin\beta\hat{\boldsymbol{x}} + \frac{\chi_{in}-\chi_{out}}{2+\chi_{in}+\chi_{out}}H_0a^2\sin\beta\left(-\nabla\frac{1}{r}\cos\varphi\right)\\ &= \boldsymbol{H}_0 + \frac{\chi_{in}-\chi_{out}}{2+\chi_{in}+\chi_{out}}H_0\frac{a^2}{r^2}\sin\beta\left(\cos\varphi\hat{\boldsymbol{r}}+\sin\varphi\hat{\boldsymbol{\varphi}}\right)\\ &= \boldsymbol{H}_0 + \frac{\chi_{in}-\chi_{out}}{2+\chi_{in}+\chi_{out}}H_0\frac{a^2}{r^2}\sin\beta\left(\cos\varphi\left(\cos\varphi\hat{\boldsymbol{x}}+\sin\varphi\hat{\boldsymbol{y}}\right)\right.\\ &\qquad\left.+\sin\varphi\left(-\sin\varphi\hat{\boldsymbol{x}}+\cos\varphi\hat{\boldsymbol{y}}\right)\right)\\ &= \boldsymbol{H}_0 + \frac{\chi_{in}-\chi_{out}}{2+\chi_{in}+\chi_{out}}H_0\frac{a^2}{r^2}\sin\beta\left(\cos2\varphi\hat{\boldsymbol{x}}+\sin2\varphi\hat{\boldsymbol{y}}\right).\end{aligned}$$

The magnetisation outside the cylinder is

$$\begin{aligned}\boldsymbol{M}_{out} &= \chi_{out}\boldsymbol{H}_{out}\\ &= \chi_{out}\boldsymbol{H}_0 + \frac{\chi_{out}\left(\chi_{in}-\chi_{out}\right)}{2+\chi_{in}+\chi_{out}}H_0\frac{a^2}{r^2}\sin\beta\left(\cos2\varphi\hat{\boldsymbol{x}}+\sin2\varphi\hat{\boldsymbol{y}}\right).\end{aligned}$$

The magnetic flux density outside the cylinder is

$$\begin{aligned}\boldsymbol{B}_{out} &= \mu_0\left(1+\chi_{out}\right)\boldsymbol{H}_{out}\\ &= \left(1+\chi_{out}\right)\boldsymbol{B}_0 + \frac{\left(1+\chi_{out}\right)\left(\chi_{in}-\chi_{out}\right)}{2+\chi_{in}+\chi_{out}}B_0\frac{a^2}{r^2}\sin\beta\left(\cos2\varphi\hat{\boldsymbol{x}}+\sin2\varphi\hat{\boldsymbol{y}}\right).\end{aligned}$$

A3 Lorentz sphere correction

The Lorentz sphere correction accounts for the difference between the macroscopic magnetic flux density and the flux density experienced by the nucleus, which is indirectly measured in MRI. The correction requires $\Delta B_{Lorentz} = -\frac{2}{3}\mu_0\boldsymbol{M}$ to be added to the macroscopic magnetic flux density, $\boldsymbol{B}$.

The magnetic flux density experienced by a nucleus inside a sphere is

$$\begin{aligned}\boldsymbol{B}_{S,in} &= \frac{3\left(1+\chi_{out}\right)\left(1+\chi_{in}\right)}{3+2\chi_{out}+\chi_{in}}\boldsymbol{B}_0 - \frac{2}{3}\mu_0\left[\frac{3\chi_{in}\left(1+\chi_{out}\right)}{3+2\chi_{out}+\chi_{in}}\boldsymbol{H}_0\right]\\ &= \left(1+\frac{\chi_{out}\left(1+\chi_{in}\right)}{3+2\chi_{out}+\chi_{in}}\right)\boldsymbol{B}_0,\end{aligned}$$

and outside a sphere is

$$\begin{aligned}
\boldsymbol{B}_{S,out} &= (1+\chi_{out})\,\boldsymbol{B}_0 + \frac{(1+\chi_{out})\,(\chi_{in}-\chi_{out})}{3+2\chi_{out}+\chi_{in}} a^3 B_0 \left(\frac{3\,(\hat{\boldsymbol{z}}\cdot\hat{\boldsymbol{r}})\,\hat{\boldsymbol{r}}-\hat{\boldsymbol{z}}}{r^3}\right) \\
&\quad -\frac{2}{3}\mu_0 \left[\chi_{out}\boldsymbol{H}_0 + \frac{\chi_{out}\,(\chi_{in}-\chi_{out})}{3+2\chi_{out}+\chi_{in}} a^3 H_0 \left(\frac{3\,(\hat{\boldsymbol{z}}\cdot\hat{\boldsymbol{r}})\,\hat{\boldsymbol{r}}-\hat{\boldsymbol{z}}}{r^3}\right)\right] \\
&= \left(1+\frac{\chi_{out}}{3}\right)\boldsymbol{B}_0 + \left[\frac{(\chi_{in}-\chi_{out})\,(3-\chi_{out})}{3\,(3+2\chi_{out}+\chi_{in})}\right] a^3 B_0 \left(\frac{3\,(\hat{\boldsymbol{z}}\cdot\hat{\boldsymbol{r}})\,\hat{\boldsymbol{r}}-\hat{\boldsymbol{z}}}{r^3}\right).
\end{aligned}$$

The corresponding equations for a cylinder are

$$\begin{aligned}
\boldsymbol{B}_{C,in} &= (1+\chi_{in})\,B_0\cos\beta\hat{\boldsymbol{z}} + \frac{2\,(1+\chi_{in})\,(1+\chi_{out})}{2+\chi_{in}+\chi_{out}} B_0 \sin\beta\hat{\boldsymbol{x}} \\
&\quad -\frac{2}{3}\mu_0\left[\chi_{in}H_0\cos\beta\hat{\boldsymbol{z}} + \frac{2\chi_{in}\,(1+\chi_{out})}{2+\chi_{in}+\chi_{out}} H_0\sin\beta\hat{\boldsymbol{x}}\right] \\
&= \left(1+\frac{\chi_{in}}{3}\right) B_0\cos\beta\hat{\boldsymbol{z}} \\
&\quad + \left[\left(1+\frac{\chi_{in}}{3}\right)\frac{2\,(1+\chi_{out})}{2+\chi_{in}+\chi_{out}}\right] B_0\sin\beta\hat{\boldsymbol{x}},
\end{aligned} \tag{7.69}$$

and

$$\begin{aligned}
\boldsymbol{B}_{C,out} &= (1+\chi_{out})\,\boldsymbol{B}_0 + \frac{(1+\chi_{out})\,(\chi_{in}-\chi_{out})}{2+\chi_{in}+\chi_{out}} B_0 \frac{a^2}{r^2}\sin\beta\,\times \\
&\quad (\cos 2\varphi\hat{\boldsymbol{x}} + \sin 2\varphi\hat{\boldsymbol{y}}) - \frac{2}{3}\mu_0\,[\chi_{out}\boldsymbol{H}_0 \\
&\quad + \frac{\chi_{out}\,(\chi_{in}-\chi_{out})}{2+\chi_{in}+\chi_{out}} H_0 \frac{a^2}{r^2}\sin\beta\,(\cos 2\varphi\hat{\boldsymbol{x}}+\sin 2\varphi\hat{\boldsymbol{y}})\Big] \\
&= \left(1+\frac{\chi_{out}}{3}\right)\boldsymbol{B}_0 + \left(1+\frac{\chi_{out}}{3}\right)\frac{\chi_{in}-\chi_{out}}{2+\chi_{in}+\chi_{out}}\times \\
&\quad B_0\frac{a^2}{r^2}\sin\beta\,(\cos 2\varphi\hat{\boldsymbol{x}}+\sin 2\varphi\hat{\boldsymbol{y}}).
\end{aligned} \tag{7.70}$$

A4 Superposition theory and the convolution kernels

Magnetic flux density due to magnetic susceptibility distribution behaves according to the superposition principle when considered on a macroscopic scale [38]. At position **r**, the total change in B field is equal to the sum of the changes at that point induced by the susceptibility of structures at all points in space,

$$\Delta\boldsymbol{B}\,(\boldsymbol{r}) = \sum_{\boldsymbol{r}'}\Delta\chi\,(\boldsymbol{r}')\,\boldsymbol{F}\,(\boldsymbol{r}-\boldsymbol{r}') \tag{7.71}$$

where $\boldsymbol{F}\,(\mathbf{r}-\mathbf{r}')$ is a three dimensional kernel function describing $\Delta\boldsymbol{B}$ induced by the structure at $\boldsymbol{r}'$ and $\Delta\chi$ is the susceptibility of that structure.

In MRI, only the changes in the direction of the applied B field are reflected in the phase data, from which ΔB is calculated. During the processing of the phase data, slow varying fluctuations are removed. This effectively removes the constant terms from the $\boldsymbol{B}$ equations.

The spherical model convolution kernel

The first order approximation of ΔB induced by a sphere is

$$\begin{aligned} \Delta B_{S,out}\left(\boldsymbol{r}\right) &\approx \frac{\Delta\chi}{3}a^3 B_0\left(\frac{3\cos\theta-1}{r^3}\right), \\ \Delta B_{S,in}\left(\boldsymbol{r}\right) &\approx 0, \end{aligned}$$

where $\Delta\chi = \chi_{in} - \chi_{out}$, $\chi \ll 1$, only the component of $\boldsymbol{B}$ in the direction of the applied B field is retained and the constant $\left(1+\frac{\chi_{out}}{3}\right)B_0$ term is subtracted.

In the context of susceptibility mapping, we can ensure that image data is acquired with isotropic voxel size and with the z or 3rd image dimension aligned to the main B field. We apply the spherical model convolution kernel to cubic voxels by equating the volume of the sphere with the volume of a voxel,

$$\begin{aligned} \frac{4\pi a^3}{3} &= d^3 \\ \frac{a^3}{3} &= \frac{d^3}{4\pi} \end{aligned}$$

where d is the side length of a voxel. We redefine the units of r as voxel side lengths, that is $r \Rightarrow rd$,

$$\Delta B_{S,out}\left(\boldsymbol{r}\right) = \Delta\chi\frac{B_0}{4\pi}\left(\frac{3\cos^2\theta-1}{r^3}\right).$$

Applying the superposition principle, we obtain

$$\Delta B_{S,out}\left(\boldsymbol{r}\right) = \sum_{\boldsymbol{r}'}\Delta\chi\left(\boldsymbol{r}'\right)F_S\left(\boldsymbol{r}-\boldsymbol{r}'\right)$$

where

$$F_s\left(\mathbf{r}\right) = \begin{cases} \frac{B_0}{4\pi}\left(\frac{3\cos^2\theta-1}{r^3}\right), & r>0 \\ 0, & r=0 \end{cases}$$

is the spherical model convolution kernel.

Cylindrical model convolution kernel

The component of $\boldsymbol{B}_{C,in}$ in the direction of the B_0 field is the dot product of (7.69) and the unit vector of (7.60):

$$\begin{aligned}
B_{C,in} &= \left(1+\frac{\chi_{in}}{3}\right) B_0 \cos^2\beta + \left[\left(1+\frac{\chi_{in}}{3}\right)\frac{2\left(1+\chi_{out}\right)}{2+\chi_{in}+\chi_{out}}\right] B_0 \sin^2\beta \\
&= B_0 + \frac{\chi_{in}}{3} B_0 \cos^2\beta + \left[\left(1+\frac{\chi_{in}}{3}\right)\frac{2\left(1+\chi_{out}\right)}{2+\chi_{in}+\chi_{out}} - 1\right] B_0 \sin^2\beta \\
&= B_0 + \frac{\chi_{in}}{3} B_0 \cos^2\beta + \left[\frac{\chi_{out}-\chi_{in}}{2+\chi_{in}+\chi_{out}} + \frac{2\chi_{in}\left(1+\chi_{out}\right)}{3\left(2+\chi_{in}+\chi_{out}\right)}\right] B_0 \sin^2\beta \\
&\approx B_0 + \frac{\chi_{in}}{3} B_0 \cos^2\beta + \left[\frac{\chi_{out}-\chi_{in}}{2} + \frac{\chi_{in}}{3}\right] B_0 \sin^2\beta \\
&= \left(1+\frac{\chi_{out}}{3} - \frac{\chi_{in}-\chi_{out}}{6}\right) B_0 + \frac{\chi_{in}-\chi_{out}}{2} B_0 \cos^2\beta \\
&= \left(1+\frac{\chi_{out}}{3}\right) B_0 + \frac{\chi_{in}-\chi_{out}}{6} B_0 \left(3\cos^2\beta - 1\right). \qquad (7.72)
\end{aligned}$$

The component of $\boldsymbol{B}_{C,out}$ in the direction of the B_0 field is given by

$$\begin{aligned}
B_{C,out} &= \left(1+\frac{\chi_{out}}{3}\right) B_0 + \left(1+\frac{\chi_{out}}{3}\right)\frac{\chi_{in}-\chi_{out}}{2+\chi_{in}+\chi_{out}} B_0 \frac{a^2}{r^2} \sin^2\beta \cos 2\varphi \\
&\approx \left(1+\frac{\chi_{out}}{3}\right) B_0 + \frac{\chi_{in}-\chi_{out}}{2} B_0 \frac{a^2}{r^2} \sin^2\beta \cos 2\varphi. \qquad (7.73)
\end{aligned}$$

We arrive at the first order approximation of $\Delta\boldsymbol{B}$ induced by a cylinder by considering the elimination of the first term in (7.72) and (7.73) as a result of the bias field removal during phase processing:

$$\begin{aligned}
\Delta B_{C,in}\left(\boldsymbol{r}\right) &\approx \frac{\Delta\chi}{6} B_0 \left(3\cos^2\beta - 1\right), \\
\Delta B_{C,out}\left(\boldsymbol{r}\right) &\approx \frac{\Delta\chi}{2} B_0 \frac{a^2}{r^2} \sin^2\beta \cos 2\varphi.
\end{aligned}$$

The convolution kernel is a 3D cubic array centred on a cylinder at angle β to the main field. The cylinder has a cross-sectional area equal to the cross sectional area of one voxel, that is

$$\begin{aligned}
\pi a^2 &= d^2, \\
a^2 &= \frac{d^2}{\pi}.
\end{aligned}$$

where a is the radius of the cylinder and d is the side length of an isotropic voxel. Again, we redefine the units of r as voxel side lengths, that is $r \Rightarrow rd$. Only kernel elements located within the plane normal to the cylinder and intersecting the central element are non-zero. For ease of reading, we shall call this the cross-sectional plane. The contributions of these voxels to ΔB are given by

$$\begin{aligned}\Delta B_{C,in}\left(\boldsymbol{r}\right) &= \frac{\Delta\chi}{6}B_0\left(3\cos^2\beta-1\right),\\ \Delta B_{C,out}\left(\boldsymbol{r}\right) &= \frac{\Delta\chi}{2\pi}B_0\frac{1}{r^2}\sin^2\beta\cos 2\varphi.\end{aligned}$$

Applying the superposition principle, we have

$$\Delta B_{S,out}\left(\boldsymbol{r}\right)=\sum_{\boldsymbol{r}'}\Delta\chi\left(\boldsymbol{r}'\right)F_C\left(\boldsymbol{r}-\boldsymbol{r}'\right)$$

where

$$F_C\left(\boldsymbol{r}\right) = \begin{cases}\frac{B_0}{6}\left(3\cos^2\beta-1\right), & r=0\\ \frac{1}{2\pi}B_0\frac{1}{r^2}\sin^2\beta\cos 2\varphi, & \text{otherwise.}\end{cases} \tag{7.74}$$

For an arbitrary cylinder axis, $\hat{\boldsymbol{c}}$, redefinitions of the variables r and φ need to be considered. r was defined in cylindrical coordinates as the distance between $\boldsymbol{r}$ and $\hat{\boldsymbol{z}}$. However, with an arbitrary cylinder axis, r is redefined as the distance from $\boldsymbol{r}$ to $\hat{\boldsymbol{c}}$:

$$r=\left|\boldsymbol{r}-\left(\boldsymbol{r}\cdot\hat{\boldsymbol{c}}\right)\hat{\boldsymbol{c}}\right|. \tag{7.75}$$

φ is redefined as the angle between the projections of $\boldsymbol{r}$ and the direction of the B_0 field, $\hat{\boldsymbol{b}}$, onto the plane normal to $\hat{\boldsymbol{c}}$:

$$\begin{aligned}\cos\varphi &= \frac{\left(\boldsymbol{r}-\left(\boldsymbol{r}\cdot\hat{\boldsymbol{c}}\right)\hat{\boldsymbol{c}}\right)\cdot\left(\hat{\boldsymbol{b}}-\left(\hat{\boldsymbol{b}}\cdot\hat{\boldsymbol{c}}\right)\hat{\boldsymbol{c}}\right)}{\left|\boldsymbol{r}-\left(\boldsymbol{r}\cdot\hat{\boldsymbol{c}}\right)\hat{\boldsymbol{c}}\right|\left|\hat{\boldsymbol{b}}-\left(\hat{\boldsymbol{b}}\cdot\hat{\boldsymbol{c}}\right)\hat{\boldsymbol{c}}\right|}\\ &= \frac{\boldsymbol{r}\cdot\hat{\boldsymbol{b}}-\left(\boldsymbol{r}\cdot\hat{\boldsymbol{c}}\right)\left(\hat{\boldsymbol{b}}\cdot\hat{\boldsymbol{c}}\right)-\left(\boldsymbol{r}\cdot\hat{\boldsymbol{c}}\right)\left(\hat{\boldsymbol{b}}\cdot\hat{\boldsymbol{c}}\right)+\left(\boldsymbol{r}\cdot\hat{\boldsymbol{c}}\right)\left(\hat{\boldsymbol{b}}\cdot\hat{\boldsymbol{c}}\right)}{\left|\boldsymbol{r}-\left(\boldsymbol{r}\cdot\hat{\boldsymbol{c}}\right)\hat{\boldsymbol{c}}\right|\left|\hat{\boldsymbol{b}}-\left(\hat{\boldsymbol{b}}\cdot\hat{\boldsymbol{c}}\right)\hat{\boldsymbol{c}}\right|}\\ &= \frac{\boldsymbol{r}\cdot\hat{\boldsymbol{b}}-\left(\boldsymbol{r}\cdot\hat{\boldsymbol{c}}\right)\left(\hat{\boldsymbol{b}}\cdot\hat{\boldsymbol{c}}\right)}{\left|\boldsymbol{r}-\left(\boldsymbol{r}\cdot\hat{\boldsymbol{c}}\right)\hat{\boldsymbol{c}}\right|\left|\hat{\boldsymbol{b}}-\left(\hat{\boldsymbol{b}}\cdot\hat{\boldsymbol{c}}\right)\hat{\boldsymbol{c}}\right|}.\end{aligned}$$

Applying the trigonometric identity $\cos 2\varphi = 2\cos^2\varphi-1$, we have

$$\cos 2\varphi = 2\left(\frac{\boldsymbol{r}\cdot\hat{\boldsymbol{b}}-\left(\boldsymbol{r}\cdot\hat{\boldsymbol{c}}\right)\left(\hat{\boldsymbol{b}}\cdot\hat{\boldsymbol{c}}\right)}{\left|\boldsymbol{r}-\left(\boldsymbol{r}\cdot\hat{\boldsymbol{c}}\right)\hat{\boldsymbol{c}}\right|\left|\hat{\boldsymbol{b}}-\left(\hat{\boldsymbol{b}}\cdot\hat{\boldsymbol{c}}\right)\hat{\boldsymbol{c}}\right|}\right)^2-1. \tag{7.76}$$

Combining (7.74) with (7.75) and (7.76), the cylindrical model convolution kernel for an arbitrary cylinder axis is

$$F_C\left(\boldsymbol{r}\right) = \begin{cases} \frac{B_0}{6}\left(3\cos^2\beta - 1\right), & r = 0 \\ \frac{1}{2\pi}B_0\frac{1}{\left|\boldsymbol{r}-\left(\boldsymbol{r}\cdot\hat{\boldsymbol{c}}\right)\hat{\boldsymbol{c}}\right|^2}\sin^2\beta\left(2\left(\frac{\boldsymbol{r}\cdot\hat{\boldsymbol{b}}-\left(\boldsymbol{r}\cdot\hat{\boldsymbol{c}}\right)\left(\hat{\boldsymbol{b}}\cdot\hat{\boldsymbol{c}}\right)}{\left|\boldsymbol{r}-\left(\boldsymbol{r}\cdot\hat{\boldsymbol{c}}\right)\hat{\boldsymbol{c}}\right|\left|\hat{\boldsymbol{b}}-\left(\hat{\boldsymbol{b}}\cdot\hat{\boldsymbol{c}}\right)\hat{\boldsymbol{c}}\right|}\right)^2 - 1\right), & \text{otherwise,} \end{cases} \tag{7.77}$$

for analytical convolutions where only points within the cross-sectional plane are non-zero.

For numerical computations discretisation of points in the 3D kernel occurs. When the cylinder axis is not parallel to either the x, y or z axes, the discrete points of the kernel will rarely coincide with the cross-sectional plane. In order to calculate a numerical kernel that approximates the analytical kernel, we consider each voxel in the kernel as a sphere of radius α and define a slab that is 2α wide and parallel to and centred on the cross-sectional plane. The volume of the sphere that intersects with the slab (Figure 44) is given by

$$V_{SC}\left(\boldsymbol{r}\right) = \frac{\pi h\left(\mathbf{r}\right)^2\left(3\alpha - h\left(\mathbf{r}\right)\right)}{3}.$$

h is the height of the intersecting region and is determined by the position vector $\mathbf{r}$ and the cylinder axis

$$h\left(\mathbf{r}\right) = 2\alpha - \mathbf{r}\cdot\hat{\mathbf{c}}$$

where $\hat{\mathbf{c}}$ is a unit vector representing the cylinder axis. The proportion of V_{SC} to the total volume of the sphere, $V_S = \frac{4\pi\alpha^3}{3}$, is

$$\begin{aligned} P\left(\mathbf{r}\right) &= \frac{V_{SC}\left(\mathbf{r}\right)}{V_S} \\ &= \frac{\pi h\left(\mathbf{r}\right)^2}{3}\left(3\alpha - h\left(\mathbf{r}\right)\right)\frac{3}{4\pi\alpha^3} \\ &= \frac{\left(2\alpha - \mathbf{r}\cdot\hat{\mathbf{c}}\right)^2\left(\alpha + \mathbf{r}\cdot\hat{\mathbf{c}}\right)}{4\alpha^3}. \end{aligned} \tag{7.78}$$

The cylinder model kernel is numerically defined as:

$$F\left(\mathbf{r}\right) = \begin{cases} \frac{B_0}{6}\left(3\cos^2\beta - 1\right), & r = 0 \\ P\left(\mathbf{r}\right)\frac{1}{2\pi}B_0\frac{1}{\left|\boldsymbol{r}-\left(\boldsymbol{r}\cdot\hat{\boldsymbol{c}}\right)\hat{\boldsymbol{c}}\right|^2}\sin^2\beta\left(2\left(\frac{\boldsymbol{r}\cdot\hat{\boldsymbol{b}}-\left(\boldsymbol{r}\cdot\hat{\boldsymbol{c}}\right)\left(\hat{\boldsymbol{b}}\cdot\hat{\boldsymbol{c}}\right)}{\left|\boldsymbol{r}-\left(\boldsymbol{r}\cdot\hat{\boldsymbol{c}}\right)\hat{\boldsymbol{c}}\right|\left|\hat{\boldsymbol{b}}-\left(\hat{\boldsymbol{b}}\cdot\hat{\boldsymbol{c}}\right)\hat{\boldsymbol{c}}\right|}\right)^2 - 1\right), & \text{otherwise} \end{cases}$$

The parameter α was optimised by convolving the numerical kernel with a known susceptibility map and comparing the resulting ΔB map with the theoretical ΔB map. Seventeen cylinder axes were distributed over an area of the unit sphere representing a range of angles that would result in different discretisation

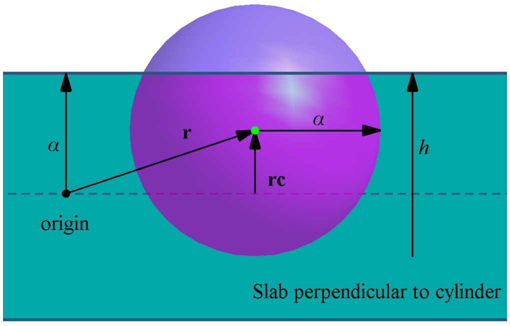

Figure 44: Intersection of sphere with slab

profiles (Fig. 45a). For each cylinder axis, a numerical phantom consisting of a single cylinder of susceptibility 4×10^{-7} was created. The theoretical ΔB map was calculated using (7.77). Numerical kernels were created for a range of α values. Each kernel was convolved with the numerical susceptibility map and the standard deviation of the difference between the result and the theoretical ΔB map was calculated. The optimum α value is that with the lowest mean standard deviation across the seventeen cylinder axes, determined to be $\alpha = 0.47$ (Fig. 45b).

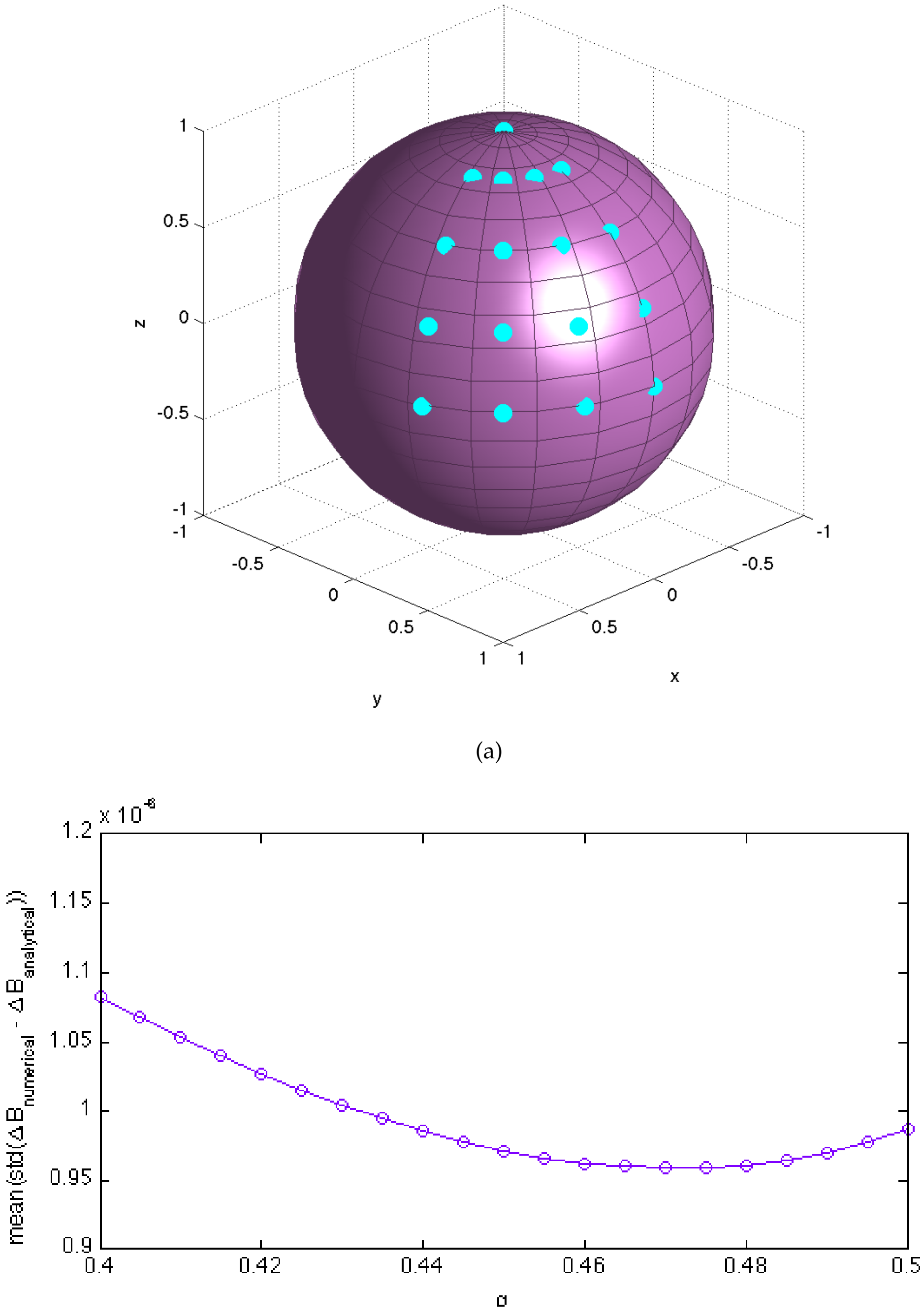

(a)

(b)

Figure 45: Optimising parameter α. (a) Positioning of the seventeen cylinder axes (denoted by blue dots) on the unit sphere for optimising parameter α in (7.78). (b) Mean of the standard deviation of the difference between derived and theoretical ΔB maps for varying α.

BIBLIOGRAPHY

[1] Madhavi Thomas and Joseph Jankovic. Neurodegenerative disease and iron storage in the brain. *Current Opinion in Neurology*, 17(4):437–442, August 2004.

[2] Luigi Zecca, Moussa B. H. Youdim, Peter Riederer, James R. Connor, and Robert R. Crichton. Iron, brain ageing and neurodegenerative disorders. *Nature Reviews Neuroscience*, 5(11):863–873, November 2004.

[3] D Faul, J Arbart, and P Margosian. Quick measurement of magnetic field variations within the body. *Radiology*, 153:303–4, 1984.

[4] I. Jane Cox, Graeme M. Bydder, David G. Gadian, Ian R. Young, Edward Proctor, Stephen R. Williams, and Ian Hart. The effect of magnetic susceptibility variations in NMR imaging and nmr spectroscopy in vivo. *Journal of Magnetic Resonance (1969)*, 70(1):163–168, October 1986.

[5] I. R Young, S. Khenia, D. G. T Thomas, C. H Davis, D. G Gadian, I. J Cox, B. D Ross, and G. M Bydder. Clinical magnetic susceptibility mapping of the brain. *Journal of Computer Assisted Tomography*, 11(1):2–6, January 1987.

[6] Robert M. Weisskoff and Suzanne Kiihne. MRI susceptometry: Image-based measurement of absolute susceptibility of MR contrast agents and human blood. *Magnetic Resonance in Medicine*, 24(2):375–383, April 1992.

[7] R. Bhagwandien, M.A. Moerland, C.J.G. Bakker, R. Beersma, and J.J.W. Lagendijk. Numerical analysis of the magnetic field for arbitrary magnetic susceptibility distributions in 3D. *Magnetic Resonance Imaging*, 12(1):101–107, 1994.

[8] Randall W. Holt, Pedro J. Diaz, Jeffrey L. Duerk, and Errol M. Bellon. MR susceptometry: an external-phantom method for measuring bulk susceptibility from field-echo phase reconstruction maps. *Journal of Magnetic Resonance Imaging*, 4(6):809–818, November 1994.

[9] O. Beuf, A. Briguet, M. Lissac, and R. Davis. Magnetic resonance imaging for the determination of magnetic susceptibility of materials. *Journal of Magnetic Resonance, Series B*, 112(2):111–118, August 1996.

[10] Zhiyue J. Wang, Shuchun Li, and John C. Haselgrove. Magnetic resonance imaging measurement of volume magnetic susceptibility using a boundary condition. *Journal of Magnetic Resonance*, 140(2):477–481, October 1999.

[11] Christopher M. Collins, Bei Yang, Qing X. Yang, and Michael B. Smith. Numerical calculations of the static magnetic field in three-dimensional multi-tissue models of the human head. *Magnetic Resonance Imaging*, 20(5):413–424, June 2002.

[12] R. Salomir, B. D. de Senneville, and C. T. Moonen. A fast calculation method for magnetic field inhomogeneity due to an arbitrary distribution of bulk susceptibility. *Concepts in Magnetic Resonance Part B: Magnetic Resonance Engineering*, 19B(1):26–34, 2003.

[13] Mark Jenkinson, James L. Wilson, and Peter Jezzard. Perturbation method for magnetic field calculations of nonconductive objects. *Magnetic Resonance in Medicine*, 52(3):471–477, 2004.

[14] JP Marques and R Bowtell. Application of a fourier-based method for rapid calculation of field inhomogeneity due to spatial variation of magnetic susceptibility. *Concepts in Magnetic Resonance Part B: Magnetic Resonance Engineering*, 25B(1):78, 65, April 2005.

[15] Lin Li and John S. Leigh. Quantifying arbitrary magnetic susceptibility distributions with MR. *Magnetic Resonance in Medicine*, 51(5):1077–1082, May 2004.

[16] Jeff H. Duyn, Peter van Gelderen, Tie-Qiang Li, Jacco A. de Zwart, Alan P. Koretsky, and Masaki Fukunaga. High-field MRI of brain cortical substructure based on signal phase. *Proceedings of the National Academy of Sciences*, 104(28):11796–11801, July 2007.

[17] Karin Shmueli, Jacco A. de Zwart, Peter van Gelderen, Tie-Qiang Li, Stephen J. Dodd, and Jeff H. Duyn. Magnetic susceptibility mapping of brain tissue in vivo using MRI phase data. *Magnetic Resonance in Medicine*, 62(6):1510–1522, December 2009.

[18] Wei Li, Bing Wu, and Chunlei Liu. Quantitative susceptibility mapping of human brain reflects spatial variation in tissue composition. *NeuroImage*, 55(4):1645–1656, April 2011.

[19] Sam Wharton, Andreas Schäfer, and Richard Bowtell. Susceptibility mapping in the human brain using threshold-based k-space division. *Magnetic Resonance in Medicine*, 63(5):1292–1304, 2010.

[20] Tian Liu, Pascal Spincemaille, Ludovic de Rochefort, Bryan Kressler, and Yi Wang. Calculation of susceptibility through multiple orientation sampling (COSMOS): a method for conditioning the inverse problem from measured magnetic field map to susceptibility source image in MRI. *Magnetic Resonance in Medicine*, 61(1):196–204, January 2009.

[21] Bryan Kressler, Ludovic de Rochefort, Tian Liu, Pascal Spincemaille, Quan Jiang, and Yi Wang. Nonlinear regularization for per voxel estimation of magnetic susceptibility distributions from MRI field maps. *IEEE Transactions on Medical Imaging*, 29(2):273–81, 2009.

[22] Ludovic de de Rochefort, Tian Liu, Bryan Kressler, Jing Liu, Pascal Spincemaille, Vincent Lebon, Jianlin Wu, and Yi Wang. Quantitative susceptibility map reconstruction from MR phase data using bayesian regularization: Validation and application to brain imaging. *Magnetic Resonance in Medicine*, 63(1):194–206, 2010.

[23] Tian Liu, Jing Liu, Ludovic de Rochefort, Pascal Spincemaille, Ildar Khalidov, James Robert Ledoux, and Yi Wang. Morphology enabled dipole inversion (MEDI) from a single-angle acquisition: Comparison with COSMOS in human brain imaging. *Magnetic Resonance in Medicine*, 66(3):777–783, 2011.

[24] Ferdinand Schweser, Karsten Sommer, Andreas Deistung, and Jürgen Rainer Reichenbach. Quantitative susceptibility mapping for investigating subtle susceptibility variations in the human brain. *NeuroImage*, 62(3):2083–2100, September 2012.

[25] Xiang He and Dmitriy A. Yablonskiy. Biophysical mechanisms of phase contrast in gradient echo MRI. *Proceedings of the National Academy of Sciences*, 106(32):13558–13563, 2009.

[26] Jongho Lee, Karin Shmueli, Masaki Fukunaga, Peter van Gelderen, Hellmut Merkle, Afonso C. Silva, and Jeff H. Duyn. Sensitivity of MRI resonance frequency to the orientation of brain tissue microstructure. *Proceedings of the National Academy of Sciences*, 107(11):5130–5135, March 2010.

[27] Christian Denk, Enedino Hernandez Torres, Alex MacKay, and Alexander Rauscher. The influence of white matter fibre orientation on MR signal phase and decay. *NMR in Biomedicine*, 24(3):246–252, 2011.

[28] Pascal Sati, Afonso C. Silva, Peter van Gelderen, Maria I. Gaitan, Jillian E. Wohler, Steven Jacobson, Jeff H. Duyn, and Daniel S. Reich. In vivo quantification of T2* anisotropy in white matter fibers in marmoset monkeys. *NeuroImage*, 59(2):979–985, January 2012.

[29] Jongho Lee, Peter van Gelderen, Li-Wei Kuo, Hellmut Merkle, Afonso C. Silva, and Jeff H. Duyn. T2*-based fiber orientation mapping. *NeuroImage*, 57(1):225–234, July 2011.

[30] L. Landweber. An iteration formula for Fredholm integral equations of the first kind. *American Journal of Mathematics*, 73(3):615–624, July 1951.

[31] M. Bertero and P. Boccacci. *Introduction to Inverse Problems in Imaging*. CRC Press, December 2010.

[32] Zhaolin Chen, Leigh A. Johnston, Dae Hyuk Kwon, Se Hong Oh, Zang-Hee Cho, and Gary F. Egan. An optimised framework for reconstructing and processing MR phase images. *NeuroImage*, 49(2):1289–1300, January 2010.

[33] Amanda Ng, Leigh Johnston, Zhaolin Chen, Zang-Hee Cho, Jingxin Zhang, and Gary Egan. Spatially dependent filtering for removing phase distortions at the cortical surface. *Magnetic Resonance in Medicine*, 2011.

[34] T. E.J Behrens, M. W Woolrich, M. Jenkinson, H. Johansen-Berg, R. G Nunes, S. Clare, P. M Matthews, J. M Brady, and S. M Smith. Characterization and propagation of uncertainty in diffusion-weighted MR imaging. *Magnetic Resonance in Medicine*, 50(5):1077–1088, November 2003.

[35] Kaluza, Owen L., Ng, Amanda C. L., Wright, David K., Johnston, Leigh A., Grundy, John, and Barnes, David G. Fast diffusion-guided QSM using graphical processing units. In *International Society for Magnetic Resonance in Medicine 21st Scientific Meeting and Exhibition*, Salt Lake City, USA, 2013.

[36] E. M Pugh and E.W. Pugh. *Principles of Electricity and Magnetism*. Addison-Wesley Publishing Company, Inc, Reading, Massachusetts, USA, 1960.

[37] E. Mark Haacke, Robert W. Brown, Michael R. Thompson, and Ramesh Venkatesan. *Magnetic resonance imaging: physical principles and sequence design*. John Wiley & Sons, Inc, New York, 1999.

[38] John David Jackson. In *Classical Electrodynamics 3rd Ed*, pages 184–188. John Wiley & Sons, Inc, New York, 1998.

8

CONCLUSION

MR phase imaging provides novel contrast and information for better visualisation and quantification of tissue structures. Its contribution to the biomedical imaging field has moved from being a means to enhance and correct other MR imaging data, such as for bias field estimation, EPI field map correction, fMRI and in particular, susceptibility-weighted imaging, to being an imaging modality in its own right, as well as providing the basis of the important and promising field of quantitative susceptibility mapping. This change in emphasis is due to the increased resolution and contrast brought about by advances in high field MR technology. While these benefits present opportunities for further exploiting the information within phase, they are accompanied by artefacts and complications in phase images that were insignificant at lower fields. This thesis has presented four novel methods for processing and utilising phase data to improve estimation and interpretation of the information contained within.

Phase unwrapping and filtering play an integral part in eliciting important information from the phase of MRI data. These processing steps are non-trivial, where the operations are complicated by high gradients in the true phase. Gradients greater than 2π per voxel are especially difficult to resolve, since their position within the image become obscured by phase wrapping. Various unwrapping methods have been proposed that address high gradients to varying degrees of success. The most commonly used methods, such as homodyne filtering[1, 2], FSL PRELUDE [3] and ΦUN [4], assume some level of coherence in the phase of neighbouring voxels. This assumption is not always valid, particularly in regions of high gradients and noise. The recently proposed CAMPUS method [5] seeks to unwrap the phase through voxel-wise observation of the accumulation of phase at subsequent multiple echoes. It therefore does not rely on assumptions of spatial coherence and is a fast method compared to PRELUDE and ΦUN.

With the exclusion of homodyne filtering-based methods, these phase unwrapping methods do not remove the spatially slow varying bias fields. Current methods for bias field removal include high pass filtering [6], polynomial fitting [7], spherical mean estimation [8] and dipole fitting [9, 10]. These methods show varying degrees of success at removing high gradient fields, resulting in brain phase images with unreliable data near the cortical surface. In Chapter 4, the Spatially Dependent Filtering (SDF) method was proposed for correcting these surface artefacts. The method is computationally efficient and versatile in the choice of base filter kernel. It is not limited to correcting errors at the cortical surface; it can be applied to any arbitrary region where adjacent regions have different intensity characteristics that would otherwise introduce errors during the filtering process. Compared to traditional methods of removing bias fields from phase, SDF has been shown to produce more reliable phase information and reveal intricate details that remain obscured by other methods. For SWI and QSM applications, this improvement in surface information will provide for better visualisation of surface vessels, as well as more accurate estimation of magnetic susceptibility values, particularly at high field applications where surface artefacts are more pronounced.

Susceptibility weighted imaging is arguably the most common application for phase data in the clinical environment. High field technologies provide improved contrast in phase images, and in turn, improved visualisation of structures in SWI, such as venous vessels. However, susceptibility-induced artefacts are also amplified at high field and lead to blurring of vein boundaries in the image. In worst cases, the delineation of these vessels is affected to the extent that the width of the vessel is overestimated. In Chapter 5 we presented a modification to the traditional SWI method that corrects for these errors. The Sigmoid-SWI method was shown to successfully correct delineation of the venous vessels, while preserving SWI values within the vessel and the general appearance of the SWI image. The corrections associated with Sigmoid-SWI are not restricted to venous vessels, but theoretically correct for any structure where large magnetic susceptibility differences induce a change in field that is large enough to attenuate the magnitude of the MR signal. This advantage is particularly significant at higher fields, where the effects of susceptibility differences are enhanced.

While SWI is a popular method that combines magnitude and phase, the technique is heuristic, where the parameter n is adjusted according to the best achievable contrast in the image. While it was suggested that $n = 4$ is sufficient for venography at 1.5T, other values of n may be optimal at higher field strengths or for different applications. In Chapter 6, we presented the Optimised Contrast Imaging (OCI), for rigorous combination of magnitude and phase information. The method is a non-heuristic classification and optimisation-based method that has the ability to manipulate intra- and inter-class contrast, making it a valuable tool for visualising structural details in MRI data. Unlike SWI, it is not restricted to axial acquisitions of anisotropic voxel dimensions. The method demonstrates improved contrast and edge definition over three variants of the SWI method, and reveals structural detail not apparent in either the magnitude or phase. Although negative phase mask SWI is well-suited for venography studies, other applications, such as structural segmentation, would benefit from OCI's ability to delineate and discriminate structures. As well, its application to isotropic data allows for multiple viewing aspects. The method is not specific to magnitude and phase, and in fact can be applied to any two contrast images of the same structure, such as magnitude and susceptibility maps. The principles behind the method can also be extended to three or more contrast images. Thus OCI is a novel method for visualising multiple voxel-wise characteristics in a single two or three-dimensional image.

The recently emerged field of Quantitative Susceptibility Mapping (QSM) promises new ways to study the composition of tissues and track changes in the brain, particularly in relation to neurodegenerative disorders. There are several published methods that address the ill-posed mathematical nature of the QSM problem; however, the methods incorrectly assume a spherical model of susceptibility-induced field changes for all tissues and ignore the contribution of chemical exchange processes between water and macromolecules to the phase. The Diffusion-Guided Quantitative Susceptibility Mapping (dQSM) method presented in Chapter 7 addresses the inaccurate characterisation of white matter voxels with spherical models of magnetic field perturbations. The method demonstrates improved estimation of magnetic susceptibility values; however, it is disadvantaged by very long computation times. This makes the method, as implemented in this thesis, infeasible for normal research environments and clinical applications. It is, however, a successful proof-of-concept warranting investigations into algorithmic and computational optimisations. Recently, this algorithm has been implemented on GPUs, with a 16× speed up on 16 Kepler GPUs compared to 4096 CPU cores.

8.1 FUTURE WORK

It is arguable that the foreseeable future of MR phase imaging is QSM, where the dipolar nature of phase images has been eliminated and the intensity values have a specific physical meaning. QSM has specific problems that still require a reliable solution: the ill-posed nature of the system, the modelling of susceptibility-induced field changes and the phase contributions of chemical exchange processes. The ill-posed nature has been addressed by several methods; however, none presents a reliable solution for all situations. The multiple orientation acquisitions of COSMOS is infeasible in a clinical environment, while the assumptions of coherence between the gradients in the magnitude and the susceptibility map in the MEDI method may not always be valid. Due to the ill-posed nature of the system, the choice of regularisation and linear solving algorithm have a significant impact on the solution. While dQSM provides a means to more accurately model the susceptibility-induced field changes, the field lacks a reliable susceptibility and diffusion phantom model to verify dQSMs results. The computational demands of the method also make it infeasible in the clinical environment. Further algorithmic development of this method and the increased availability of GPU architecture will address this issue. The chemical exchange processes have been demonstrated to have a significant effect on phase; however, a method of eliminating these effects from the phase data has not been proposed. It is envisaged that the answer to this problem lies in specific MR acquisition sequences, rather than computational analysis. With solutions to these three problems, QSM promises to become a valuable and important tool in biomedical imaging, providing the means to study non-invasively the composition and compositional changes of both normal and diseased biological tissues.

BIBLIOGRAPHY

[1] Y. Wang, Y. Yu, D. Li, K.T. Bae, J.J. Brown, W. Lin, and E.M. Haacke. Artery and vein separation using susceptibility-dependent phase in contrast-enhanced MRA. *Journal of Magnetic Resonance Imaging*, 12(5):661–670, 2000.

[2] D.C. Noll, D.G. Nishimura, and A. Macovski. Homodyne detection in magnetic resonance imaging. *Medical Imaging, IEEE Transactions on*, 10(2):154–163, 1991.

[3] Mark Jenkinson, James L. Wilson, and Peter Jezzard. Perturbation method for magnetic field calculations of nonconductive objects. *Magnetic Resonance in Medicine*, 52(3):471–477, 2004.

[4] Stephan Witoszynskyj, Alexander Rauscher, Jürgen R. Reichenbach, and Markus Barth. Phase unwrapping of MR images using [Phi]UN - a fast and robust region growing algorithm. *Medical Image Analysis*, 13(2):257–268, April 2009.

[5] Wei Feng, Jaladhar Neelavalli, and E. Mark Haacke. Catalytic multiecho phase unwrapping scheme (CAMPUS) in multiecho gradient echo imaging: Removing phase wraps on a voxel-by-voxel basis. *Magnetic Resonance in Medicine*, (1):117–126, July 2012.

[6] Alexander Rauscher, Jan Sedlacik, Markus Barth, Hans-Joachim Mentzel, and Jurgen R. Reichenbach. Magnetic susceptibility-weighted MR phase imaging of the human brain. *AJNR Am J Neuroradiol*, 26(4):736–742, April 2005.

[7] Jeff H. Duyn, Peter van Gelderen, Tie-Qiang Li, Jacco A. de Zwart, Alan P. Koretsky, and Masaki Fukunaga. High-field MRI of brain cortical substructure based on signal phase. *Proceedings of the National Academy of Sciences*, 104(28):11796–11801, July 2007.

[8] F. Schweser, B.W. Lehr, Andreas Deistung, and Jürgen R. Reichenbach. A novel approach for separation of background phase in SWI phase data utilizing the harmonic function mean value property. In *Proceedings of the ISMRM/ESMRMB Joint Annual Meeting*, Stockholm, Sweden, January 2010.

[9] Tian Liu, Ildar Khalidov, Ludovic de Rochefort, Pascal Spincemaille, Jing Liu, and Yi Wang. Improved background field correction using effective dipole fitting. In *Proceedings of the ISMRM/ESMRMB Joint Annual Meeting*, Stockholm, Sweden, May 2010.

[10] Samuel James Wharton and Richard W. Bowtell. Dipole-based filtering for improved removal of background field effects from 3D phase data. In *Proceedings of the ISMRM/ESMRMB Joint Annual Meeting*, Stockholm, Sweden, May 2010.

Author/s:
Ng, Amanda Ching Lih

Title:
Techniques for the processing and analysis of magnetic resonance imaging phase data

Date:
2013

Citation:
Ng, A. C. L. (2013). Techniques for the processing and analysis of magnetic resonance imaging phase data. PhD thesis, Department of Electrical and Electronic Engineering, The University of Melbourne.

Persistent Link:
http://hdl.handle.net/11343/38674

File Description:
Techniques for the processing and analysis of magnetic resonance imaging phase data